Physically Based Real-Time Rendering of the Martian Atmosphere

Tim Meyran

Master Thesis

Hochschule Hannover
Faculty IV – Business and Computer Science
Course of Studies M. Sc. Applied Computer Sciences

November 7, 2022

Author

Tim Meyran
Matriculation Number: 1633612
E-Mail: tim.meyran@stud.hs-hannover.de

Examiner

Prof. Dr. Ingo Ginkel
Hochschule Hannover
Faculty IV, Computer Science
Ricklinger Stadtweg 120
30459 Hannover

Second Examiner

M. Sc. Simon Schneegans
German Aerospace Center (DLR)
Institute for Software Technology
Software for Space Systems and Interactive Visualization
Lilienthalplatz 7
38108 Braunschweig

Declaration of Authorship

I hereby declare that this thesis, and the work presented in it are my own and has been generated by me as the result of my own original research. I confirm that:

1. Where I have consulted the published work of others, this is always clearly attributed.

2. Where I have quoted from the work of others, the source is always given. Except for such quotations, this thesis is entirely my own work.

3. I have acknowledged all main sources of help.

4. Where the thesis is based on work done by myself jointly with others, I have made clear exactly what was done by others and what I have contributed myself.

Hannover, November 7, 2022
Location and Date   Signature

Contents

1 Introduction

Figure 1.1: NASA's Mars Exploration Rover Spirit captured this view as the Sun sank below the rim of Gusev crater on Mars [1]. Note that the color of the sunset is very different from the earths'. The sky itself has a reddish color, whereas the sunset show a blue glow around the sun.

1.1 Motivation

The physical equations that explain the color of the Earth's sky are well understood. On the other hand, simulating the radiometric energy transport through the atmosphere is very expensive to solve. Many interactive simulations and computer games would also benefit from an accurate representation of the atmosphere. This motivated the design of more efficient and accurate rendering algorithms [2].

For the Earth's atmosphere, many approximations have been developed over the years. Unfortunately, these approximations cannot be applied directly to other planets, like e.g., the martian atmosphere. For example, the blue sunsets on Mars, which can be seen in **Figure 1.1**, cannot be modelled with these commonly used approximations.

1.2 Goal

Over the years, many clear-sky models for the Earth's atmosphere have been developed, which vary largely in computational efficiency and visual accuracy. In order to achieve the goal of high interactive frame rates, these models have to be compared. The best performing model will be extended in order to support the rendering of the martian atmosphere. This will require a more fine-grained control over the phase function and extinction coefficients of the particles in the atmosphere.

The goal of this thesis is to improve an existing real-time rendering approach for planetary atmospheres. First, fundamental problems of the existing models have to be identified. Then, based on the many related studies which analyze and characterize the martian atmosphere, the improved model has to be designed. Just as all the previous models, the extended model will also be a clear sky models, which means that the model will not be able to render clouds or other similar local phenomenons like dust storm or dust devils.

Afterwards, the extended model should be compared to the previous models and if possible also to real world measurements. In order to perform this evaluation, a suitable solution has to be found or developed.

1.3 Outline

The **Background** chapter starts with an explanation of how light traverses through the atmosphere, which is then followed by a brief explanation of the physical effects. An explanation for the color palette of the Earth's sky is given and some key properties of particles, important to light scattering, are identified. Then some units related to light measurement are mentioned and explained. The scattering properties of particles can be calculated by a solution to *Maxwell's* equations called **Mie theory**. It describes a solution to absorption and scattering by small particles [3]. Unfortunately, due to the fact that light can take infinitely many paths and Mie's solution takes the form of an infinite series, the exact solution is hard to compute. In the context of computer graphics, this can be solved by some more or less accurate approximations.

The chapter **Related Work** starts with a detailed explanation of computer graphic models which are used to render the Earth's atmosphere. For the Earth, there are numerous models which are briefly mentioned by their key differences. Two important models are then described in more detail. The second part of the chapter deals with the martian atmosphere and its key differences to the Earth's. In order to simulate the martian's atmosphere as correctly as possible, its scattering properties have to be identified as accurately as possible. There has been done quite some research in this field and multiple results are going to be discussed.

The **Design and Implementation** chapter starts with a discussion of how already existing martian atmospheric models can be improved. A number of studies are mentioned, which compiled martian dust properties based on various measurements and also studied possible analogues that come closest to these observations. It's then the question of how these properties can be approximated to support the real-time aspect of the model. One approach would be to completely simulate the scattering behavior of the martian dust using Mie theory. In order to compare the different approaches, an already existing framework for the comparison of atmospheric models, developed by *Erik Bruneton* [2] is extended to also support the comparison of different atmospheric properties. The second part of the **Design and Implementation** chapter, discusses the implementation of the new approach in a real-time implementation.

The chapter **Results and Evaluation** starts with a quantitative comparison of all examined atmospheric martian models using the new extended framework of *Eric Bruneteon*. The evaluation compares radiance, chromaticity, and transmittance measurements against every examined model. These measurements have been accumulated by various martian orbiters, landers, and rovers and cover a variety of martian weather situations. Afterwards, various renderings are compared with real images taken on the Martian surface. These include sky dome images, ground perspectives and views from outer space. Finally, the advantages and disadvantages of all models are summarized.

2 Background

The appearance of the sky can be described by optical effects caused by various particles in the sky. The color of the Earth's sky results from the scattering and absorption of the sunlight by air molecules and aerosol particles [2]. It was already Isaac Newton who discovered that sunlight can be split into the colors of the rainbow when it is shone through a prism. He was also able to show that the colors are not *created* by the prism. Instead, he could show that sunlight is a mix of multiple spectral colors ranging from ultraviolet to infrared [4].

Light is electromagnetic radiation which is described by its wavelength λ. Sunlight for example contains a whole spectrum of different wavelengths. The visible part of the spectrum ranges from 380 to 780 nm [5]. How much each color contributes to the sunlight is shown in the spectral irradiance plot in **Figure 2.1**. Irradiance itself will be described in **Section 2.4**.
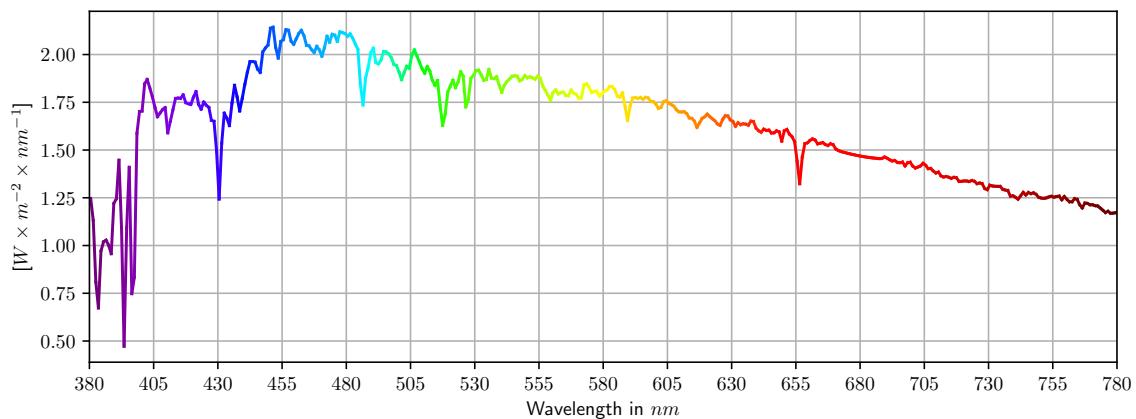
Figure 2.1: The radiance of the visible part of the solar spectrum from 380 to 780 nm [6]. The colors of the curve correspond to the wavelength.

Scattering and Absorption　There are two types of interaction between a photon and an atom: *scattering* and *absorption*. The type of interaction depends on the wavelength of the incident light, which is analogous to the energy of the photon. The energy of a photon is given by:

$$E = h \cdot f$$
$$f = c/\lambda$$

E : Photon energy
f : Wave frequency
λ : Wavelength
c : Speed of light
h : Planck's constant

(2.1)

5

If the energy of the photon is high enough to move an electron of the atom into a higher excited state, the photon will be absorbed. After this excitation, the atom may return to a lower excited state, by emitting a photon of a characteristic wavelength which is called **dissipative absorption** [8]. Otherwise, if the energy of the incoming photon is not large enough to excite an electron into a higher state, the electromagnetic field of the light can still drive the electron cloud into oscillation. The electron cloud starts to vibrate at the same frequency as the incident photon and may radiate a new photon in some new direction with that surplus energy, which consequently has the same frequency and wavelength as the incident photon. This process is called **elastic scattering** [8].

Figure 2.2: A ray of light being refracted in a plastic block [7].

Refraction   Refraction is the redirection of light passing from one medium to another, with a different local speed of light [8]. This effect can be seen in **Figure 2.2**. The plastic block has a different speed of light, which results in a refracted light path. This behavior is described by the complex refractive index $n = m + ki$, whereby the real part is the ratio of the speed of light of the two mediums and the imaginary part corresponds to the absorption of internally transmitted light [9].

2.1 Energy Transfer in the Atmosphere
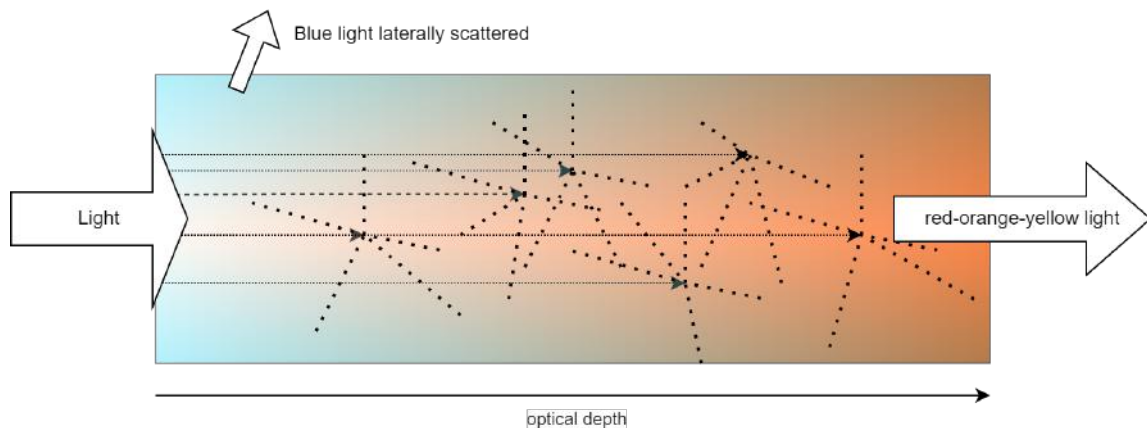
Figure 2.3: Scattering of blue light in the atmosphere [8]. Blue light is scattered stronger in the lateral direction. After a long path through the atmosphere, most of the blue light has been scattered away, which leaves only orange or red light.

The color of the sky is produced by different interactions between the particles in the atmosphere and the incident light. The major interactions are scattering and absorption, with scattering playing
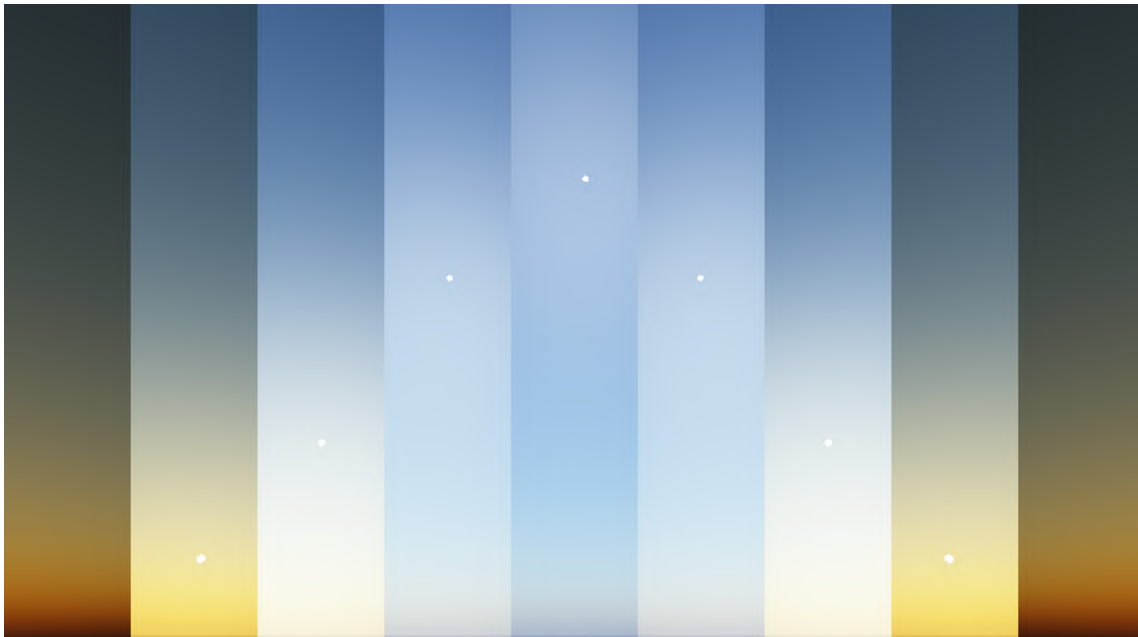
Figure 2.4: Sequence of images showing the colors of the sky rendered with the atmospheric model by *Eric Bruneton* [2].

the larger role. During the daytime, when the sun is high in the sky, the scattering of sunlight results in a blue sky. But when the sun is low and the optical depth is large, most of the blue light is scattered away, which results in a red or orange sun (see **Figure 2.3** and **2.4**). The process of removing blue light is called reddening and vice versa, the removal of red light from the light ray is called bluing.

Scattering by Air Molecules   Different particles have different scattering properties. When the particles are much smaller than the wavelength, the scattered light is highly isotropic. The strength of the so-called Rayleigh scattering is highly dependent on the wavelength, although the directional dependency is independent of the wavelength. Shorter wavelengths are scattered much stronger than longer ones [2]. Scattering in general is proportional to the density of the molecules, which is generally decreasing exponentially with altitude [2].

Scattering by Aerosols   Aerosols, which generally have a much larger radius compared to the wavelength, scatter light in a much more complex way. This type of scattering is traditionally called Mie scattering [2]. The scattering direction is highly anisotropic and can even depend on the wavelength, although in the context of the Earth's atmosphere, it is not. Scattering occurs in a strong forward-direction, so almost no effect of Mie scattering can be seen at larger scattering angles. That is why the bright glow around the sun has the same color as the sun itself [2].

7

Scattering Intensity   The intensity of **scattered light** at the *distance r* from a particle and at *angles θ* and *φ*, depending on the intensity of the incident light, is defined by:

$$I_{sca} = I_0 \frac{F(\theta, \varphi)}{k^2 r^2}$$

(2.2)

where *θ* is the *angle* between the direction of the scattered and incident light and *φ* is its *azimuth angle*. *k*, the *angular wavenumber* measures *radians per unit distance* of a wave [10].

$$k = 2\pi/\lambda \ (rad * m^{-1})$$

(2.3)

The scattering function $F(\theta, \varphi)$ is dimensionless and expresses the relation between the incident and scattered intensities.

2.1.1 Phase Function

When talking about scattering, it is necessary to characterize how light is scattered in which direction. The directionality is commonly described as the phase function, which can be seen as a spherical probabilistic density distribution [11]. This function is obtained by dividing the scattering function $F(\theta, \varphi)$ by $k^2 C_{sca}$, the *wave number* and *scattering cross-section*, which is defined below[10].

$$\begin{aligned} P(\theta, \varphi) &= \frac{F(\theta, \varphi)}{k^2 C_{sca}} \\ &= \frac{F(\theta, \varphi)}{\int F(\theta, \varphi) d\omega} \text{ where } d\omega = sin(\theta)d\theta d\varphi \\ &= \frac{F(\theta, \varphi)}{\int F(\theta, \varphi) sin(\theta) d\theta d\varphi} \end{aligned}$$

(2.4)

A phase function has no physical dimension, and its integral over all directions is commonly normalized to **1** or sometimes 4π [10, 12].

$$\int_0^{4\pi} \int_0^{\pi} P(\theta, \varphi) \ \sin \theta \ \partial\theta \ \partial\varphi = 1$$

(2.5)

Note that the azimuthal dependence *φ* of *P* is often removed, which is possible under the assumption of a spherical particle.

$$P(\theta) = \frac{F(\theta)}{\int F(\theta) sin(\theta) d\theta}$$

(2.6)

A phase function is often displayed as a polar plot, but most of the time, due to its symmetry, it ranges just from 0° to 180°.

Mie Theory   In order to obtain the phase function there are quite a few approximations which will be discussed in **Section 2.3** but there are also theories which calculate the general scattering properties of different particles. In 1908 the physicist *Gustav Mie* [13] dealt with the problem of scattering and absorption by gold particles suspended in water. This resulted in one of the first general solutions to the problem of scattering of an electromagnetic wave by a sphere [10]. His solution is based on Maxwell's equations and takes the form of an infinite series [9]. The complex amplitude functions S_1 and S_2 are calculated with

$$S_1(\mu) = \sum_n^\infty \frac{2n+1}{n(n+1)} (a_n\,\pi_n(\mu) + b_n\,\tau_n(\mu))$$

$$S_2(\mu) = \sum_n^\infty \frac{2n+1}{n(n+1)} (a_n\,\tau_n(\mu) + b_n\,\pi_n(\mu)) \qquad \text{where } \mu = \cos(\theta) \text{ [3].} \qquad (2.7)$$

The terms a and b are scattering coefficients and π and τ are angle dependent functions. What these functions look like in detail can be found in the work of *Craig Bohren* and *Donald Huffman* [3]. The important information is that Mie theory enables the calculation of phase functions and scattering and extinction cross-sections based on the incident wavelength, the refractive index and the radius of the particle. It is important to note that Mie theory supports the calculation of only one kind of particle at a time. On the other hand, the scattering behavior of different particles can simply be summed up, although this is only true if the particles in the mixture are reasonably far apart and do not interact with each other. The intensity of unpolarized scattered light can be calculated by

$$I_{sca} = \frac{1/2(|S_1(\theta)|^2 + |S_2(\theta)|^2)}{k^2 r^2} I_0 \qquad \text{where } k = \frac{2\pi}{\lambda}. \qquad (2.8)$$

The extinction and scattering cross-sections are then given by

$$C_{sca} = \frac{2\pi}{k^2} \sum_{n=1}^\infty (2n+1)(|a_n|^2 + |b_n|^2)$$

$$(2.9)$$

$$C_{ext} = \frac{2\pi}{k^2} \sum_{n=1}^\infty (2n+1) Re\{a_n + b_n\}.$$

Wavelength Dependent Phase Function of a Rainbow   A practicle example for the usefulness of the Mie theory is the scattering calculation of a water droplet, which lets us examine the source of the colors of the rainbow. The refractive index of water is dependent on the wavelength of the incident light. **Figure 2.6** shows the phase function for four wavelengths (380, 480, 580 and 680 nm) of a 100 μm large water droplet. The enlarged view from 125° to 140° shows the part of the scattering direction that is responsible for the colors of the rainbow. The main rainbow can be seen at around 138° and the secondary rainbow at around 128°. Between them lies the so-called Alexander's dark band, which can be seen in **Figure 2.5**. Due to the wavelength dependent refractive index,

Figure 2.5: Image of a Rainbow [14].

the local maxima of the different wavelengths are shifted, which means
that different wavelengths are scattered in different directions. Note that the red peaks in the phase
function are positioned towards the dark band, just as in the image of the real rainbow. In case of
a water droplet, the phase function can be explained visually by the fact that photons are reflected
internally multiple times before they exit the droplet. How often they are reflected depends strongly
on the incident angle, the refractive index of water for the specific wavelength and the radius of the
droplet.
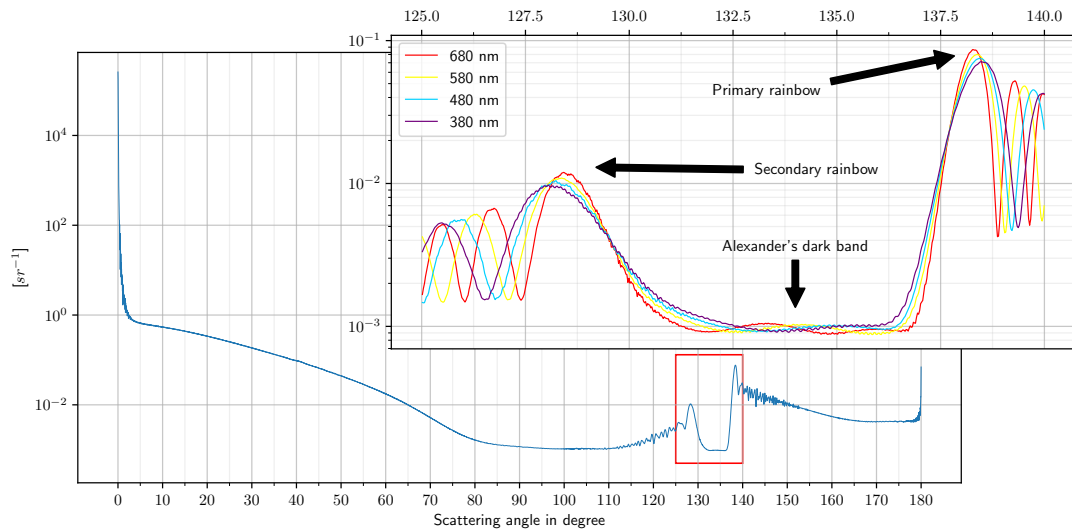
Figure 2.6: Phase functions of a rainbow calculated with Mie theory for different wavelengths. The
enlarged view shows the phase function in the range from 125° to 140° for four wavelengths. The
Graph in the background shows the curve of the combined phase function.

2.1.2 Cross-Section

Another property of particles is their geometrical cross-section G [10]. For a simple sphere, it is
given by

$$G = \pi r^2. \tag{2.10}$$

The *scattering cross-section C_{sca}* is a measure of how much of the incident energy is scattered
away. The total energy that is scattered away is equal to the energy of the incident light that would
fall onto the area C_{sca}. If C_{sca} is equal to the area of the *geometrical cross-section ($C_{sca} = G$)*, all
the incident energy would be scattered away. Using the **Equation 2.4** the *scattering cross-section*
is defined as the total energy scattered in all directions:

$$C_{sca} = \frac{1}{k^2} \int F(\theta, \varphi) d\omega \ (m^2) \text{ where } d\omega = sin(\theta) d\theta d\varphi \tag{2.11}$$

Energy that is absorbed is measured by the *absorption cross-section* C_{abs}, which has the same geometric meaning. If all the energy was absorbed by the particle, then C_{abs} would be equal to G.

The *extinction cross-section* C_{ext} is the sum of C_{sca} and C_{abs} and describes how much of the incident energy is removed from the light, either by *absorption* or *scattering*.

$$C_{ext} = C_{abs} + C_{sca} \tag{2.12}$$

Efficiency Factors In contrast to the cross-sections of a particle, the efficiency factor Q expresses the relation of the before mentioned cross-sections to the geometrical cross-section G [10]. Q is a dimensionless constant for each particle and is calculated by:

$$\begin{aligned} Q_{ext} &= C_{ext}/G \\ Q_{sca} &= C_{sca}/G \\ Q_{abs} &= C_{abs}/G \end{aligned} \tag{2.13}$$

Just as the individual cross section can be summed up, the same holds for the efficiency factors:

$$Q_{ext} = Q_{abs} + Q_{sca} \tag{2.14}$$

2.1.3 Volume Scattering Coefficient

In the context of atmospheric scattering, it is useful to not only have scattering properties of a single particle, but for a whole volume. For a given volume V, all areas of the individual *scattering cross-sections* of the particles can simply be added up [9].

$$\beta_{sca} = \frac{\sum_{i=1}^{n} C_{sca}^{i}}{V} \, [m^{-1}] \tag{2.15}$$

Doing the same with the *extinction cross-section* leads to the *volume extinction coefficient*. This coefficient describes the fractional power loss per unit length. The *volume coefficients* can be converted from the *standard air reference* to any temperature and pressure using the following formula [15]:

$$\beta = \beta^s \frac{P}{P_s} \frac{T_s}{T} \qquad \begin{aligned} &\beta^s : \text{volume coefficient of standard air} \\ &P_s = 1013.25 mbar : \text{reference pressure a which } \beta_S \text{ was measured} \\ &T_s = 288.15K : \text{reference temperature a which } \beta^s \text{ was measured} \end{aligned} \tag{2.16}$$

The ratio between the energy of the incident and exiting light is expressed by Beer-Lamberts law [9]. The *volume scattering coefficient* is also known as the *attenuation coefficient* [16].

$$\frac{P}{P_0} = e^{-\beta_{ext} z} \qquad \begin{aligned} &\beta_{ext} : \text{extinction cross section} \\ &P_0 : \text{radiant power of the incident light} \\ &P : \text{power after the beam travels a distance z} \\ &z : \text{distance} \end{aligned} \tag{2.17}$$

The *volume coefficients* can also be obtained by

$$\beta_{sca} = C_{sca} \cdot N_0 \tag{2.18}$$

where N_0 is the number density [number of molecules $/cm^3$] at sea level. For Rayleigh scattering on the Earth $N_0 = 2.68731 * 10^{19} cm^{-3}$ [17].

2.1.4 Optical Depth & Transmittance

Additionally to scattering, a fraction of the light can also be absorbed. This is usually not the case for molecules, but for large aerosols in the atmosphere. The attenuation of light traveling a distance S through the atmosphere is calculated by the integral over all *volume extinction coefficients β_{ext}* times the *density ratios ρ* at the given heights in the atmosphere. This is then called the *optical depth t* [16].

$$t(S, \lambda) = \int_0^S \beta_{ext}(s) \, \rho(s) \, \partial s \tag{2.19}$$

For an atmosphere with an exponentially decreasing pressure, the *density ratio* can be calculated by

$$\rho = \exp\left(\frac{-h}{H_0}\right) \qquad \begin{array}{l} \rho : \text{density ratio} \\ h : \text{height above sea level} \\ H_0 : \text{scale height} \end{array} \tag{2.20}$$

where the *scale height* is the height above sea level over which the density falls off by a factor of $1/e$. For Rayleigh scattering in the Earth's atmosphere $H_0 = 7995.75m$ [17]. The **transmittance** expresses the ratio of photons that can travel the distance S without being absorbed or scattered away [18].

$$\tau = e^{-t} \qquad \begin{array}{l} t : \text{Optical depth} \\ \tau : \text{Transmittance} \end{array} \tag{2.21}$$

2.2 Atmospheric Scattering

The intensity of the light that is scattered, at a given altitude h, can be calculated with **Equation 2.22** [19]. The angle θ is the angle between the incident and exiting light directions, and $\theta = 0°$ describes the scattering in the same direction as the incident light (*forward scattering*). All atmospheric models mentioned in this thesis base their calculations on these equations, either at runtime or in a pre-computation phase.
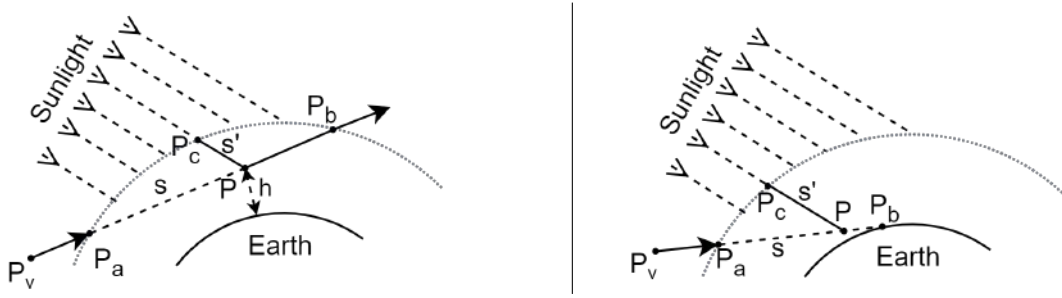
Figure 2.7: Intensity calculation for the ray intersection only with the atmosphere (left) . Intensity calculation for the ray intersection only with the Earth [16] (right).

$$I(\lambda) = I_0(\lambda) \ P(\theta) \ \beta(\lambda) \ \rho(h) \tag{2.22}$$

I : resulting intensity

I_0 : incident intensity

P : phase function

β : volume scattering coefficient

ρ : density at height h

Using the previously defined equations, it is relatively easy to calculate the light that will reach an observer at a point P_V, after it has been scattered a single time. If multi scattering is considered, the evaluation is a little more complex, unfortunately, both in algorithmic and time complexity.

In general, the calculation can be differentiated into three cases. If the view ray from the observer does not intersect the atmosphere, no calculation is needed. If the view ray enters the atmosphere at a point P_a and leaves the atmosphere again at a point P_b, no additional light from the Earth's surface has to be taken into account (**Figure 2.7** left diagram) [16]. In the last case, the view ray enters the atmosphere at a point P_a and intersects with the Earth's surface at a point P_b, where the reflected and then attenuated light from the ground has to be added to the total light intensity (**Figure 2.7** right diagram). In all cases, if the observer is within the atmosphere, the point P_a simply coincides with the location of the observer P_V.

No Ray Intersection with the Earth   **Equation 2.23** calculates the intensity of the light that is scattered into the direction of the observer at the point P. To calculate the intensity I_P of the light that reaches the point P, the *optical depth* from point P_c to P has to be taken into account, resulting in the *transmittance* term. The intensity of the light that is scattered into the direction of the observer P_V can then be calculated with **Equation 2.22**, which is the scattering part of the equation. Multiplying this with the Sun's intensity at the top of the atmosphere I_S gives the intensity of the scattered light.

$$I_P(\lambda) = I_S(\lambda) \overbrace{P(\theta)\,\beta(\lambda)\,\rho(h)}^{\text{scattering}}\ \underbrace{e^{-t(PP_c,\lambda)}}_{\text{transmittance}} \qquad (2.23)$$

I_P : intensity of light arriving at P

I_S : Sun intensity at P_C

P : phase function

β : volume scattering coefficient

ρ : density at height h

t : optical depth

Integrating **Equation 2.23** along the path $P_a P_b$ and taking the transmittance from point P to point P_a into account, leads to **Equation 2.24**, which gives the light intensity I_V reaching the observer at P_V, where s is the distance from P to the point P_a.

$$I_V(\lambda) = \int_{P_a}^{P_b} I_P(\lambda)\ \underbrace{e^{-t(P_aP,\lambda)}}_{\text{transmittance from } P \text{ to } P_a}\ \partial s \qquad (2.24)$$

Due to the large distance to the Sun, sunlight can be assumed parallel and the scattering angle θ along the line $P_a P_b$ to be constant. Following this, the phase function is constant along $P_a P_b$ as well and can be evaluated outside the integral, resulting in **Equation 2.25**

$$I_V(\lambda) = I_S(\lambda)\,P(\theta)\,\beta(\lambda) \int_{P_a}^{P_b} \rho(h)\ e^{(-t(PP_c,\lambda)-t(P_aP,\lambda))} \partial s \qquad (2.25)$$

Ray Intersection with the Earth   In case the view ray intersects with the Earth, the equation is almost the same as before. In addition to the light intensity from **Equation 2.25** I_V, the light I_e reflected from the Earth into the observer's direction has to be added. Considering how much of this light actually reaches the observer by multiplying it with the *transmittance* from P_a to P_b, gives the following equation:

$$I_V'(\lambda) = I_V(\lambda) + I_e(\lambda)\ e^{-t(P_aP_b,\lambda)} \qquad (2.26)$$

2.3 Common Approximations of Phase Functions and Scattering Coefficients

The accurate calculation of phase functions and scattering coefficients can be computationally very expensive. Previous studies have found numerous approximations for specific types of particles which match their exact solutions quite well. The following section describes a number of these approximations which are commonly used in atmospheric models.
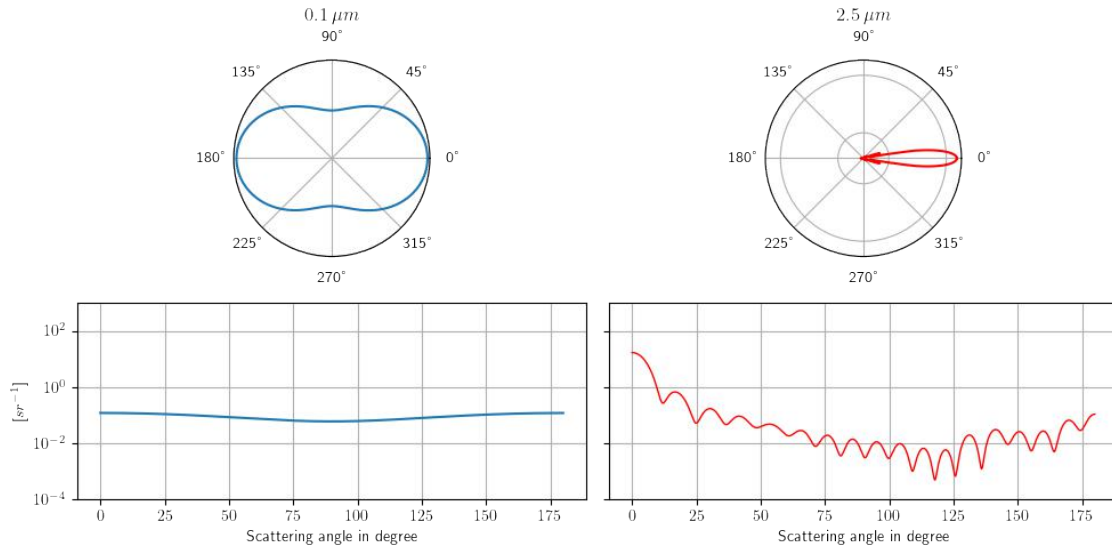
Figure 2.8: Phase functions for a 0.1 µm and 2.5 µm small particle at 450 nm calculated with Mie theory. The functions are normalized to one.

Large vs. Small Particles With the results obtained from the Mie theory, it is possible to analyze different kinds of particles. One of the most important distinctions is the size of the particle. Two example phase functions for particle sizes of 0.1 µm and 2.5 µm are shown in **Figure 2.8**. Small particles have an almost isotropic phase function for which light is scattered almost equally in all directions, whereas larger particles have a highly anisotropic phase function which often has a strong forward scattering peak. Large and small refers to the relative size of the particle compared to the incident wavelength.

Scattering by larger particles is generally much more complex, and it is not possible to give a general analytical phase function. As shown in **Section 2.1.1**, it is possible to calculate the phase function for particles of various shapes, diameters and refractive indices using the Mie theory.

In case of the Earth's atmosphere, light is attenuated and scattered by various different gases and aerosols. Traditionally, scattering in the atmosphere is calculated for small molecules like CO_2 ($I_{Rayleigh}$) and for large particles like dust (I_{Mie}) individually [19]. The sum of all individual scattering calculations results in the total intensity I_{total}.

$$I_{total} = I_{Rayleigh} + I_{Mie} \qquad (2.27)$$

Depending on the size of the particle relative to the wavelength and the difference of the refractive index of the particle compared to the surrounding medium, different approximations can be made. Which approximation is applicable in which case has been worked out by *Hendrik Christoffel van de Hulst* [10]. Small particles, for example with an arbitrary refractive index, can be approximated with the formula by Lord Rayleigh.
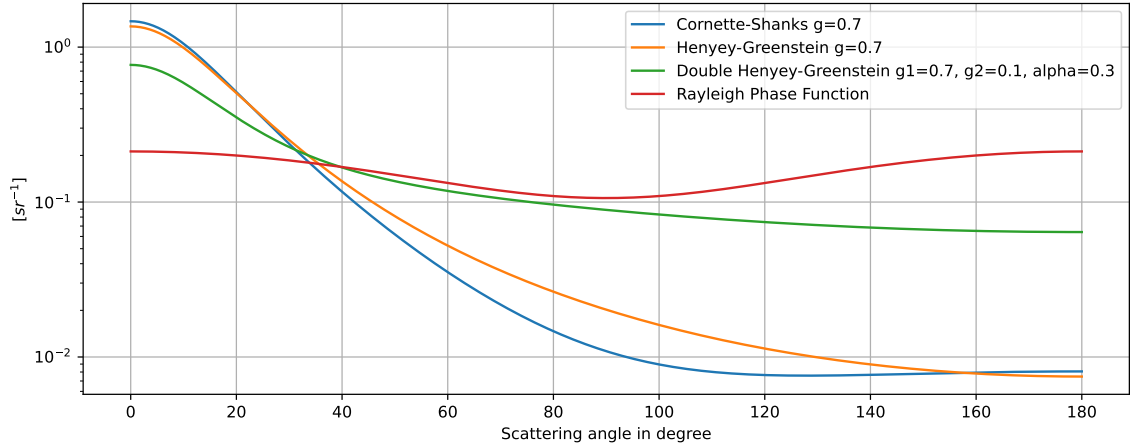
Figure 2.9: Comparison of different phase function approximations (Cornette-Shanks Henyey-Greenstein, Double Henyey-Greenstein and Rayleigh) normalized to 1 over 4π sr.

2.3.1 Rayleigh Scattering

The **Rayleigh phase function** for particles that are much smaller than the wavelength, is independent of other factors like the wavelength and can be described by the formula [10]

$$P(\theta) = \frac{3}{16\pi}(1 + \cos^2(\theta)).$$ (2.28)

2.3.2 Henyey-Greenstein

The most widespread analytic function is the Henyey-Greenstein phase function. The *Henyey-Greenstein* phase function is a relatively simple expression. The curve can be controlled by a single parameter g [20].

$$P_{HG}(\mu, g) = \frac{1 - g^2}{(1 + g^2 - 2g\cos(\theta))^{3/2}}$$ (2.29)

Unfortunately, the function does not reduce to a physically sensible phase function for small particles in the Rayleigh regime. It can also only produce either a forward or a backward scattering peak [20].

2.3.3 Double Henyey-Greenstein

An improvement is the *Double Henyey-Greenstein* phase function, which combines two *Henyey-Greenstein* phase functions and mixes them with a parameter f. In total, three parameters are needed: g_1, g_2 and f [20].

$$P_{DHG}(\mu, f, g_1, g_2) = (1 - f)P_{HG}(\cos(\theta), g_1) + fP_{HG}(\cos(\theta), g_2), \quad \text{where } g_1 > 0, g_2 < 0$$
(2.30)

2.3.4 Cornette-Shanks

William M. Cornette and *Joseph G. Shanks* proposed a more realistic and still simple analytic phase function with a single parameter $g \in (-1, 1)$. If $g \rightarrow 0$ the function converges to the Rayleigh phase function and if $g \rightarrow 1$ it approaches the *Henyey-Greenstein* phase function [20].

$$P(\theta, g) = \frac{3(1 - g^2)}{2(2 + g^2)} \frac{(1 + \cos^2 \theta)}{(1 + g^2 - 2g \cos \theta)^{3/2}}$$
(2.31)

The *Cornette-Shanks* phase function gives a more realistic description of scattering by small particles, but it has the same shortfalls as the *Henyey-Greenstein* phase function for larger particles. Also, neither of these functions is able to produce the sharp forward scattering peak which can be observed in measurements [20].

2.3.5 Anomalous Diffraction Approximation

Larger spherical particles which fall into the Mie scattering regime, with a refractive index close to one, can be approximated by the **anomalous diffraction approximation**. The before mentioned extinction efficiency factor Q_{ext}, which expresses how much of the incident light is either absorbed or scattered away, can be calculated by the formula derived by *van de Hulst* [10]:

$$
\begin{aligned}
Q^{ext}(\lambda, \rho(r)) = {}& 2 - 4e^{-\rho(r) \tan \beta} \frac{\cos \beta}{\rho(r)} \sin (\rho(r) - \beta) \\
& - 4e^{-\rho(r) \tan \beta} \left(\frac{\cos \beta}{\rho(r)}\right)^2 \cos (\rho(r) - 2\beta) \qquad \rho(r) = \frac{4\pi}{\lambda} r \cdot (m(\lambda) - 1) \\
& + 4 \left(\frac{\cos \beta}{\rho(r)}\right)^2 \cos 2\beta \qquad\qquad\qquad\qquad\quad r : \text{particle radius}
\end{aligned}
$$
(2.32)

In case the sphere is non-absorbing, the formula is much simpler:

$$Q^{ext}(\lambda, \rho(r)) = 2 - \frac{4}{\rho} \sin \rho + \frac{4}{\rho^2}(1 - \cos \rho)$$
(2.33)

Some of these approximations are used more often than others. It is quite common to use the Rayleigh phase function for gases in the atmosphere and the Cornette-Shanks phase function for larger particles. The next section discusses the physical units which are used in these light scattering calculations and how they compare to the sensitivity of the human eye.

Quantity	Radiometric term	Units	Photometric term	Units
Energy	Radiant energy Q_e	J (Joule)	Luminous energy Q_v	$lm \cdot s$
Power	Radiant flux Φ_e or radiant power	$\frac{J}{S}$ or Watt (W)	Luminous flux Φ_v or Luminous Power	Lumen (lm)
Power per solid angle	Radiant intensity I_e	$\frac{W}{sr}$	Luminous intensity I_v	$\frac{lm}{sr}$ or Candela (cd)
Power per area	Radiant existence M_e or Irradiance E_e	$\frac{W}{m^2}$	Luminous existence M_v or Illuminance E_v	$\frac{lm}{m^2}$ or Lux (lx)
Power per area per solid angle	Radiance L_e	$\frac{W}{m^2 sr}$	Luminance L_v	$\frac{lm}{m^2 sr} = \frac{cd}{m^2}$ or Nit (nt)

Table 2.1: Radiometric and photometric quantities listed by *Sébastien Lagarde* and *Charles de Rouseier* [21].

2.4 Common Units for Light Measurements

The calculations in physically based atmospheric models use real physical units. In their paper about "Moving Frostbite to Physically Based Rendering 3.0" *Sébastien Lagarde* and *Charles de Rouseier* from Electronic Arts gave an in depth explanation of the different units related to light measurements [21]. These are split into two categories: radiometric and photometric units. Radiometric units deal with physical quantities and optical radiation measurements. Photometric units on the other hand are only concerned with radiation in the visible spectrum. Loosely speaking, photometric units are radiometric units weighted by the sensitivity of the human eye. An overview of common units is given in **Table 2.1**.

After calculating the scattering effects in the atmosphere for various wavelengths, these wavelengths need to be converted to *RGB* values which are finally going to be displayed on the screen. For this, the sensitivity of the human eye to certain colors has to be taken into consideration, which is described by the CIE photometric curve. The human eye is most sensitive to the color green, at 555 nm at which the sensitivity curve has the value one, meaning 100% efficacy. The constant factor K_m is the maximum spectral luminous efficacy. The relationship between photometric and radiometric quantities can then be expressed by the integral

$$X_V = K_m \cdot \int_{380}^{780} X(\lambda)\, V(\lambda)\, \partial\lambda$$

K_m : maximum spectral luminous efficacy
V : CIE photometric curve
X : radiometric quantities

over the visible spectrum [21].

18

3 Related Work

This chapter discusses the properties of the Earth's atmosphere and how they are modeled in various different atmospheric computer graphic models. These models are evaluated on how well they could match the desired properties of a real-time physically based atmospheric model of the martian atmosphere.

Then the known properties of the martian atmosphere are discussed, based on a number of measurements taken by several martian rovers, landers, and orbiters. The studies cover measurements of the phase function of martian dust and suggestions for martian dust analogues, including their phase functions and refractive indices. Then, already existing models of the martian atmosphere are evaluated.

3.1 Atmosphere of the Earth

The atmosphere of the Earth consists of single atoms, molecules, water droplets, ice crystals and aerosols. Atmospheric air is a mixture of many gases [5]. The most common ones are shown in **Table 3.1**. Atmospheric air has a strong spatial and temporal fluctuation caused by the variable water vapor content, which is commonly described as humidity. Many physical quantities, like the refractive index, depend on the humidity. Because water molecules (H_2O: $18.015g/mol$) weigh less than oxygen (O_2: $31.998g/mol$) and nitrogen (N_2: $28.014g/mol$) molecules, humid air has a lower density than dry air. Dry air also has a lower refractive index than humid air [5].

In the atmosphere, water is present in liquid, gaseous and solid form (ice crystals). Water drops form through condensation of water vapor and grow larger and larger by colliding with each other. Their size can range from a few micrometers to many millimeters [5]. The average sizes of water drops are listed in **Table 3.2**.

Name	Abbreviation	Volume fraction
Nitrogen	N_2	78.08%
Oxygen (2018)	O_2	20.95%
Argon	Ar	0.95%
Carbon dioxide	CO_2	0.0400%
Neon	Ne	0.0018%
Helium	He	0.0005%
Methane	CH_4	0.0002%

Table 3.1: Average composition of pure dry air [5].

Type	Radius (μm)	Quantity (cm^3)	Average density (g/m^3)
Fog	$10 - 20$	$1 - 500$	$0.1 - 0.5$
Cloud drops	$10 - 100$	$1 - 1000$	$1 - 2$
Drizzling rain	$100 - 500$	$0.01 - 1$	$0.1 - 10$
Rain drops	$500 - 5000$	$0.0001 - 0.01$	$0.1 - 10$

Table 3.2: Average water droplet sizes in the Earth's atmosphere [5].

The content of aerosols fluctuates from $1\mu g/m^3$ over the antarctic and the oceans up to $1mg/m^3$ over forest fires or sand storms. The time a particle spends in the atmosphere depends on its size. In the lower atmosphere, particles can stay airborne from days to weeks, whereas they can spend months to years in the upper atmosphere [5].

3.2 Real-time Rendering Models of the Earth's Atmosphere

The physics behind the color of the sky is well understood. Unfortunately, computationally, it is really expensive to compute the color of the sky as a radiative simulation. This led to the design of more efficient but still accurate sky rendering algorithms [2]. Nowadays, there are quite a few different models, with many having advantages and disadvantages over the others. Some can only compute the sky color when the Sun is above the horizon. Some have an excellent time complexity but only support a viewpoint from the ground, while others support views from any altitude, even from space [2].

The first model developed by *Robert Victor Klassen* in 1987 [22] was based on a ray tracing algorithm and solved the color of the sky as a simplified radiative simulation. *Klassen's* physical sky model unfortunately has a high time and space complexity [23]. In order to mitigate the high computational costs, analytical models have been developed. They try to fit a mathematical function to the result of a radiative simulation or even to real world measurements and simply evaluate this much more simple function at runtime. Unfortunately, most analytical models are limited in their possible viewpoints and suffer from a lower accuracy [2].

3.2.1 Physical Sky Models

On the way through the atmosphere, light is scattered numerous times. Physical sky models try to compute this by simulating scattering and absorption effects caused by different kinds of particles in the atmosphere. Unfortunately, it is not viable to consider any number of scattering events, so most models only consider a few, though it has been shown that higher order scattering events have a decreasingly lower influence [16]. Overall, simulating just a few or even one scattering event results only in a small error [23].

Klassen In the first clear-sky model by *Klassen*, the atmosphere is approximated by multiple layers, with each having a uniform density [22]. Although simple to compute, this led to large

errors near the horizon. The model was also restricted in that it could only produce views from the ground [16].

Nishita93   The successor to *Klassen's* model, the model by *Nishita et al.* [16], is also based on a numerical integration of the single scattering equation. They improved on the model by *Klassen* by representing the atmosphere as spherical shells with a continuous density and precomputing the optical depth between the Sun and each point P in the atmosphere.
Taking a cylinder with a radius C_j, oriented towards the Sun with its center coinciding with the Earth's center, all points P intersecting along the perimeter of the cylinder and a shell at height r have the same optical depth [16]. P and P' have the same optical depth because light rays coming from the Sun can be considered to be parallel [16]. After precomputing all optical depths into a 2D Matrix with a reasonable resolution of C_j and r, getting the optical depth from any point P to the Sun is as simple as reading the value from this lookup table. The model by Nishita et al. supports rendering of the sky from any viewpoint, even from space, but ignores multiple scattering, which induces a small error in comparison with real-world data. The brightness of the sky is generally underestimated [2]. It is also the simplest numerical model.

Nishita96   The *Nishita96* model is an extension to the *Nishita93* model and adds multiple scattering. At daytime, the effects of multiple scattering can be neglected, but especially during twilight, when the path through the atmosphere is long, multi scattering has a large influence [24]. Calculating double scattering normally requires the calculation of an integral over all directions at each sample point along the view ray, resulting in an additional triple integral at each sample [2]. *Nishita et al.* reduce the sampling over all directions to only eight directions, and precompute the single scattering into large 3D matrices. The *Nishita96* model increases the overall accuracy, but still underestimates the measured values. Due to the nature of the precomputed 3D matrix, possible viewpoints are limited to the ground [2].

O'Neal   The atmospheric model by *Shean O'Neil* [25] from 2005 was one of the first models to run at interactive frame rates on a GPU. It supports all viewpoints from ground to space and allows all Sun directions, but only accounts for single scattering [2]. It is based on *Nishita93* with the difference that the precomputed transmittance table is replaced by an analytic approximation. To improve the transmittance calculation further, only one scale height is used, which cuts the amount of calculations in half. So it is not only faster to evaluate, but does not even need a pre-computation phase. Unfortunately, due to these approximations, the model underestimates the radiance by a large factor [2].

Haber   Like *Nishta96*, the model by *Jörg Haber* [24] from 2005 also precomputes multiple scattering in a 3D grid, but unlike *Nishta96's* Cartesian coordinates, *Haber* uses spherical coordinates centered on the viewer. Like *Nishita96*, values are only precomputed for a specific Sun zenith angle and viewer altitude [2]. In a view from space, different positions in the atmosphere with different Sun zenith angles would be visible at the same time, so *Haber's* model is limited to views from the ground. But unlike other models, *Haber* accounts for the refractive index of the air, which makes

curved light paths possible. The absorption of Ozone is also accounted for [2]. *Haber's* model takes more scattering orders and more directions into account, so in comparison to *Nishita96*, *Haber's* model delivers better results, but still underestimates the sky radiance [2].

Bruneton   When developing their model in 2008, *Eric Bruneton* and *Fabrice Neyret* had the goal to create a model that is able to render the atmosphere in real time from any viewpoint at any time of the day. They also account for multi scattering and Rayleigh and Mie scattering [26]. Based on the model by *Nishita96 et al.*, *Bruneton* and *Neyret* precompute multiple scattering but instead of doing this for only one Sun zenith angle, they do it for n_{θ_s} Sun zenith angles [2]. They realized this by precomputing most terms of the light transport equation 2.24 into a 4D Matrix. During render time, they can evaluate the model in constant time, without any sampling [26]. Just as *Nishita et al.*, *Bruneton* and *Neyret* use the Rayleigh and Cornette-Shanks phase function, but unlike the eight directions in *Nishita et al.'s* model, they compute multi scattering over all directions [16, 26]. Close to the Sun, the model usually underestimates the sky radiance but overestimates it near the horizon. *Bruneton* and *Neyret* suggest that this could be caused by the missing strong forward scattering peak in the Cornette-Shanks phase function [2]. An extension of *Bruneton's* model was developed by **Oskar Elek** and *Petr Kmoch* in 2010. Besides other improvements, their main difference is the number of samples in the visible spectrum. *Bruneton et al.* only consider three wavelengths, but *Elek at al.* take 15 samples into account.

3.2.2 Analytical Sky Models

Analytical models try to overcome the large computational cost of physical sky models and trade customizability for performance. These models are usually realized as an equation which approximates a realistic clear sky. The first analytical model was developed by *Arcot J. Preetham* in 1999 [27]. The advantage of analytical models is, that they are really fast to evaluate, although they suffer from a lower accuracy [27]. Most analytical models are also limited in their viewpoints. *Preetham's* model for example only allows for views from the ground.

Preetham   Based on *Nishita96*, *Preetham* calculated the sky radiance for many view and Sun directions. These results were then fitted to an analytical function using least square fitting [2]. *Preetham's* model has only one parameter, the turbidity, which describes the cloudiness or haziness of the atmosphere. The other usual parameters such as the solar spectrum, ground albedo or phase functions are ignored [2]. *Preetham's* model is limited to views from the ground, mainly because it was fitted for an observer on the ground. The solar zenith angle is also limited to be over the horizon. The sky radiance during twilight deviates strongly from daytime, which could not be incorporated into the analytical function. As a result, the model strongly overestimates the sky radiance [2].

Hosek   The model by *Hosek* [28] is much more accurate than *Preetham's* model [2]. Although it is similar, the fitting phase had more degrees of freedom, which resulted in a better matching function. Instead of *Nishita96*, *Hosek* used a computationally much more expensive but more precise path tracer to evaluate the sky radiance. The analytical function itself has more parameters, such as the ground albedo, which allows for a better fit into the scene [2].

Model	Precompute time	Precompute memory	Render time
Nishita93	$O(n^3)$	$O(n^2)$	$O(n)$
Nishita96	$O(n^3)$	$O(n^3)$	$O(n)$
Preetham	0	0	$O(1)$
O'Neal	0	0	$O(n)$
Haber	$O(n^6)$	$O(n^3)$	$O(n^2)$
Bruneton	$O(n^6)$	$O(n^4)$	$O(1)$
Elek	$O(n^6)$	$O(n^4)$	$O(1)$
Hosek	0	0	$O(1)$

Table 3.3: Compelexity analysis of the clear sky models analyzed by *Bruneton* [2].

But just like *Preetham*, the viewpoint is limited to ground level and the solar zenith angle has to be over the horizon. *Hosek's* model still overestimates the sky radiance, but not as much as *Preetham's* model [2].

Conclusion   In 2017 *Eric Bruneton* published a Paper in which he compared eight clear sky models, namely *Nishita93*, *Nishita96*, *Preetham*, *O'Neil*, *Haber*, *Bruneton*, *Elek*, and *Hosek* [2]. He concludes, that numerical models are generally slower and require a pre-computation phase, but provide more possible viewpoints and more physical parameters. Analytical models, on the other hand, are much faster to evaluate, but lack the flexibility of numerical models [2]. *Bruneton* suggests that ". . . adding more aerosol parameters in the computer graphic models is the best way to significantly increase . . . " the accuracy [2]. "In particular, we think using more realistic phase functions for aerosols is the easiest way to increase accuracy in the solar aureole region [2]." He also concludes that, the fewer approximations are used, the more realistic are the results.

Figure 3.1: Renderings of all models compared by *Bruneton et al.* [2].

3.3 Atmosphere of Mars

	Earth	Mars
Mass ($10^{24}kg$)	5.9722	0.64169
Equatorial radius (km)	6378.1	3396.2
Polar radius (km)	6356.8	3376.2
Surface gravity (m/s^2)	9.80	3.71
Surface pressure (mb)	1014	6.36
Solar irradiance (W/m^2)	1361.0	586.2

Figure 3.2: Image of Mars taken by the Hubble telescope [29].

Table 3.4: Facts about the Earth and Mars [2, 30].

The planet Mars is the fourth planet in our solar system. It has about 10% of the Earth's mass, and its equatorial radius is only 3396.2 km in comparison to the Earth's 6378.1 km. Mars has a much lower gravity of only 3.71 m/s^2 and an average surface pressure of about 6.63mb, ranging from 4 mb to 9 mb depending on the season. With 586.2 W/m^2 the solar irradiance reaching Mars is only 43.1% of that of the Earth [30]. The martian atmosphere contains about 95% Carbon Dioxide, 2.59% Nitrogen, and 1.94% Argon. The remaining molecules are mostly Oxygen, Carbon Monoxide, Water, Nitrogen Oxide and Neon which contribute about 0.25%. The main contributions to scattering in the Rayleigh regime are made by Carbon Dioxide, although, due to the thin atmosphere, Rayleigh scattering contributes < 1% compared to the Earth and can almost be neglected [31, 32].

Name	Abbreviation	Volume fraction
Carbon Dioxide	CO_2	95.1%
Nitrogen	N_2	2.59%
Argon	Ar	1.94%
Oxygen	O_2	0.16%
Carbon Monoxide	CO	0.06%
Water	H_2O	210ppm
Nitrogen Oxide	NO	100ppm
Neon	Ne	2.5ppm

Table 3.5: Gaseous composition of the martian atmosphere [30].

3.3.1 Atmospheric Studies

Tomasko In 1999 *Martin G. Tomasko et al.* published a study in which they characterized the properties of the martian atmospheric dust based on images returned from the Imager on *Mars Pathfinder*. The camera has four optical filters at 444, 671, 896, and 965 nm. Images show the Sun at azimuth angles ranging from 4° to 180° and a Sun elevation of about 15°. From these images (see **Figure 3.4**), *Tomasko et al.* determined the Radiance [$W m^{-2} sr^{-1}$] of the four wavelengths based on available calibration data for the image sensor [34].

Tomasko et al. based their analysis on an atmospheric sky model, which was iteratively fitted against the results of the image analysis. Free parameters of the model were for example the refractive index, the particle size distribution and the total number of particles $/cm^2$ in a vertical column. After fitting the model, they computed the optical depth as a function of number density N and in turn used

Figure 3.3: Image taken by *Pathfinder on Mars* [33].

the optical depth determined by *Lemmon et al.* [32] to calculate the final number density N for their model. Their final results include parameters for the chosen particle size distribution, the refractive index and the phase function.
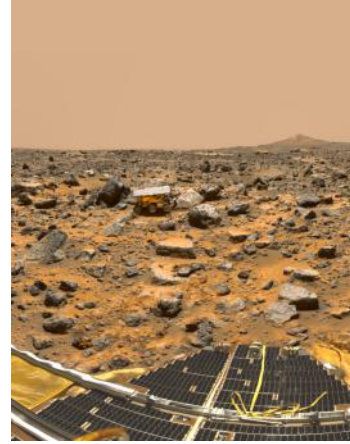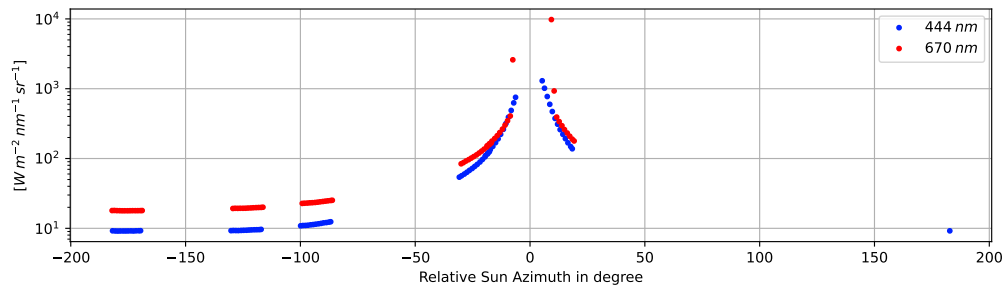

Figure 3.4: Sky radiance from Tomasko [34] for two wavelengths. The measurements have been derived from images taken by images from *Mars Pathfinder*.

Ehlers In 2014 *Kurt Ehlers et al.* [9] investigated the role of dust aerosols in the blue martian sunset. They came to the conclusion that light scattering in the martian atmosphere is much more complicated than on the Earth, due to the fact that the size of the dust particles is very close to the wavelength of the light. They propose that the reddish appearance of the martian dust is caused by the presence of hematite ($\alpha - Fe_2O3$), an iron oxide with a wavelength

Figure 3.5: Sunset at Mars' Gusev crater, taken by the rover spirit [1].

dependent refractive index and a strong absorption of blue light.

Like seen in **Figure 3.5** during sunrise and sunset, both the Sun disc itself and the glow surrounding the Sun show a blue tint. *Ehlers et al.* [9] estimated that the blue cone is most dominant up to 10° around the Sun and decreases up to 28°. They identifed two different processes which cause this effect. The blue color of the Sun's disc is caused by bluing (extinction of larger wavelengths) of sunlight. Unfortunately, the reason for this is not as simple as its counterpart in the Earth's atmosphere, the reddening of sunlight for low solar elevation angles. Reddening simply means, that blue light is scattered or absorbed more effectively than red light, which in turn results in a larger transmittance for red light than for blue light. In the case of the martian atmosphere, *Ehlers et al.* [9] propose that the stronger absorption of blue light may in turn even ". . . enhance bluing by reducing destructive interference of transmitted and diffracted light[9]." This is only possible when particles with an imaginary refractive index, like e.g. hematite, are present. They suggest that this effect may also be seen on Earth during strong dust storms or after volcanic eruptions, when a lot of ash is in the air. In contrast to the wavelength selective extinction of blue light, the blue glow surrounding the Sun is caused by stronger scattering of smaller wavelengths in the near-forward direction, which in turn is caused by the wavelength dependent refractive index. Scattering in the forward direction is mostly a product of diffraction and external reflection.

Dabrowska　Also in 2014 *Dominika D. Dabrowska et al.* [35] analyzed scattering properties of martian dust analogs at $488nm$ and $647nm$. They analyzed montmorillonite, two palagonite samples, basalt, and calcite. As per their results, palagonites and basalt seem to be the best martian dust analogues. This seems quite logical because of past volcanic activities on Mars, which left many basaltic rocks. Their basalt samples were collected on the Tenerife Island in Spain, and their palagonite samples come from the *Johnson Space Center* (JSC) in Houston, Texas. The palagonite samples used in their study have a diameter of less than $200\,\mu m$. Part of the original sample was heat treated in an oven at 200 °C for 24h. The heated sample is called **JSC200** and the non-heated one **JSC0**. Among other results, they measured the particle size distribution and phase function from 3° to 177° for each sample. Afterwards, they compared the phase functions with results produced by applying Mie theory with the same measured size distribution and refractive indices as the samples. They come to the conclusion that realistic poly-dispersions of dust particles **cannot** be replaced by calculations with Mie theory [35].

3.3.2 Properties of the Martian Dust

The size distribution and amount of dust in the air is strongly dependent on the martian weather. Mars is well known for its huge dust storms, which can cover continent-sized areas and can last for up to a few weeks. About every 5^1/$_2$ Earth years, normal storms can grow into planet-encircling dust storms or so-called *global dust storms*, which can reach as high as $60km$. But even during those huge storms, the maximum wind speed almost never exceeds $100km/h$. During dust storms, the visibility is much greater on Mars as compared to dust storm on Earth [36, 37].

Particle Shapes　As part of their analysis, *Dabrowska et al.* took *scanning electron microscope* (SEM) images of their samples, which are shown in **Figure 3.6**. It is obvious that the particles in
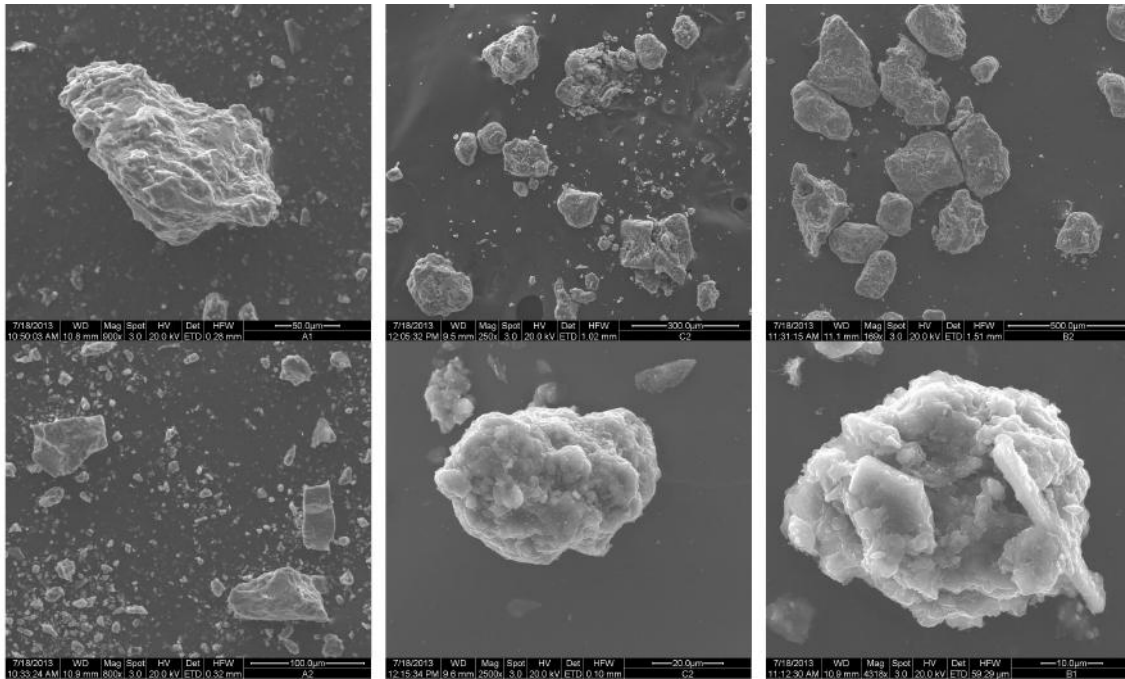
Figure 3.6: Scanning electron microscope images of *basalt* (left), *JSC0* (middle) and *JSC200* (right) taken by *Dabrowska et al.* [35].

their sample are no simple spherical bodies, but have rather irregular shapes. *Dabrowska et al.* also mention that the captured particles are not necessarily representative for the size distribution of each sample. Unfortunately, this shows that it might not be a valid assumption to calculate the scattering of martian dust with a model which uses spherical particles [35]. *Chen-Chen et al.* come to the conclusion that scattering in the martian atmosphere is consistent with non-spherical randomly oriented particles [38].

Particle Sizes The Mars Exploration rover (MER) has shown that the martian surface dust consists of sand-sized particles, ranging from $200 - 300\mu m$ in diameter [35]. The atmospheric dust particle distribution on the other hand is highly variable in time, location and altitude. In times of high transparency, martian dust particles have an effective radius of around, $0.05\mu m$ which can exceed an effective radius of $9\mu m$ during global dust storms [35]. One of the results by *Tomasko et al.* is that dust in the martian atmosphere has a wide distribution of particle sizes. Their calculated size distribution has a mean geometric particle radius of $1.6 \pm 0.15\mu m$ [34]. For the shape of the distribution, they chose the gamma distribution modified by *James E. Hansen* and *Larry D. Travis* in 1974 which was published in their paper "light scattering in planetary atmospheres [39]." The distribution has two free parameters, a the mean cross-section-weighted radius and b the mean cross-section-weighted variance divided by a^2. The distribution itself is given by:
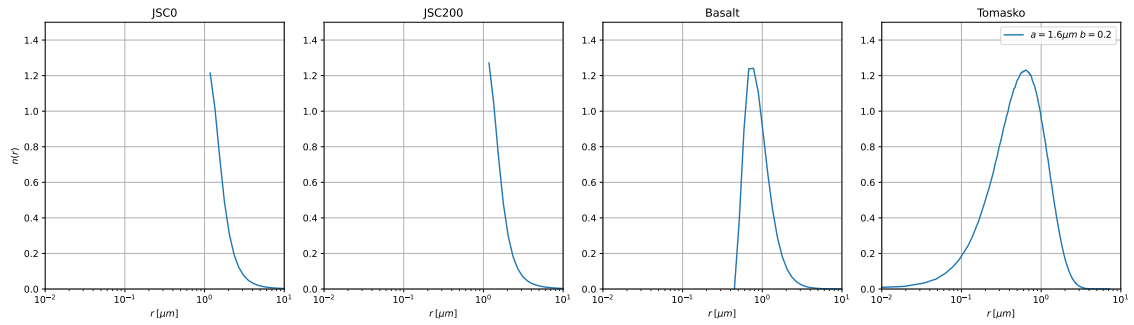
$$n(r) = cr^{(1-3b)/b}e^{-r/(ab)}.$$

Figure 3.7: Measured size distributions of JSC0, JSC200 and Basalt using the Mie method and the gamma distribution from *Tomasko et al.* [34].

The resulting gamma distribution from *Tomasko et al.* with $a = 1.6\mu m$ and $b = 0.2$ is shown in **Figure 3.7**. For comparison, the results of the measured size distributions for the Basalt, JSC0 and JSC200 samples by *Dabrowska et al.* are also shown. The theoretical gamma distribution shows many smaller particles than the samples, especially for the JSC samples. On the other hand, for particles larger than $1\mu m$, the distributions seem to line up quite nicely.

Refractive Index   The refractive index of a particle has a large influence on its scattering properties. For atmospheric models, *Tomasko et al.* generalized that an increase in the imaginary part of the refractive index decreases the overall brightness [34]. According to *Wolff et al.* [40], for martian dust the real part is nearly constant over the whole visible spectrum at around $n = 1.5$. The imaginary part on the other hand is highly dependent on the wavelength. At $400\,nm$ it starts at about $k = 0.014$ and quickly drops to around $k = 0.001$ in the near infrared area. All dust analogues analyzed by *Dabrowska et al.* have an almost constant real and imaginary refractive index over the whole visible spectrum. The only exceptions are JSC0 and JSC200 which have a slightly higher imaginary part for lower wavelengths than for higher. The role of the imaginary part is very important for the scattering extinction curve, as the imaginary refractive index is responsible for the absorption of internally transmitted light [9].
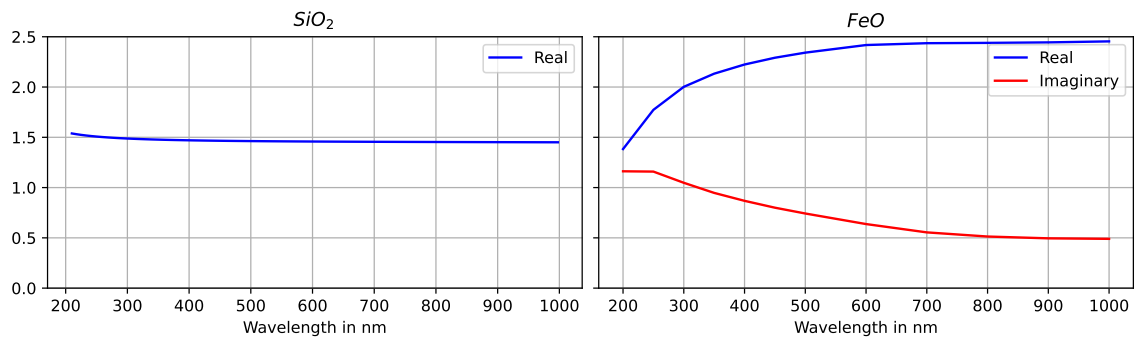

Figure 3.8: Real and imaginary refractive index for Quartz (SiO_2) [41, 42] and Wüstite (FeO) [43].

Typical martian soil is dominated by silicon dioxide SiO_2 (43.7 % by weight) and ferric oxide FeO (21.0% by weight) [44]. Their refractive indices are strongly dependent on the wavelength, as can be seen in **Figure 3.8**. The real part of the refractive index for SiO_2 slowly decreases with wavelength from 1.53 at 210 *nm* to 1.45 at 1000 *nm* whereas the real part of the refractive index of FeO has a steep climb from 1.38 at 200 *nm* to 2.45 at 1000 *nm*. For the visible spectrum, the imaginary part is only available for FeO. It starts at 1.16 and drops to more than half of that.
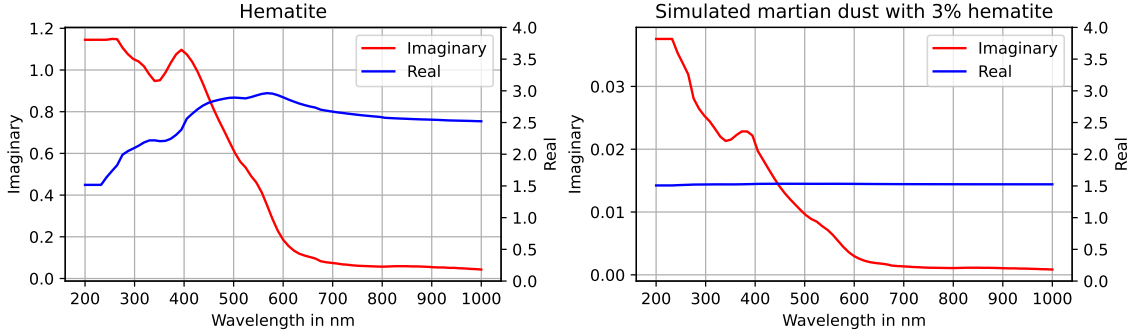

Figure 3.9: Refractive index of hematite [45] (left) and 3% hematite mixed with a non-absorbing substrate with the index of refraction $n = 1.5 + 0i$ [9].

Another candidate for bluing of the extinction curve is hematite ($\alpha - Fe_2O_3$), which has a few deposits on the martian surface. Hematite is an iron oxide which imaginary refractive index is also strongly dependent on the wavelength of the incident light. Hematite has two distinct appearances. Coarse grained particles which have a radius greater than $2.5 - 5\mu m$ appear to be gray. On the other hand, fine-grained hematite particles with a radius of less than $2.5\mu m$ scatter longer wavelengths much stronger, which might explain the red color of the martian surface [46, 9]. Based on the assumption that hematite might also be responsible for the blue color of the martian sunset, *Ehlers et al.* developed a simplified model of Martian dust. For the non-absorbing part of the dust, they chose a substrate with a refractive index of $n = 1.5 + 0i$ which matches the results by *Wolff et al.* [40].

$$n^2 = n_0^2 \frac{n_A^2 + 2n_0^2 + 2v_A(n_A^2 - n_0^2)}{n_A^2 + 2n_0^2 - v_A(n_A^2 - n_0^2)}$$

v_A : volume fraction of absorbing inclusion

n_0 : non absorbin substrate

n_A : absorbing inclusion

Using the *Maxwell–Garnett mixing rule* they computed the refractive index of the resulting dust model, which contains 3% Hematite. By trying multiple different fractions of Hematite (shown in **Figure 3.10**) they settled on 3% which seems to match the most with the results by *Tomasko et al.* [34]. The expected bluing of scattered light can be seen by the positive slope over the visible spectrum, although it is quite obvious that the slope itself is largely independent of the amount of hematite. The amount of bluing is relatively weak and probably not responsible for the blue glow around the Sun.

Phase Function The derived model parameters by *Tomasko et al.* [34] also give a reasonable phase function which is able to reproduce the observed sky radiance. **Figure 3.11** shows their
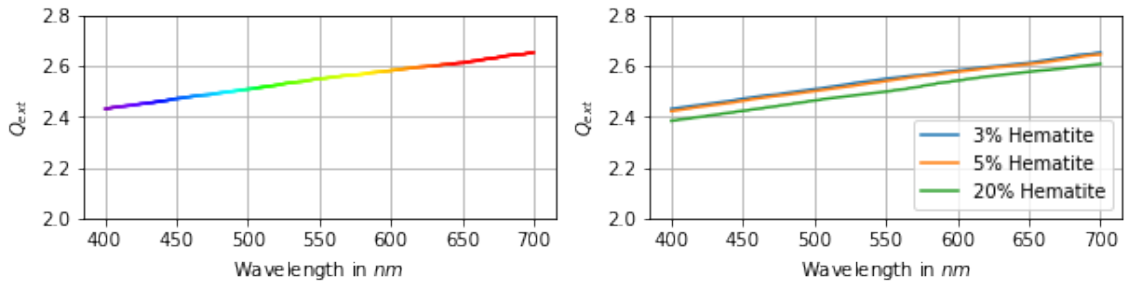
Figure 3.10: Relative intensity for simple dust and a 3% hematite mixture [9].
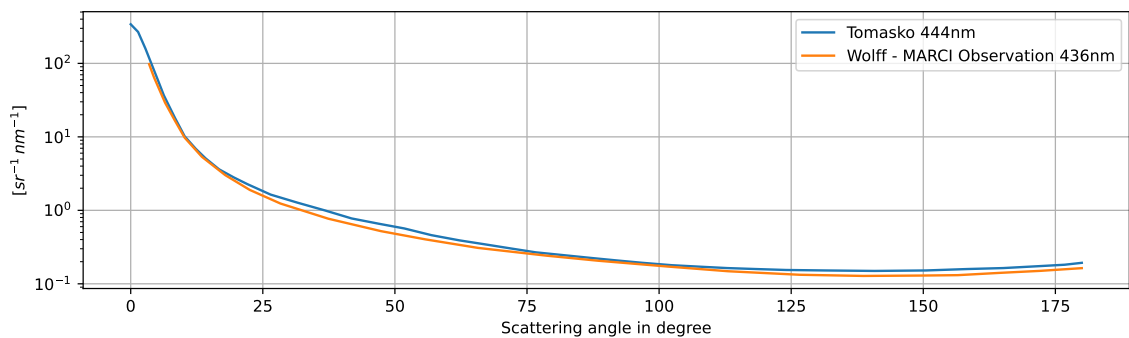

Figure 3.11: Comparison of the phase functions calculated by *Tomasko et al.* [34] and *Wolff et al.* [47]

resulting phase function for 444 nm in comparison to the phase function derived by *Michael J. Wolff et al.* in 2010. Based on observations by the Mars Color Imager (MARCI) on board the Mars Reconnaissance Orbiter (MRO) and its 436 nm color channel, they were able to synthesize an analog for the scattering phase function [47]. Both of these phase functions line up astonishingly well across all directions. According to *Dabrowska et al.* [35] a typical phase function for irregular mineral dust is a smooth function with a steep forward scattering peak and almost no special features at side- and back-scattering, which describes both functions really well.

In their study, *Dabrowska et al.* not only measured the size distribution of the aforementioned samples but also measured their single scattering phase functions, which are shown in **Figure 3.12**. Note that also the martian dust analogues show the desired features; a strong forward-scattering peak and almost no features in the side- and back-scattering area. Shorter wavelengths in the forward scattering area are scattered stronger than longer ones. In the side- and back-scattering area, longer wavelengths are scattered stronger, which is especially true for *JSC0* and *JSC200*. *Dabrowska et al.* also tried to reproduce these functions with Mie theory, which is also shown in **Figure 3.12**. Unfortunately, the desired shape of the curve cannot be reproduced by this. In the forward scattering area the curves match pretty well, but especially in the side scattering area they divert a lot. Even the strong back scattering peak which can be observed in the results for Basalt cannot be seen in the measurements. Another result is, that a small change in the physical properties of the sample, e.g. the size distribution, has almost no effect on the phase function [35].
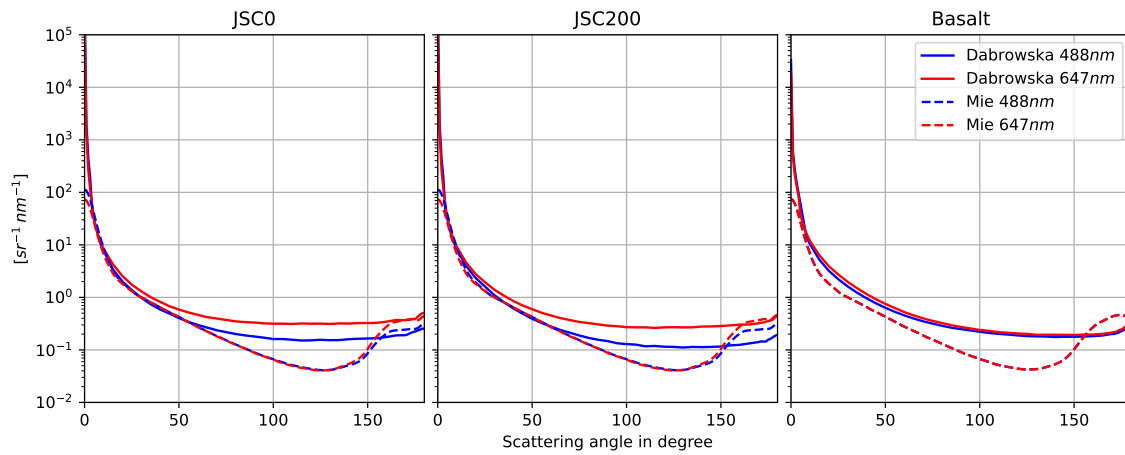
Figure 3.12: Phase functions of JSC and Basalt in comparison with the resulting functions of Mie theory [35].
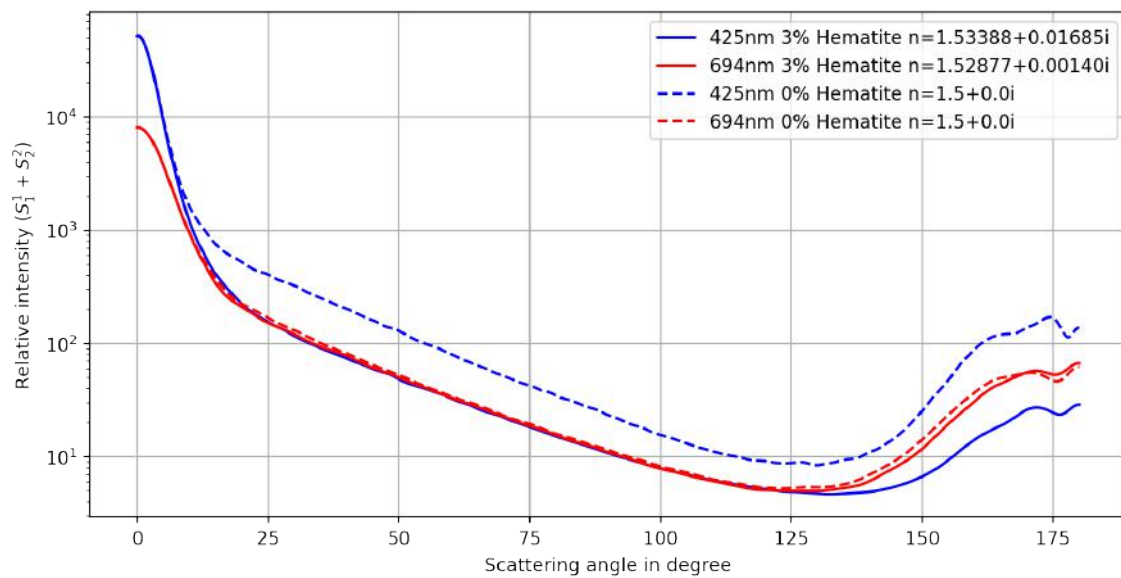

Figure 3.13: Relative intensity for simple dust and a 3% hematite mixture [9].

The intensity function for the simplified martian dust model proposed by *Ehlers et al.* is shown in **Figure 3.13**. The dashed line represents dust containing only a non-absorbing substrate, whereas the solid line shows the intensity function for a mixture containing 3% hematite. Hematite has almost no effect in the forward scattering region, but significantly influences the rest of the function. Like seen in the results of applying Mie theory on the dust analogue samples *JSC* and *Basalt*, the curves have a strong valley in the side-scattering area. With this in mind, the real world measurement of such a sample would most probably not reproduce this valley and look more similar to the flat shape seen at the measured analogues.

3.4 Real-time Rendering Models of the Martian Atmosphere

The goal of this thesis is to develop or extend a physically based real-time rendering model for the martian atmosphere. There have been previous efforts to develop such a model, namely a model by *Peter Collienne* [48] in 2013 and *Jonathas Costa et al.* [31] in 2021.

3.4.1 Collienne

The model by *Collienne* [48] is based on the physical sky model by *Bruneton* [26]. *Collienne* described an implementation of *Bruneton's* model which can even be applied to rough terrain instead of just smooth spheres. They concluded that the Rayleigh and Mie scattering calculations in *Bruneton's* model cannot be adapted to accurately model the physical effects which are responsible for the color of the martian sky. They settled on finding parameters for *Bruneton's* model, which would generate images which look most like the martian atmosphere. Their solution tries to find new parameters for the Rayleigh scattering volume coefficients. Instead of stronger scattering of short wavelengths (blue light), they propose to inverse the effect. This yields a yellowish or reddish sky color during daytime and a bluish sunrise and sunset. The parameters they came up with are listed are as following:

$$\lambda = (440, 510, 680) \times 10^{-9} m$$
$$\beta_R = (5.75, 13.57, 19.918) \times 10^{-3}.$$

(3.1)

The model by *Collienne* is not based on any real physical effects. They simply tried to find scattering parameters that result in a model which looks most alike the martian atmosphere. During daytime, the model matches the expected color of the martian atmosphere quite well. Apart from the blue color, the look of the sunrise and sunset is very different compared to actual images. In their model, the blue color stretches almost along the whole horizon.

3.4.2 Costa

Costa et al. [31] developed a model which can be parameterized to render not only the Earth's atmosphere, but also different planets like, e.g., the martian atmosphere. Like *Colliene*, they also based their atmospheric model on *Bruneton's* work, due to their high performance at runtime with a constant rendering time complexity.
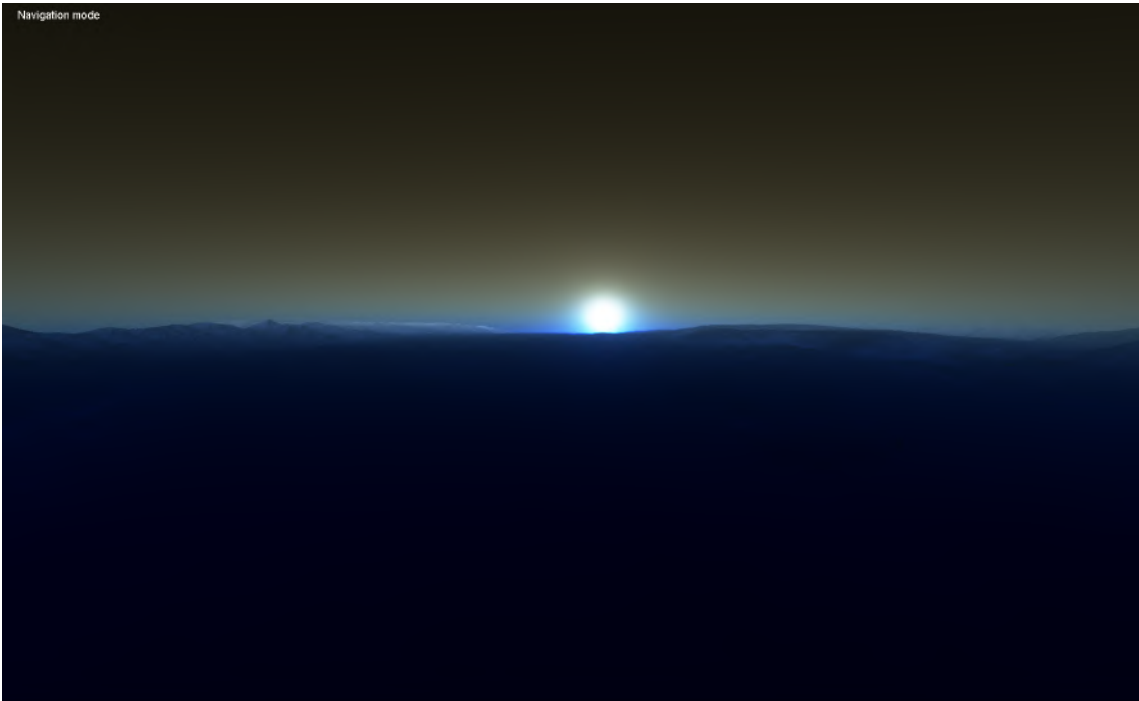
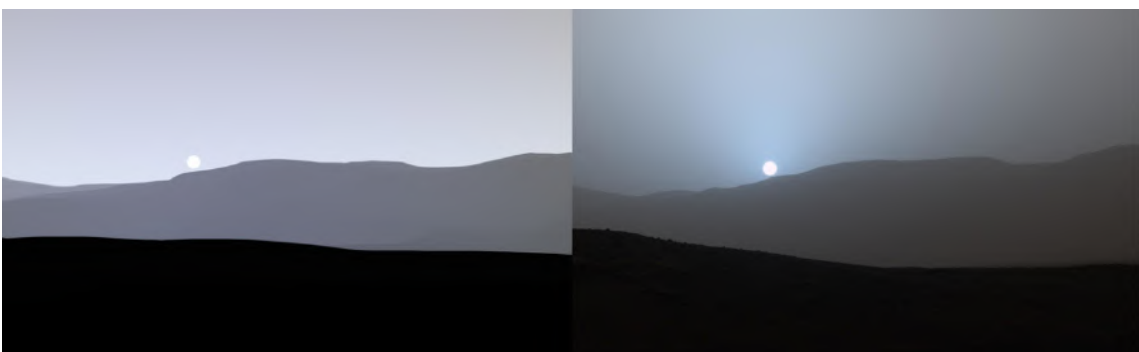Figure 3.14: Martian sunset, rendered by Collienne [48].

Figure 3.15: Rendering by *Costa et al.* [48] compared with an image taken by NASA's Curiosity Mars rover [49].

The model supports a standard and an advanced mode, whereby only the advanced mode is able to render the martian atmosphere. The standard model uses fixed Rayleigh and Mie coefficients (β_R^{sca}, β_M^{scat} and β_M^{ext}). The advanced model extends the model with wavelength-dependent Mie scattering and absorption.

In the advanced mode, the values for Mie scattering and absorption and Rayleigh scattering are calculated based on a few mostly physical parameters. These parameters cover the molecular number density N at ground level, the complex refractive index $n(\lambda)$ for different wavelengths and the particle sizes which are modeled by a gamma distribution (**Section 3.3.2**).

For scattering of atmospheric gases, they use the usual formula for the Rayleigh scattering phase function and scattering coefficients (**Section 2.3.1**). For Mie scattering, they use the double Henyey-Greenstein phase function (**Section 2.3.3**). The wavelength dependent extinction coefficients are calculated by the *anomalous diffraction approximation* (**Section 2.3.5**). The parameters used by *Costa et al.* are listed in **Table 3.7**

λ	wavelength
β	volume scattering coefficient
H	scale height
g_1, g_2, α	Double-Henyey-Greenstein parameters
N	molecular number density
m, k	real and imaginary refractive index
r	particle size
T	turbidity
K	wavelength-dependent fudge factor[50]
v	Junge's exponent [50]
ρ	mean mass density
n	Rayleigh refractive index

Table 3.6: Description of parameters used by *Costa et al.*

Although their advanced approach seems to be physically based, they have tweaked some of these parameters, e.g., the turbidity T, iteratively, until they reached a satisfying appearance of the atmosphere. The parameters g_1, g_2 and α for the double Henyey-Greenstein phase function are based on the analysis of *Chen-Chen et al.* [38] but they found the wavelength dependent parametrization by "experimental findings". In their paper they seem to have provided erroneous values for g_1, g_2 and α. More reasonable values can be found in their implementation published on GitHub [51], which are listed in **Table 3.7** and visualized in **Figure 3.16**.

Conclusion Like the atmospheric model by *Collienne* the model by *Costa et al.* uses the model by *Bruneton et al.* which is computationally very efficient. They correctly modeled the source for the blue glow around the Sun to be caused by a wavelength dependent phase function. This phase function is realized by different parameters for the DHG phase function for all three wavelengths. One disadvantage of the DHG phase function is the fact, that the strong forward scattering peak, which can commonly be observed in the scattering behavior of dust, cannot be achieved. The model is also not really physically correct because many of the parameters like the DHG parameters are user defined.

	Earth	**Mars**
$\lambda [nm]$	$(680, 550, 440)$ (S,A)	$(680, 550, 440)$ (S,A)
$\beta_R^{sca}[m^{-1}]$	$(5.1768, 12.2588, 30.5964) \cdot 10^{-6}$ [15](S)	$(1.2871, 3.0560, 7.6406) \cdot 10^{-3}$ (S)
$\beta_M^{sca}[m^{-1}]$	$4.0 \cdot 10^{-5}$ (S)	-
$\beta_M^{ext}[m^{-1}]$	$0.1 \cdot \beta_M^{sca}$ (S)	-
$H_R[km]$	7.99575 (S) [17]	8.0
$H_M[km]$	1.2 (S) [50]	11.1
g_1	0.85 (S,A)	$(0.03, 0.4, 0.67)$(A)
g_2	0.0 (S,A)	$(0.094, 0.094, 0.094)$(A)
α	1.0 (S,A)	$(0.743, 0.743, 0.743)$(A)
$N[part/cm^3]$(A)	$2.68731 \cdot 10^{19}$	$2.8 \cdot 10^{29}$
$m(\lambda)[nm]$(A)	$(1.00027598, 1.00027783, 1.00028276)$	$(1.52, 1.52, 1.52)$
$k(\lambda)[nm]$(A)	$(0i, 0i, 0i)$	$(0.001i, 0.006i, 0.013i)$
$r[\mu m]$(A)	0.0	1.6
turbidity T	$\in [2, 9]$	$\in [2, 10]$
K	$(0.0096, 0.0092, 0.0089)$	$(0.31, 0.16, 0.27)$
v	4	4
$\rho_{CO_2} [mol \cdot m^{-3}]$	-	$2.8 \cdot 10^{23}$
$n_{CO_2}(\lambda) [nm]$	-	$(1.00044661, 1.00045019, 1.00045558)$

Table 3.7: Parameters used by *Costa et al.* in the standard (S) and advanced mode (A) [31].
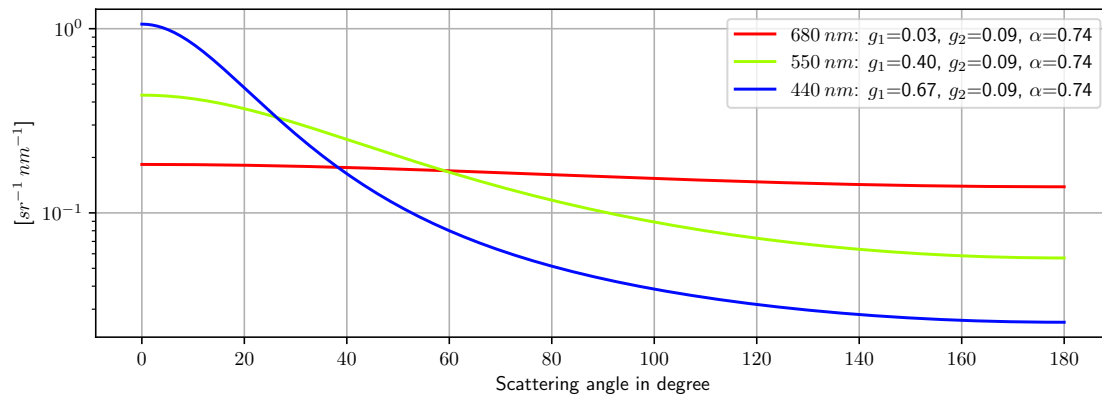
Figure 3.16: Double Henyey-Greenstein phase functions used by *Costa et al.* normalized to one.

4 Design and Implementation

Previous work has shown, that the difference between models and real world measurements is largely caused by the missing strong forward scattering peak of the commonly used Cornette-Shanks or Henyey-Greenstein phase function [2]. In their work, *Bruneton et al.* [2] suggest that a better phase function for scattering by larger particles will most likely improve the overall accuracy of a model.

4.1 Requirements and Improvements of the New Model

Kurt Ehlers et al. [9] concluded that the blue martian sunset is caused by a wavelength dependent phase function for the scattering of dust in the atmosphere. Because the effects which are responsible for the color of the Earth's atmosphere are largely wavelength independent, real-time rendering models for the Earth's atmosphere only support wavelength independent phase functions. One previous martian atmospheric model developed by *Costa et al.* already supports a wavelength dependent phase function in terms of different parameters for the double Henyey-Greenstein function. This analytical phase function on the other hand does not match what previous studies about the martian dust have shown, especially in the forward scattering regime. The model by *Costa et al.* is based on the clear sky model developed by *Bruneton et al.* which has an excellent time complexity and supports multi scattering.

Instead of an analytical phase function, the new model will use a precomputed phase function for every wavelength, which will later be accessed through a lookup table. These phase functions will be calculated by Mie theory with parameters based on previous Martian atmospheric studies about the size distribution and refractive indices. The new model with the lookup table will be implemented in the comparison framework by *Bruneton* [2] and also as a real-time implementation. Just like the model by *Costa et al.* the new model will be based on the clear sky model developed by *Bruneton et al.*

Calculating the new Physical Phase Function   The new phase function will be calculated based on the paper by *Kurt Ehlers et al.* [9]. Consequently, and based on the title of their paper, the new model will be called "Blue Moon's" model. In order to apply Mie theory, a few parameters need to be chosen. Previous work that analyzed the size distribution of the martian dust has been discussed in **Section 3.3.2**. The gamma distribution with $a = 1.6\mu m$ and $b = 0.2$ has been identified to be a good approximation for the size distribution [34].

The simplified dust model by *Kurt Ehlers et al.* [9] uses a wavelength dependent refractive index based on a mixture of a non-absorbing substrate with $n = 1.5 + 0i$ and 3 % hematite. The refractive index of hematite has been analyzed by *Olga Muñoz et al.* [52, 53] and is available in the *Granada – Amsterdam Light Scattering Database*.
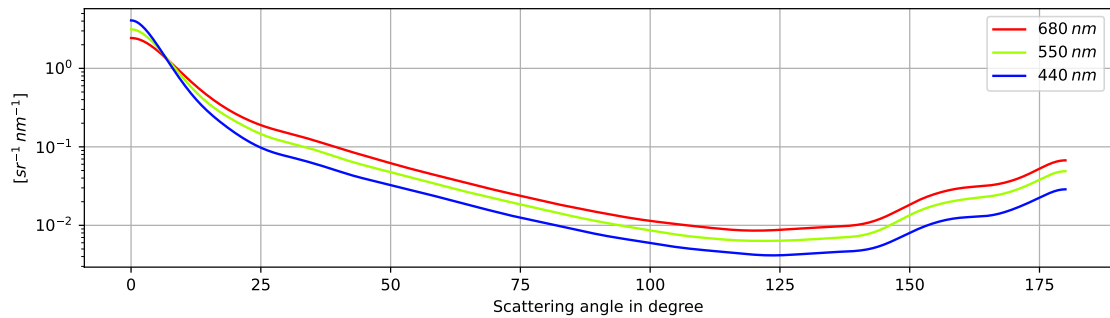
Figure 4.1: Phase function calculated with Mie theory using the parameters provided by *Ehlers et al.* [9].

The python library *Mie Python* is an implementation of the Mie theory [54], which simplifies the calculation a lot. The python code for this is listed in the appendix **Section A.2**. Mie python supports various normalization factors for the phase function. The default implementation normalizes the integral of the phase function over 4π steradians to the single scattering albedo. Dividing the phase function by the single scattering albedo gives the normalization to 1 which is used by the atmospheric models. The single scattering albedo can be calculated by dividing Q_{sca} by Q_{ext}.

The resulting phase function is shown in **Figure 4.1** for three wavelengths. It is notable, that the shorter wavelengths corresponding to a blue color dominate the function in the near forward scattering area. At greater angles, the function is dominated by longer wavelengths, which matches the observed behavior.
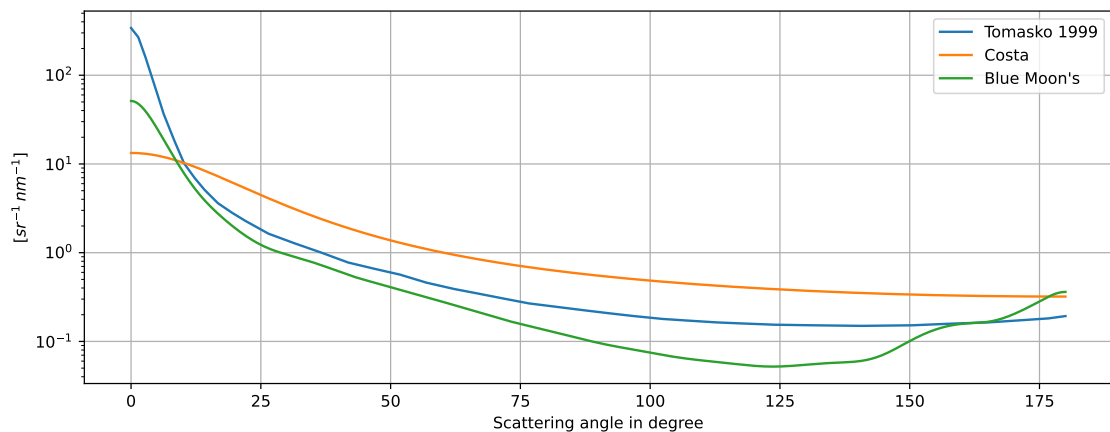

Figure 4.2: Comparing phase functions by Tomasko, Wolff, Costa, and the Blue Moon's phase function at 440 nm normalized to one.

Figure 4.2 shows the phase function in comparison to the previously mentioned phase functions by *Tomasko et al.* and the one used in the model by *Costa et al.* [31]. It is noticeable, that the new phase function calculated with Mie theory has a much stronger peak in the forward scattering area

than the one used by *Costa et al.* On the other hand, the rest of the function, especially the side scattering is much smaller than the measured phase function. With the back scattering strength being about a strong as the function by *Tomasko et al.* the *Blue Moon's* phase function produces a backward scattering peak which cannot be observed in any of the measured data.
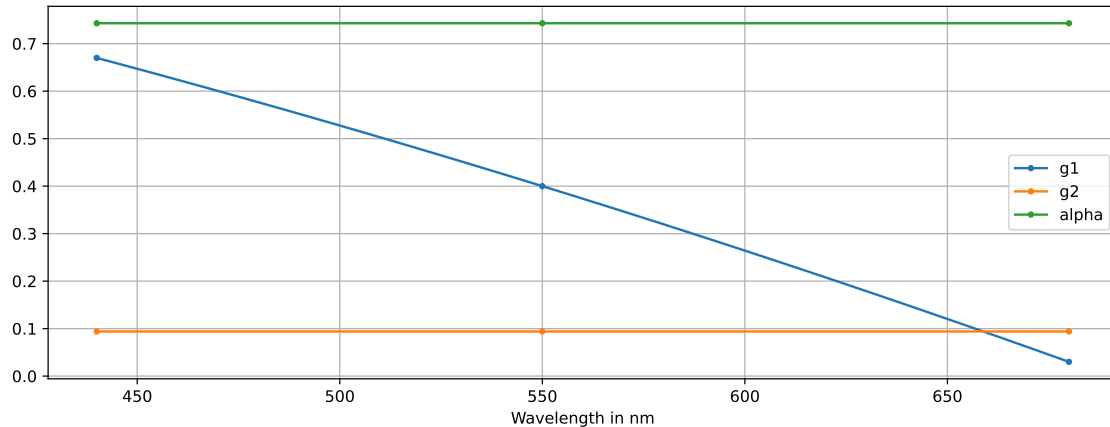

Figure 4.3: Interpolated DHG-Parameters from *Costa et al.*

Combining the Phase Functions into a Hybrid Model   It has been shown that this new *Blue Moon's* phase function is only better in the forward scattering region. One idea is to combine the *Blue Moon's* phase function with the previous phase function by *Costa et al.* to obtain a phase function that has the advantages of both functions, although this *hybrid* phase function wouldn't be based on any physical observations anymore. On the other hand, it has been shown, that a phase function which has been calculated with Mie theory does not match a physically measured phase function, especially in the side- and backwards scattering range in the first place. This is the region in which the values of the DHG phase function used by *Costa et al.* seems to give a better result.

The *hybrid* phase function should combine the strong forward scattering peak of the *Blue Moon's* model with the better fitting model by *Costa et al.* for back- and side-scattering area. One problem is, that *Costa et al.* use only three wavelengths instead of the 48 wavelengths used by the Bruneton comparison framework. The DHG phase function used by *Costa et al.* is parametrized by three parameters, g_1, g_2 and α which are shown in **Figure 4.3**. g_2 and α are constant over the whole spectrum and g_1 can be interpolated with a quadratic function, which has been fitted to the given three parameters with

$$g_1(\lambda) = -1.63170163 \cdot 10^{-6}\lambda^2 - 8.39160839 \cdot 10^{-4}\lambda + 1.35512821 \ .$$

Figure 4.4 shows the phase function by *Costa et al.*, the *Blue Moon's* and the *hybrid* phase functions. A simple linear interpolation seems to give quite promising results, but another method for combining these functions could be investigated in the future. After interpolating between the two original phase functions, the new *hybrid* function has to be normalized again in order to keep the total energy in the system the same. This normalization has to be done for every wavelength.

The *hybrid* phase function has a lower forward scattering peak than the *Blue Moon's* phase function, because the rest of the function is higher and the total area must be the same.
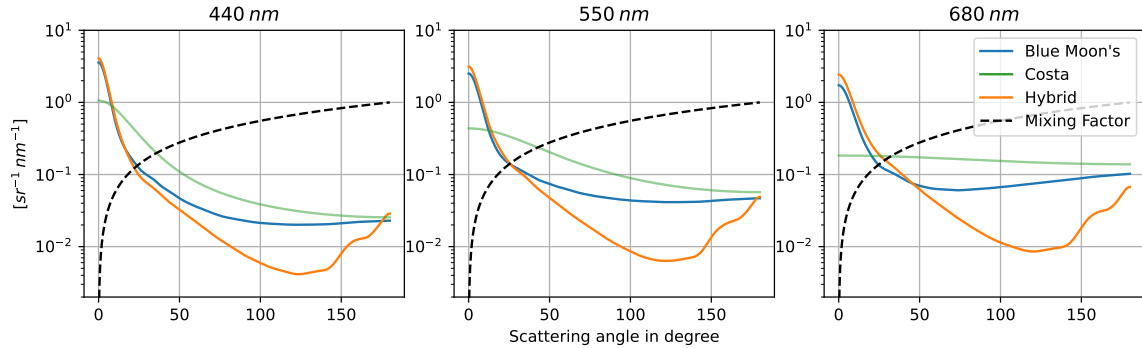

Figure 4.4: Interpolation between the phase functions, resulting in the *hybrid* phase function.

Figure 4.5 shows a contour plot of both, the *Blue Moon's* and the *hybrid* phase function for all wavelengths. The *Blue Moon's* phase function on the left has a much stronger valley at around 120° up to a wavelength of almost 600 nm. The contour plot of the *hybrid* phase function on the other hand is much smoother in the side and back scattering region and shows almost no back scattering peak.
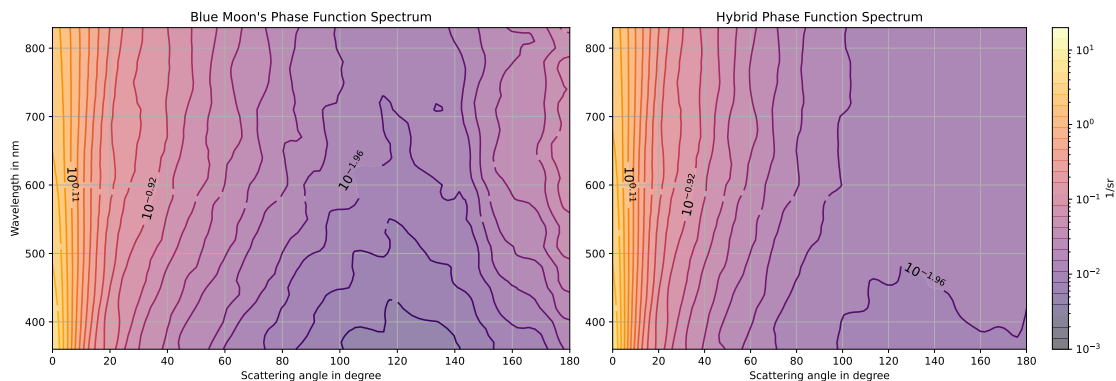

Figure 4.5: Contour plot of the *Blue Moon's* phase function and the *hybrid* phase function for all supported wavelengths from 0° to 180°.

4.2 Bruneton's Comparison Framework

Eric Bruneton [2] published a paper in which he compared eight clear sky models for the Earth's atmosphere. For this, he developed a comparison framework in which he implemented these models. To rule out any problems with more or less accurate approximations, his framework is structured in such a way, that all these models use the same atmospheric properties of the Earth. The framework can analyze the radiance and chromaticity of different models and generate color images. It is also

possible to compare the models with real world measurements. The framework is implemented in *C++*.

The framework delivers a good environment in which different atmospheric models can be compared. Many models for the Earth have already been implemented, and the implementation uses quite an advanced unit system. It is however not possible to compare different atmospheres themselves. In order to evaluate the effect of different phase functions and scattering coefficients, this functionality has to be extended.

4.2.1 Refactoring & Extension

The framework is mostly implemented by non-member functions and with almost no classes, which makes it really difficult to change parameters like the phase function for only specific atmospheres. This work improves the framework by refactoring it and allowing the dynamic composition of different atmospheric properties. These properties can now be defined by a new configuration file with the *YAML* syntax. Based on the chosen properties, the concrete functions like e.g., phase functions and scattering approximations that should be used, can be chosen from numerous implemented functions.

All Models inherit from the new `CgAtmosphereModel` class, which gives an interface for all models to use. This enables an easy comparison of different models. The header of the class is shown in the appendix in **Section A.1.1** The non-member functions for Atmospheric properties have been replaced with a unified class for atmospheric properties: `AtmosphericFunctions`. This new class also adds support for atmospheres with a wavelength dependent phase function, like the Martian atmosphere.

In order to support atmospheres with a wavelength dependent phase function, the function `InverseSolidAngle MiePhaseFunction(Number scattering_angle_cosine)` has been replaced with `PhaseFunctionSpectrum MiePhaseFunction(Number scattering_angle_cosine)`. In other words, the new implementation always returns a phase function value for every wavelength, instead of one value for all wavelengths. Though, not all atmosphere need a wavelength dependent phase function, like e.g. the Earth's. In this case, the function simply returns the same phase function value for all wavelengths.

The goal of the new refactored framework is to support not only the Earth's and Martian atmospheres, but a variety of other atmospheric models. Instead of individual implementations for a specific atmosphere, a more dynamic approach has been chosen. By using `std::function`, it is possible to compose an individual atmosphere at runtime, by choosing between various implementations.

So far the list of implemented functions in the new refactored framework contains several phase functions like the *Rayleigh*, *Cornette-Shanks*, *Henyey-Greenstein* and *Double Henyey-Greenstein* phase functions. It is also possible to load a custom phase function values from a `csv` file. For extinction and scattering coefficients, the supported implementations cover *Penndorf's Table of Rayleigh Scattering Coefficients for standard air* [17], the Angstrom coefficient [55], a constant coefficient and an import from a `csv` file. The refactored implementation also adds the possibility to directly compare two models and different atmospheres.

New Concept for the Executable   In contrast to the original implementation which had a single `main` function which compared all implemented models with measured data and was not configurable in any way, the new implementation works with configuration files. An example configuration for the model used by *Costa et al.* can be seen in **Section A.1.2**. This new framework will later be used to compare the previous atmospheric models with the *Blue Moon's* and *hybrid* model. Especially, the functionality to measure radiance and chromaticity values at various positions in the sky will be used to compare the models against real measurements.

Caching of Precomputed Data   Some models require a pre-computation phase before being able to render any images. If the pre-computation phase has to be repeated, depends on a number of parameters. In case of *Bruneton's* model, the pre-computed transmittance data depend on the *extinction* and *scattering* coefficients, the *planet radius* and the *scale heights*. If any of these parameters changes, the pre-computation step has to be repeated. Instead of simple overwriting the calculated data, the new implementation calculates a hash value of all contributing properties and stores the pre-computed data in a folder with the hash as its name. This way, the pre-computation phase for a given set of properties has only to be done once. This makes the comparison of different models in the evaluation phase much faster.

4.3 Real-Time Implementation

The models by *Collienne* and *Costa et al.* are both based on the model developed by *Eric Bruneton et al.* and are capable of rendering the atmosphere in real-time [26]. An example real-time implementation for this model has been published by *Eric Bruneton* [56] himself. In order to have a direct comparison to the models by *Collienne* and *Costa*, in addition to the new martian models, both of these previous models have been implemented in the real-time version, as part of this thesis, as well.

Coefficients   The implementation by Bruneton calculates the wavelength dependent values for scattering and extinction with the formula of *Anders Angstrom* [55]. For the Earths' atmosphere, Bruneton chooses $\alpha = 0.0$ and $\beta = 5.328 \cdot 10^{-3}$.

For the new implementation, the same Rayleigh scattering coefficients as used by *Costa et al.* were chosen. The extinction β_{ext}^M and scattering coefficients β_{sca}^M for Mie scattering are calculated using Mie theory. Unfortunately, *Colliene et al.* don't mention their Mie extinction and scattering parameters, so they have to be guessed. They base their model on the original implementation by *Eric Bruneton et al.* [26] so the same parameters for Mie scattering are assumed.

Phase Functions   The wavelength dependent phase function used by *Costa et al.* is implemented as three calls to the **Double Henyey-Greenstein** phase function. In contrast, the implementation for the model by *Collienne* simply uses a **Cornette-Shanks** phase function with $g = 0.8$. The new implementation of the phase function relies on a lookup from a pre-populated array. In this implementation, the phase function has a resolution of $0.25°$ and is linearly interpolated between

	Colliene	Costa & New
β_{sca}^{R}	$(19.918, 13.57, 5.75) \cdot 10^{-3}$	$(1.2871, 3.056, 7.6406) \cdot 10^{-3}$
β_{sca}^{M}	$(0.432, 0.432, 0.432) \cdot 10^{-3}$	$(15.4969, 12.8212, 10.2982) \cdot 10^{-3}$
β_{ext}^{M}	$(0.48, 0.48, 0.48) \cdot 10^{-3}$	$(16.1938, 15.7726, 15.4174) \cdot 10^{-3}$

Table 4.1: Comparison of the martian coefficients. $\lambda = (440, 550, 680)$.

those values, to suppress visual artifacts. The lookup function, which takes place in the fragment shader, can be seen in **Section A.3**

Texturing the Planet　　In addition to views from the ground, *Costa et al.* [31] compare renderings from space to images taken by the Hubble Space Telescope. To be able to compare these views with images created by the real-time implementation, the surface of Mars has to be textured. The example implementation given by *Bruneton et al.* realizes the planet's body, not as a typical sphere made from vertices. They instead use the parametric formula for a sphere and perform a ray intersection test in the fragment shader to evaluate the position of the fragment on the sphere.

The calculation of the *uv* texturing coordinates is shown in the **Appendix A.3**. At first, the code calculates the position on the sphere corresponding to the fragment, based on the camera's position, the view direction, the distance of the camera to the intersection and the center of the planet. Then, based on this position on the sphere, the latitude and longitude coordinates and finally the *uv* of the projected texture can be calculated. The color value of the texture must then be converted to the ground albedo of the martian planet by converting the value from the *sRGB* color space to linear values.

5 Results and Evaluation

This chapter starts with a quantitative comparison of the previously mentioned models and the new one, using the extended framework of *Eric Bruneton*. Afterwards, various renderings are compared with real images taken on the Martian surface. These include sky dome images, ground perspectives and views from outer space.

5.1 Quantitative Comparison

In this section the models by *Collienne*, *Costa*, the new "*Blue Moons*" model based on the phase function described by *Ehlers et al.*, as well as the new "hybrid" model, are compared. The comparisons comprise the sky radiance, the chromaticity of the Martian sky and the transmittance measured in the direction of the Sun. All measured data are also compared with real world measurements taken by various Martian rovers and landers.
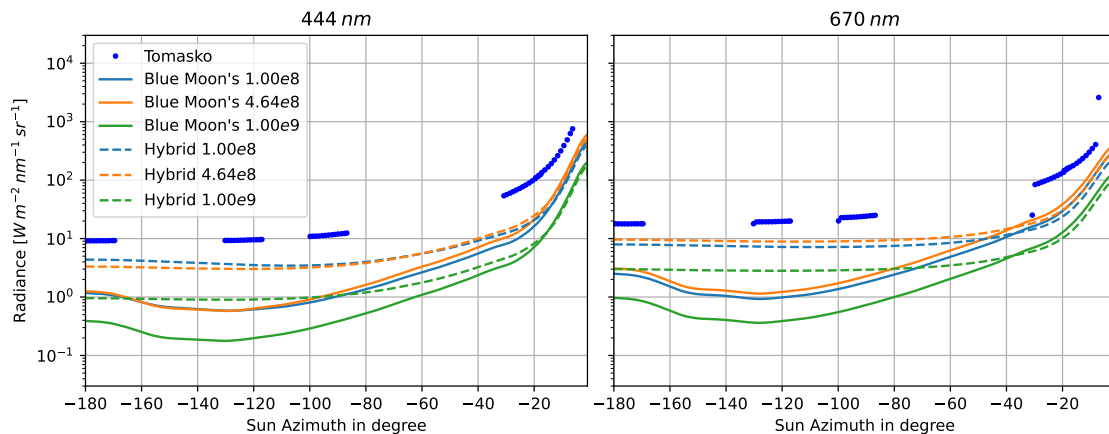
5.1.1 Sky Radiance

Figure 5.1: Sky radiance at a Sun elevation of 14° evaluated at 442.25 nm for 6 different dust densities.

The sky radiance, measured in [$W\,m^{-2}\,nm^{-1}\,sr^{-1}$] shows how much energy finally arrives at the observer's eye. The robotic spacecraft *Mars Pathfinder* landed on Mars in 1997 and its rover Sojourner was the first rover on Mars. The CCD camera of the *Imager for Mars Pathfinder* (IMP) was used to take several sequences of photos of the Martian atmosphere. *Tomasko et al.* [34] analyzed some of these sequences, taken during times when the Sun was low in the sky (between

12° and 29°). Each data set contains either six or 15 images which were taken at 20°, 75°, 120° and 170°, with each frame covering an area 14° wide. The data shown in **Figure 5.1** consists of 28 sequences, taken in the morning and in the evening of the 11th Sol of the *Mars Pathfinder* mission. Each sequence consists of four scans at 444, 671, 896, and 965 nm [34]. The resulting radiance functions for the respective wavelengths show the sky radiance with a Sun azimuth from −180° to 0° and a Sun elevation of about 13° to 15°. The measurements of the models are taken at 14° Sun elevation ranging from a Sun azimuth of −180° to 0°. The resulting sky radiance values can be seen in **Figure 5.1** and **Figure 5.2**. It must be noted that the larger radiance values of the measurements might stem from the height of the landing site of *Mars Pathfinder* above sea level.
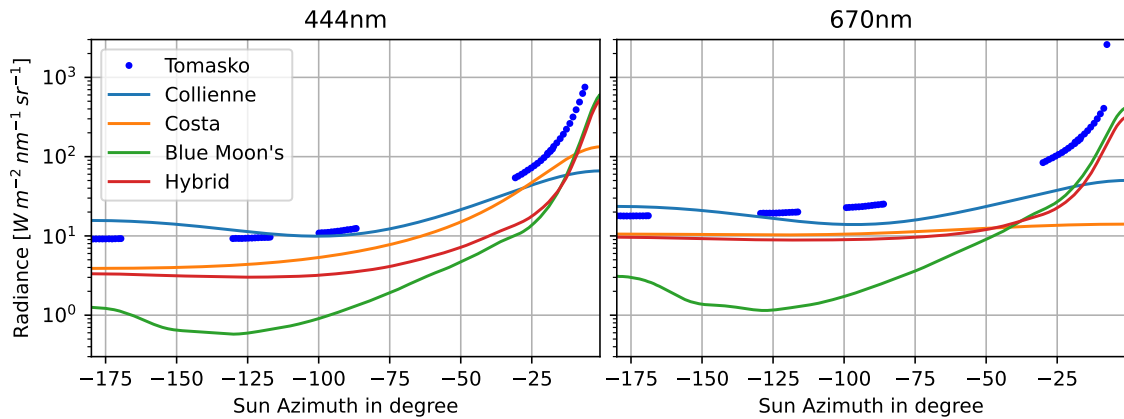

Figure 5.2: Sky radiance at a Sun elevation of 14° evaluated at 442.25 nm compared with results from *Tomasko et al.* and the models by Collienne, Costa and the *Blue Moon's* and *hybrid* model. For the *number density* at sea level $N_0 = 4.64 \cdot 10^8$ was chosen.

One free parameter of the compared models is the *number density* at sea level N_0 ($molecules/cm^3$) which represents the amount of dust in the atmosphere. As shown in **Figure 5.1** different densities result in a brighter or dimmer sky. In the comparison, $N_0 = 4.64 \cdot 10^8$ resulted in the overall brightest sky and which is closest to the real-world measurements by *Tomasko et al.* which is true for both measurements available at 444 nm and 670 nm. The differences in radiance between the *Blue Moon's* and the *hybrid* model are quite obvious. The *Blue Moon's* model has a stronger peak in the forward-scattering regime, but is much darker after about 40°. According to the data by *Tomasko et al.* there should be no peak in the radiance in the backward-scattering area around 180°. The *Blue Moon's* model on the other hand shows a noticeable peak, whereas the *hybrid* model compares much better with the measured data. Overall, both models seem to be too dark at all angles. Contrary to expectations, lowering the amount of dust in the atmosphere does not result in a brighter sky over all angles. For the *hybrid* model, the radiance curve for $N_0 = 1.00 \cdot 10^8$ at 444 nm is greater than that at $N_0 = 4.64 \cdot 10^8$ at large azimuth angles, but smaller for smaller angles. At 670 nm, fewer dust particles in the atmosphere result in a dimmer overall sky appearance. A greater number density of $N_0 = 1.00 \cdot 10^9$ also leads to a dimmer overall sky. Almost the same behavior can be observed for the *Blue Moon's* model.

This behavior can be explained by the low density of the Martian atmosphere. Alongside dust particles, gases like CO_2 scatter only a fraction of the energy compared to Earth. If there is not

much dust in the Martian atmosphere, there simply aren't many molecules that scatter light into the observer's eye. On the other hand, if the dust content in the atmosphere is very large, more light is scattered away from the planet or even absorbed by the particles.

The resulting sky radiance produced by the models varies a lot. In **Figure 5.2** results for the four models are shown for $N_0 = 4.64 \cdot 10^8$. The brightest model by *Collienne* totally lacks the strong forward peak near the Sun. *Costa et al.* achieve a stronger peak, but are a bit darker after about 30°. The *Blue Moon's* phase function has a much stronger forward scattering peak which comes much closer to the measured data, both for 444 nm and 670 nm. Unfortunately, it is way too dark in the back- and side-scattering area. The *hybrid* model combines the strong forward scattering peak of the *Blue Moon's* model with the better fitting model by *Costa et al.* for the back- and side-scattering area.
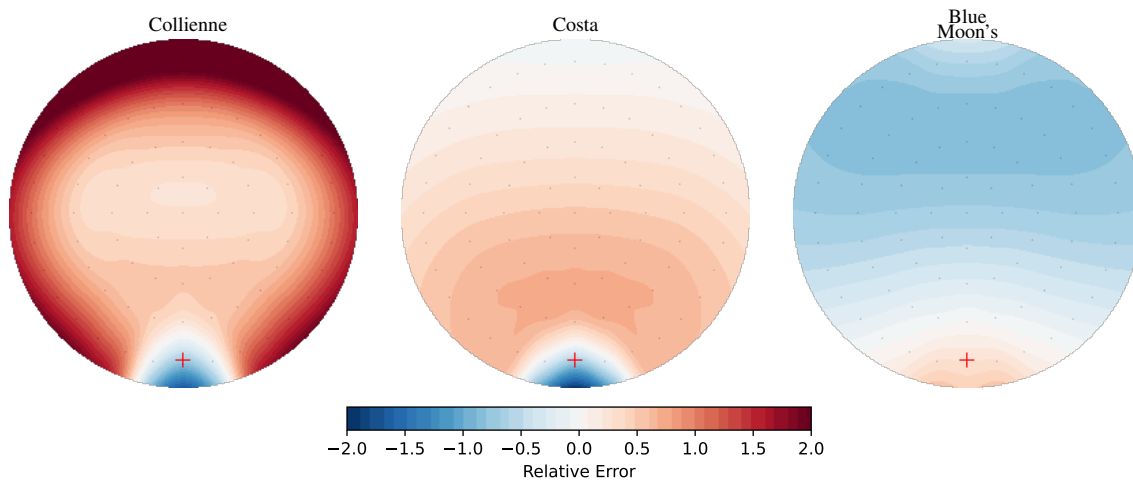

Figure 5.3: Relative radiance error between the *hybrid model* and *Collienne*, *Costa* and the *Blue Moon's* model at 14° Sun elevation.

Relative Radiance Between the Models   One of the features of the framework developed by Eric Bruneton is the calculation of the relative error of the radiance between two models. This error is calculated at 81 different sample points. Then, by using a spherical bicubic interpolation, the whole sky dome can be rendered as an image. The results are shown in **Figure 5.3**. The models by *Collienne*, *Costa et al.* and the *Blue Moon's* model are compared against the model with the *hybrid* phase function which overall matches the measured radiance by *Tomasko et al.* the most. The error is calculated by $error = (r_1 - r_2)/r_2$ with r_1 being the respective radiance of on the three models and r_2 being the radiance of the *hybrid* model.

Especially when the Sun is low in the sky, the model by *Collienne* is much brighter at greater azimuthal angles compared to the *hybrid* model. On the other hand, closer to the Sun it is much darker, which considering that **Figure 5.2** shows that the *hybrid* model is too dark as well, makes clear that the model cannot show the Martian sunrise and sunsets very accurately.

The model by *Costa et al.* is overall much closer to the *hybrid* model. In the back-scatter region, there is basically no difference. This is expected, as the phase function of the *hybrid* model converges

to the phase function by *Costa et al.*. In the forward scattering area, the model is much darker. As seen in **Figure 5.2** the lobe around the Sun is much broader than the measurements show.

As already seen in the comparison with the measurements, the overall brightness of the *Blue Moon's* model is too low. The bright area around the Sun can be explained by the fact, that the *hybrid* phase function has been normalized after mixing it with the phase function by *Costa et al.* This leads to a darker phase function in the forward scattering area around 0° compared to the *Blue Moon's* model. After all, the area under the curve is the same for all phase functions. In comparison, the *Blue Moon's model* also shows a back-scattering peak.

Figure 5.4 shows the relative luminance sampled at 81 different points, interpolated across the whole sky dome. Luminance describes how a human eye would perceive the brightness of the sky over all wavelengths, and it is calculated relative to the luminance measured of the zenith direction. The model by *Collienne* shows no significant luminance peak around the Sun, which does not match the measurements by *Tomasko et al.* [34]. On the other hand, there is also no back scattering peak visible, which is expected.

The model by *Costa et al.* shows a large lobe around the Sun with no significant backward scattering peak. There is generally no large luminance difference between the darkest and the brightest parts of the image.

The *Blue Moons* model shows a very strong forward scattering peak and a smaller backward scattering peak. The peak follows the Sun during the day. The darkest part of the sky is quite a bit darker than the bright spot around the Sun. The luminance profile of the *hybrid* model shows the expected mix between the model by *Costa* and the *Blue Moon's* model. There is a strong forward scattering peak, but no backward scattering peak. The luminance does not vary very much across the whole sky dome.

According to the measurements by *Tomasko et al.* the luminance profile of the martian sky should have a strong forward scattering peak which is only produced by the *Blue Moon's* and *hybrid* model. On the other hand, there should be no backward scattering peak which is matched by the models by *Collienne*, *Costa et al.* and the *hybrid* model. The *Blue Moon's* model shows a significant backward scattering peak. In the side scattering regime, the *Blue Moon's* model is by far the darkest of all the models and the worst match for the measured data. Overall, the *hybrid* model seems to match the expected luminance profile the closest.
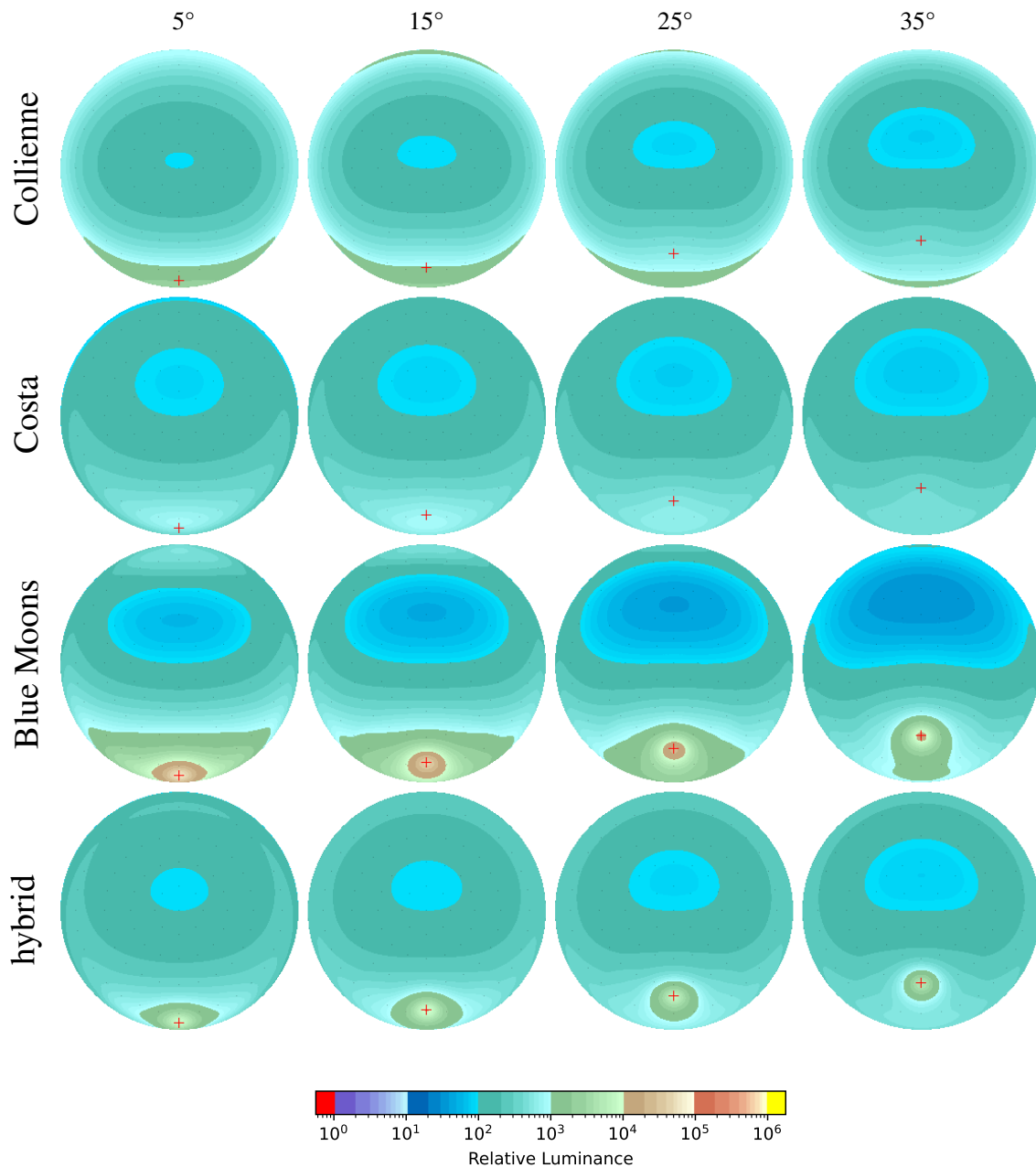
Figure 5.4: Relative luminance compared to the zenith luminance (90° Sun elevation) for different Sun elevation angles for all four models.

5.1.2 Chromaticity Comparison

Next, the chromaticity of the models is compared to measurements. The *Mars Exploration Rover's* (MER) *Spirit* and *Opportunity* took chromaticity measurements as part of a sky- and horizon survey during their first year on Mars [57]. The data was acquired by the panoramic cameras on top of the

rovers. These cameras had been calibrated when they were fitted to the rovers. With this calibration data, it is possible to convert the images to actual physical units.
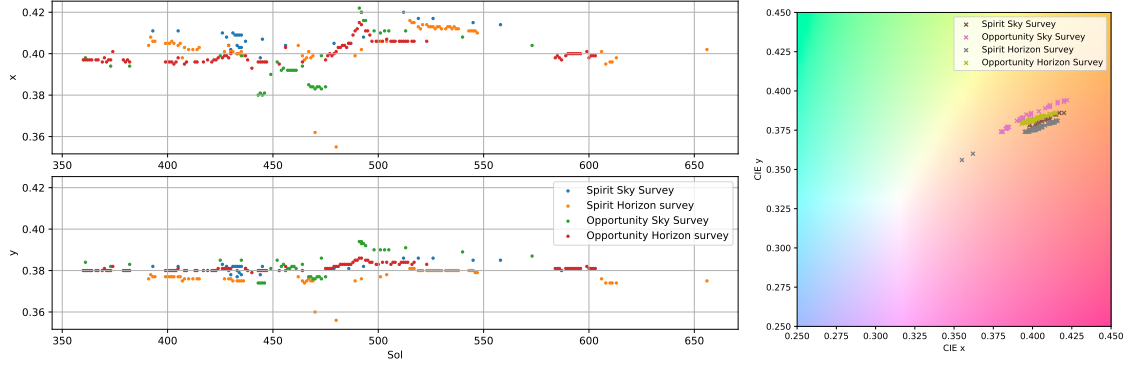

Figure 5.5: Chromaticity measured by Spirit and Opportunity [57].

The horizon survey had the camera pointed 3° above the horizon directly to the west. Images were taken when the Sun is high in the sky, typically between 11am and 12am. Each observation acquired one full frame image with each of the L4, L5 and L6 filter wheels (482, 535 and 601 nm). From each combined image, the average x and y CIE chromaticity values from a selection of certain pixels, result in the final chromaticity for the observation, which can be seen in **Figure 5.5**. The graph on the left shows the x and y values over time. On the right side, all measured data are shown in a CIE scatter plot. The sky survey on the other hand takes images of multiple portions of the sky. The time of day at which these images were taken changed frequently. It is notable that the x and y values of the sky and horizon survey differ by less than 7% [57].
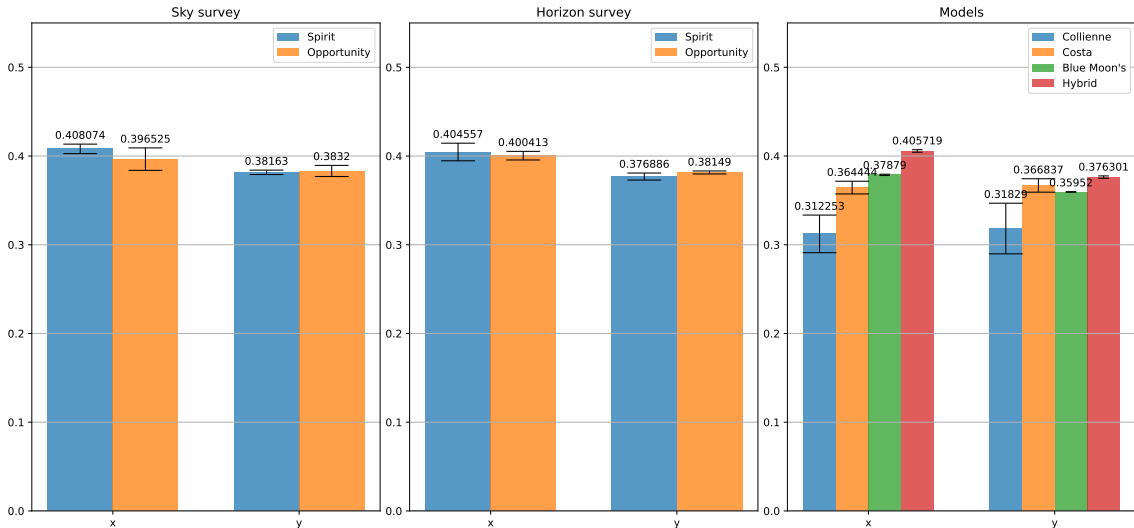

Figure 5.6: Measured chromaticities of the two MER rovers Spirit and Opportunity, with their mean value and the standard deviation compared to the four sky models. For the *number density* at sea level $N_0 = 4.64 \cdot 10^8$ was chosen.

The mean chromaticity values and their standard deviation are shown in **Figure 5.6**. Spirit's horizon survey shows the greatest standard deviation, followed by the sky survey of Opportunity, although the deviations are generally not really large.

The chromaticity values of all the models were evaluated at all Sun elevation angles from 0° to 90°. The model by *Collienne* produces the largest difference to the measured data. The average *x* value of 0.313 is much lower than the measured data with averages of 0.408, 0.396, 0.405 and 0.400. The average *y* value of 0.318 is also much lower than the averages of 0.382, 0.383, 0.377 and 0.381. The chromaticity of the model by *Costa et al.* and the *Blue Moon's* and *hybrid* models are much closer to the measurements, with the best fitting one being the *hybrid* model.

Figure 5.7 shows the chromaticity for a given Sun elevation angle. The graph shows, that for low Sun angles the *x* and *y* values depend strongly on the Sun elevation. Especially, the model by *Collienne* varies a lot for different Sun elevations. Like seen in the CIE graph, for low Sun angles the color of the sky opposite to the Sun can have a blue tint, that converges only to an orange tone when the Sun is at least 10° above the horizon. The model by *Costa et al.* also varies a lot over different Sun elevation angles. The range is about as large as the color change of the *Spirit sky survey*, although it is too far in the blue direction. The *Blue Moon's* chromaticity is basically independent of the Sun elevation angle, but like the model by *Costa et al.* the color is a bit off. The *hybrid* model achieves the best results. The chromaticity range is right in the region of the measurements for a number density of $N_0 = 4.64 \cdot 10^8$.
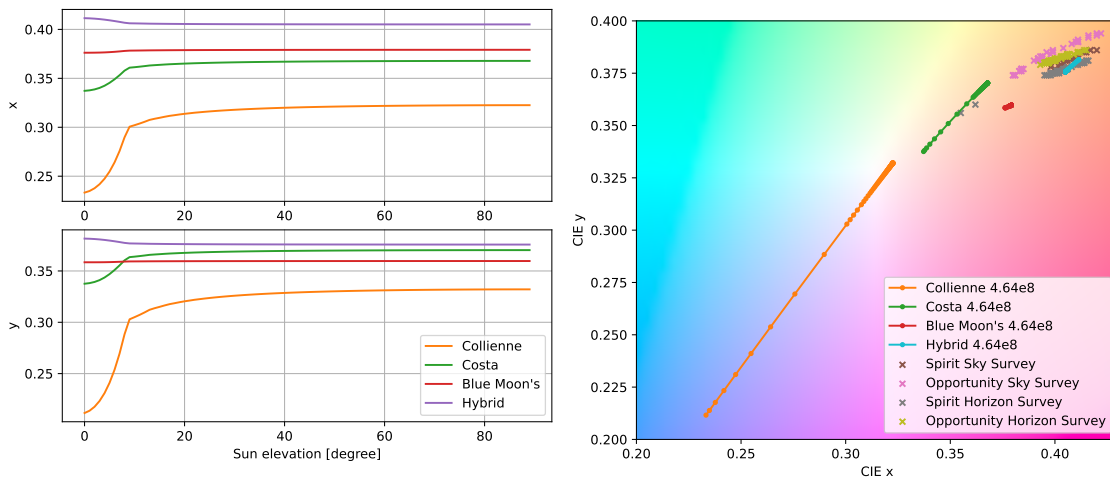

Figure 5.7: Chromaticity for a simulated Martian atmosphere looking 180 degree away from the Sun azimuth and for Sun elevations from 0° to 90°.

Figure 5.7 shows the chromaticity of all four models for different Sun elevation angles. At 5° *Collienne* shows a blue color all around the horizon. The blue color during low Sun angles is not a feature around the Sun, but to large atmospheric paths. As *Ehlers* pointed out, the blue tint is a feature that could be visible during the whole day, but it is not produced by*Collienne's* model. The

blue glow around the Sun by *Costa et al.* is the largest one of the models. Its color is also extremely blue, but the orange color of the sky is a bit more orange and more uniform than the previous model by *Collienne*. Like seen in the comparison with the measured chromaticity data, the *Blue Moon's* and *hybrid* model come closest to the actual data. The whole sky shows a distinctive orange color, which is most predominant for the *hybrid* model. Both, the *Blue Moon's* and *hybrid* model, show a blue tint around Sun the at all angles.
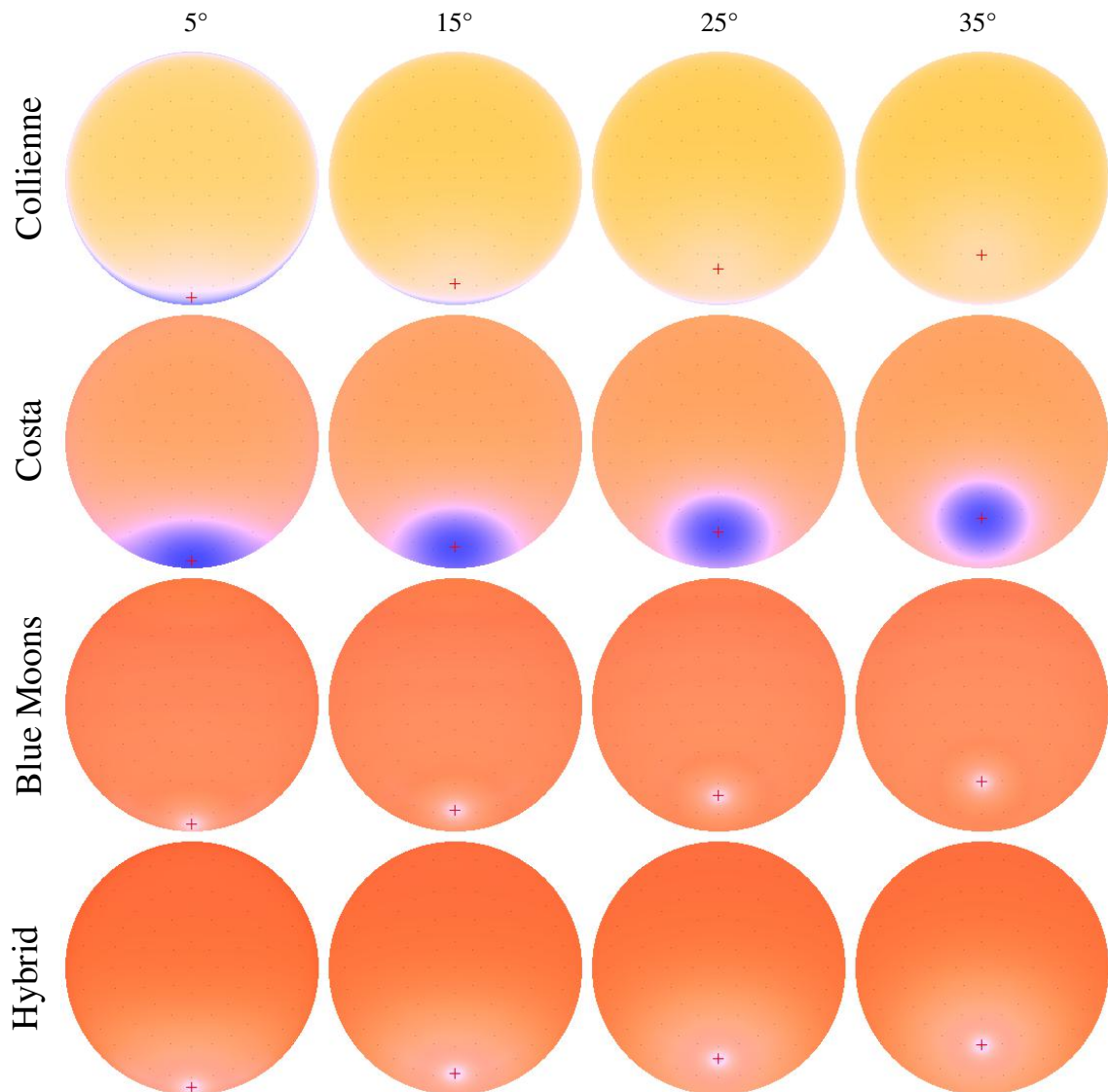
Figure 5.8: Chromaticity comparison for all models at four different Sun elevation angles. For the *Blue Moon's* and *hybrid* model, a number density of $N_0 = 4.64 \cdot 10^8$ was chosen.

Just as the sky radiance, the chromaticity is also dependent on the amount of dust in the atmosphere. **Figure 5.9** shows the dependency between the dust density and the observed sky chromaticity for the *Blue Moon's* and the *hybrid* model. The graph shows, that in order to achieve a red color, quite

a dense dust atmosphere is needed. Like mentioned previously, the reddish color comes from the dust in the Martian atmosphere. If only the gases like e.g. CO_2 were considered, the atmosphere would have a blue tint which explains, why for low dust densities the sky has a blue rather than a red tint.
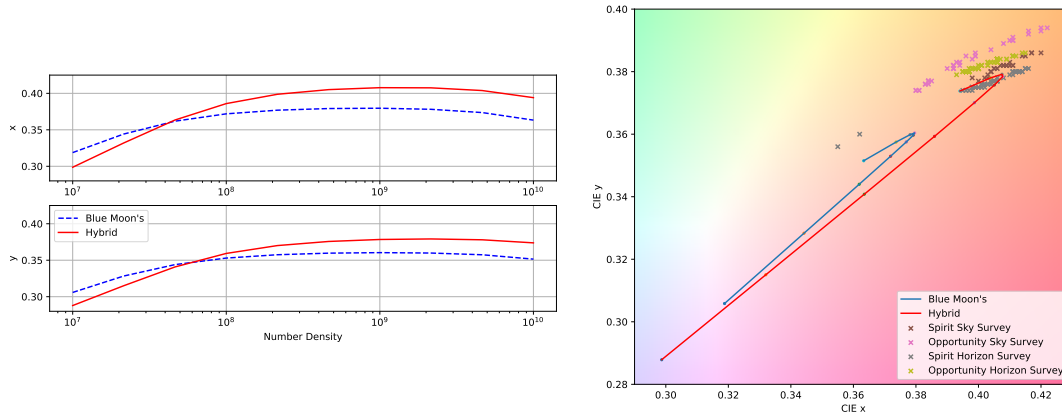

Figure 5.9: Chromaticity comparison of different dust densities for the *hybrid* model.

5.1.3 Transmittance Comparison

As mentioned in **Section 2.1.4** the transmittance expresses the ratio of photons that can travel the distance *s* without being absorbed or scattered away. During their lifetime on Mars, *Spirit* and *Opportunity* took extensive transmittance measurements by measuring the sunlight reaching the rovers [58]. Measurements of the two rovers are available for a combined total of 7315 Martian days, or sols. The measured transmittance data are shown in **Figure 5.10**.
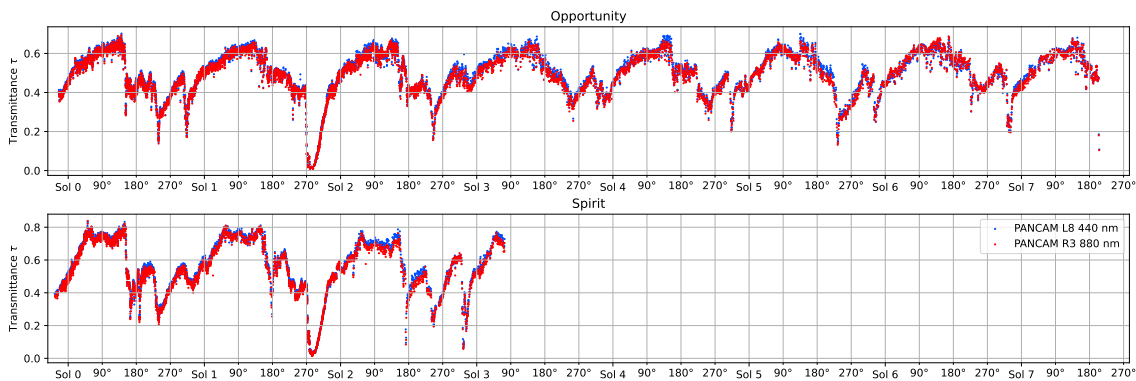
Figure 5.10: Atmospheric transmittance measured by the two MER rovers Spirit and Opportunity. The x-axis shows the Martian year (Sol) of the mission. The minor ticks show the solar longitude, which describes the position on the martian orbit around the Sun.

Mark T. Lemmon [58] analyzed the seasonal behavior of the amount of dust in the atmosphere. Seasons on Mars are often described by their solar longitude, which describes the position of Mars

on the orbit around the sun. For both rovers, they came to the conclusion, that early in the Martian year from $0 - 135°$ the dust content of the atmosphere is generally quite low. The $135 - 215°$ season shows local to regional storms, which most of the time is also true for the $215 - 360°$ season, but this is also the time in which global dust storms occur. The measured transmittance values vary from $\tau = 0.00988$ measured by Opportunity on Sol 3363, to $\tau = 0.839$ measured by Spirit on Sol 428, both with the 880 nm filter.

In order to compare the transmittance values generated by the models with the measured data, a variety of sample points have to be considered. The transmittance values for Sun elevation angles from $0°$ to $90°$ for different dust densities are shown in **Figure 5.11**. The results can be explained quite intuitively. The transmittance is influenced by the amount of dust in the atmosphere and by the length of the path s through the atmosphere, which in turn is dependent on the elevation of the Sun. When the Sun is low in the sky, the path is much longer than during times of high Sun elevations. Just as the best fitting chromaticity values were observed for $N_0 = 4.64 \cdot 10^8$, the density that matches the measured transmittance values the most seem to be $N_0 = 4.64 \cdot 10^8$ as well. The histogram on the left in **Figure 5.11** shows the combined transmittance data of both rovers at $440 nm$.
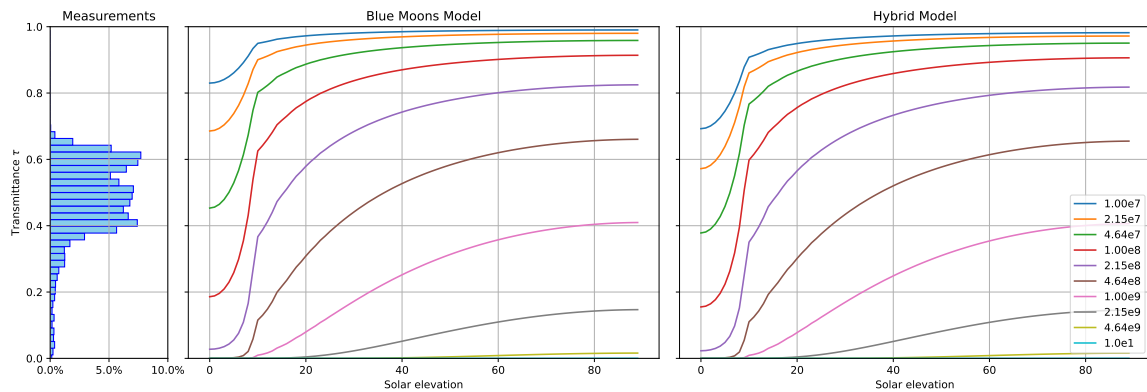

Figure 5.11: Transmittance density comparison for the *hybrid* and *Blue Moon's* model at 444 nm.

5.2 Qualitative Comparison

Figure 5.12: NASA's Mars Exploration Rover Spirit captured this view as the Sun sank below the rim of Gusev crater on Mars (left) [1]. The image on the right shows the same viewpoint but rendered with the *hybrid* model with a dust density of $N_0 = 4.64 \cdot 10^8$ and a Sun elevation of 1°. The silhouette of the rocks in the foreground is overlaid from the original image.

Figure 5.12 shows an image taken by the Mars Exploration Rover Spirit on its 489th Martian day. The color corrected image shows the distinct blue glow above the Martian sunset and the otherwise orange- or yellowish Martian sky. The right image shows a rendering of the *hybrid* model. The overall appearance of the two images seems to be really close. The glow around the Sun has an almost equal shape, which may only be a bit larger in the original photograph. The glow in the original image has a more bluish color and also seems to reach a bit higher through the atmosphere.

5.2.1 Comparing Rendered Sunset Sequences

The left column of **Figure 5.13** shows actual images taken by the InSight Mars lander during the sunset of Sol 1198 in 2022. The images are not color corrected and do not match what a human eye would see, but they provide a sequence of images of a real views of a Martian sunset. Next to this are sequences showing rendered images of each of the four compared images, showing approximately the same Sun elevation at the same viewpoint. The Sun elevation angles cover 2° to −2° with a 1° step. The exposure is the same for all images. Compared to the real images, the rendered images by *Collienne* show the previously observed blue color above the horizon, which does not seem to be a feature of light scattering around the Sun but generally to the horizon. This matches with the theoretical knowledge about the model, which achieves the blue tint of the sunset through adapted Rayleigh scattering coefficients. This unfortunately also leads to a completely blue horizon.

The rendered images of the model by *Costa et al.* show a blue glow which is more concentrated around the Sun than by *Collienne's* model. On the other hand, its color is also much bluer, which does not match what could be expected from the images from *Mars InSight*. All of those images show the distinctive look of a dusty atmosphere. During the sunrise and sunset, there is a characteristic glow

above the Sun, which can already be seen when the Sun is still below the horizon. Depending on the dust density, the shape of the glow forms a narrower or wider v-shape. The model by *Costa et al.* does not produce this feature at all. The *Blue Moon's* model with the phase function developed by *Ehlers et al.* has a much more concentrated glow around the Sun, which is also much brighter than the previous models, which seems to match the look of the real images much better. On the other hand, the glow is almost too bright, as the Sun itself can hardly be seen anymore. Of all models, the hybrid model comes closest to the look of the real images. The Sun disc itself can still be seen, and the glow around the Sun matches that of the images the most. It has to be noted that in order to render an image, factors like the white balance, gamma correction and tone mapping are the same for all models but don't necessarily match the properties of the robotic arm-mounted, Instrument Deployment Camera (IDC) on *Mars InSight*.
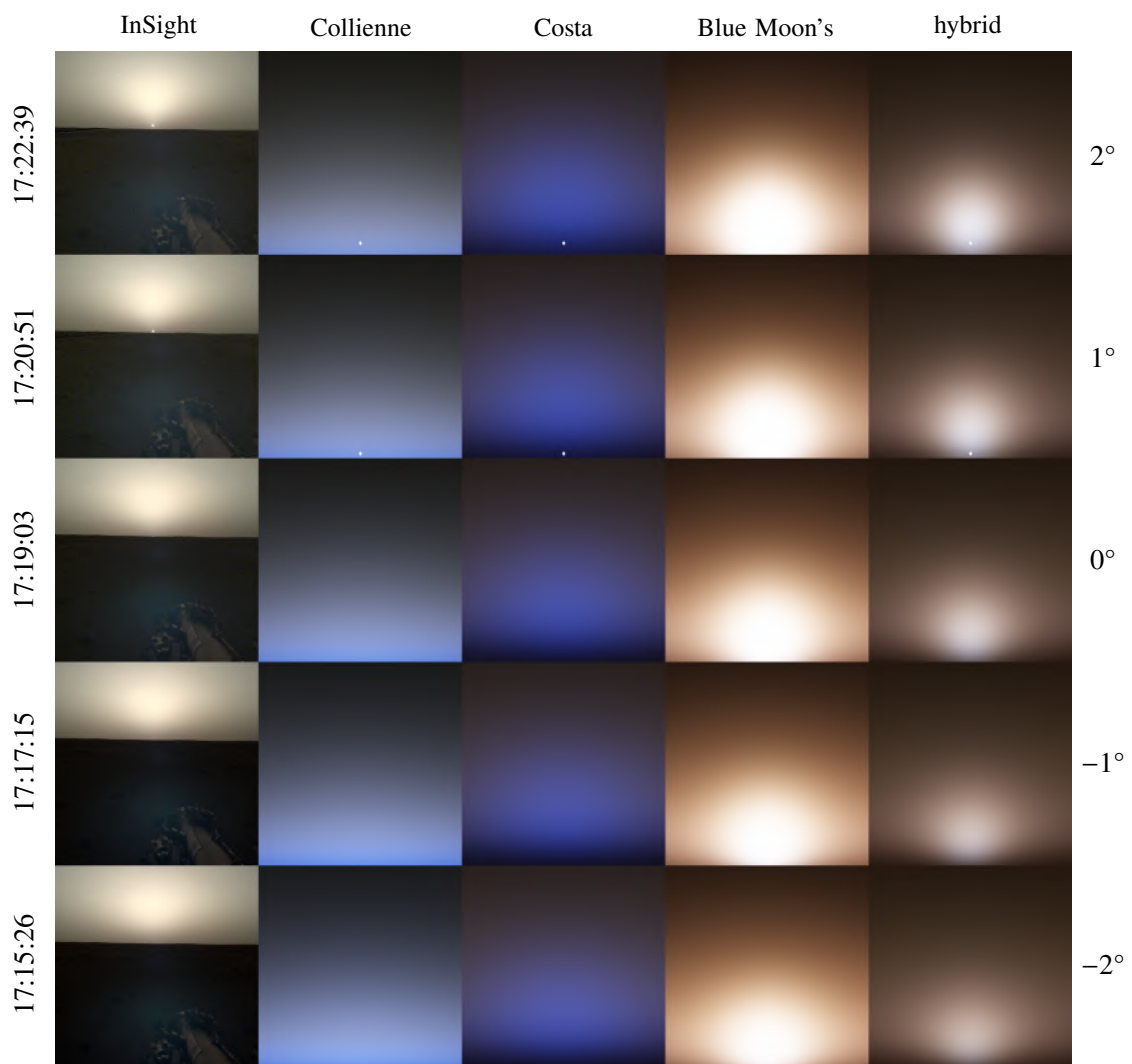

Figure 5.13: Comparing a sequence of images taken by the lander InSight with renderings from all models [59]. More images and renderings can be seen in the **Appendix A.4**
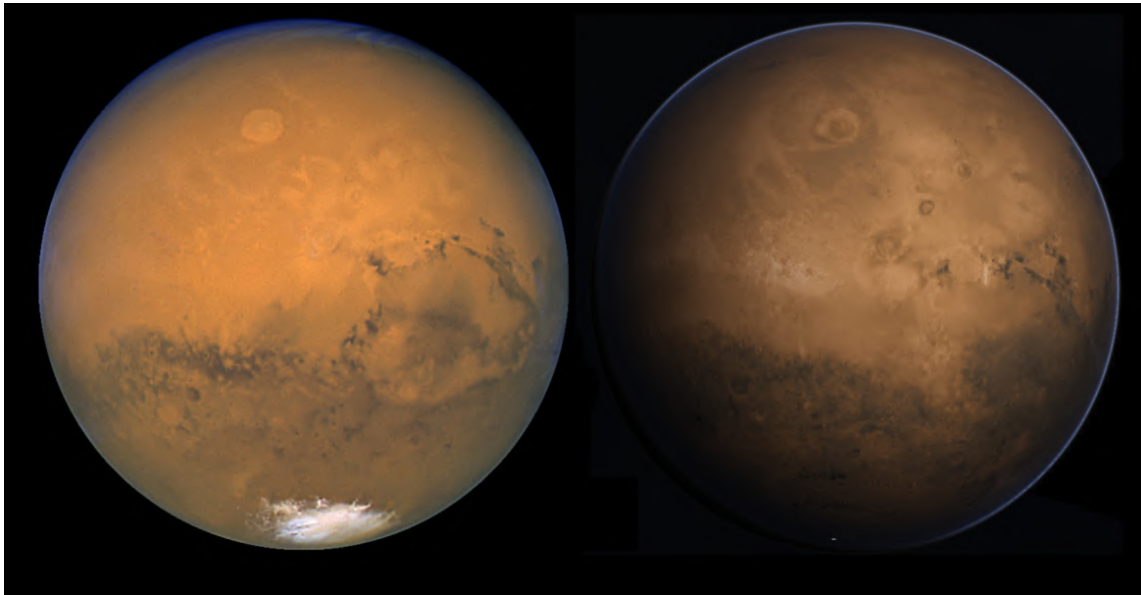
5.2.2 Views from Space

Figure 5.14: Photo taken by the Hubble telescope (left) [29] and the atmosphere rendered with the model by *Costa et al.* (right) as shown in their paper [31].

In contrast to the framework by Bruneton, the real-time implementation is not limited to a fixed viewpoint on the ground and even allows for viewpoints from space. In their paper, *Costa et al.* [31] compare their model with an actual image of Mars taken by the Hubble telescope (**Figure 5.14**). Their implementation is part of the *OpenSpace* project, which has a detailed Martian model which also contains terrain data. This is not only important for viewpoints close to the surface but also renderings from space, as the density of the atmosphere and its vertical height play a huge factor in its appearance. In fact, a large part of the Martian surface is very high above average, which results in a large variety of the atmospheric thicknesses.

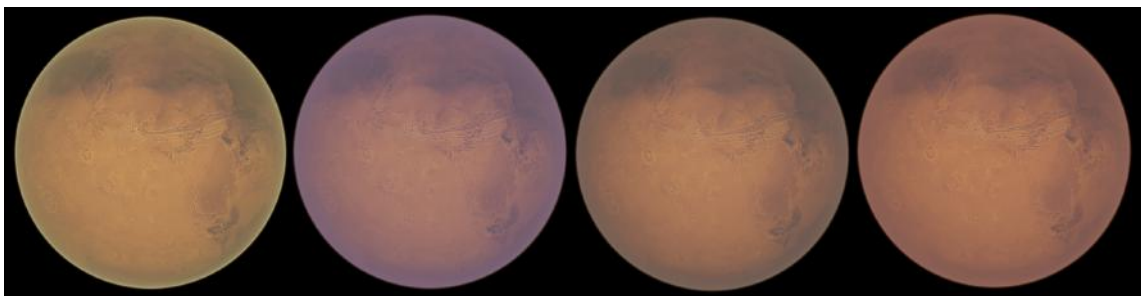Figure 5.15: Rendered images from with viewpoint from space. From left to right: *Collienne*, *Costa*, *Blue Moon's* and the *hybrid* model

The real-time implementation is based on an example implementation developed by *Eric Bruneton*

which assumed the planet to be a perfect sphere, which is probably responsible for the large visual difference compared to the rendered views from all models in **Figure 5.15**.

6 Conclusion and Future Work

Martian atmospheric models like the one by *Collienne* and *Costa et al.* were not really able to render the optical phenomena like the blue sunset which can be seen in the martian atmosphere very accurately. Previous work has shown, that the effects in the martian atmosphere are produced by the wavelength dependent scattering properties of the martian dust. These properties themselves have not been fully characterized yet, although there are many studies trying to deduce them from observations by various martian rovers, landers, and orbiters. One key scattering characteristic is the phase function, which controls how much of the incident light is scattered in which direction. The blue glow around the martian sunrise and sunset is produced by a different phase function for blue light than for the rest of the visible spectrum. Blue light is simply scattered stronger in the forward direction than the other colors. This mechanism is not needed to produce the look of the Earth's atmosphere, and so computer graphic models which render the Earth's atmosphere simply use a single phase function for the whole spectrum.

Eric Bruneton suggests that "... adding more aerosol parameters in the CG models is the best way to significantly increase..."[2] the accuracy. "In particular, we think using more realistic phase functions for aerosols is the easiest way to increase accuracy in the solar aureole region [2]." He also concludes that, the fewer approximations are used, the more realistic are the results.

One of the first models that tried to render the martian atmosphere is the one by *Collienne* [48]. This model does not use an accurate representation for the radiometric energy transport by dust in the atmospheric. Instead, they tweaked the Rayleigh scattering parameters until the result looked most like the martian atmosphere. Following this, these parameters have no physical explanation anymore.

Another model by *Costa et al.* [31] correctly differentiates between scattering by gases like CO_2 and scattering by dust particles in the atmosphere. Their model supports a wavelength dependent phase function, which is implemented as the *Double Henyey-Greenstein* (DHG) phase function. Unfortunately, their final parameters for the DHG have no physical representation as well. In their paper, they wrote that the parameters for the phase function have "different values for different λ by experimental findings [31]." Comparing the phase functions against measurements from martian dust analogues shows that they don't produce the expected strong forward scattering peak. According to *Dabrowska et al.* [35] a typical phase function for irregular mineral dust is a smooth function with a steep forward scattering peak and almost no special features at side and back scattering.

Ehlers et al. [9] proposed that the martian wavelength dependent phase function may be influenced by the iron oxide hematite, They developed a simplified model of the Martian dust with a wavelength dependent refractive index containing hematite. In the forward scattering regime, this resulting phase function comes much closer to measured data from the martian atmosphere than the previous models. Unfortunately, the resulting model based on the *Blue Moons* phase function is too dark in the back and side scattering.

The extended atmospheric model uses the phase function developed by *Ehlers et al.* This phase function has been computed for all 48 wavelengths, which is required by the comparison framework. The phase function was calculated with the Python library *miepython* [54] and then exported as a *csv* file. Another new approach tries to mitigate the fact, that the phase function proposed by *Ehlers et al.*, calculated with Mie theory, only delivers better results in the forward scattering regime. Following this, a *hybrid* phase function was constructed, which is realized as a simple linear interpolation between the *Double Henyey-Greenstein* phase function proposed by *Costa et al.* and the phase function by *Ehlers et al.* To summarize: the models which were compared as part of this thesis are the model by *Collienne*, *Costa et al.*, and the new *Blue Moon's* and *hybrid* models.

In order to be able to compare the previous and the new atmospheric models, the comparison framework originally developed by *Eric Bruneton* [2] was extended to support the comparison of different atmospheric parameters and approximations. Additionally, a whole new concept for the executable of the framework was developed. The original implementation was not configurable in any way. Now, different atmospheres can be composed at runtime based on a new configuration file. Numerous approximations and also a *csv* import have been implemented. Models can be analyzed by their radiance, chromaticity, and transmittance. These measurements can be done along specific zenith and azimuth angles or across the whole sky dome. Just like in the original implementation, it is still possible to generate color and sky dome images.

The comparison shows, that the model by *Collienne* has the brightest overall sky radiance, Unfortunately it is not able to reproduce the strong forward scattering peak close to the sun. The overall radiance along the horizon is also much too large compared to the rest of the curve. Compared to chromaticity measurements by the *Mars Exploration Rovers* Spirit and Opportunity, the color of the sky during daytime shows the largest difference of all models. The blue glow around the sun does also not match the expected shape and intensity.

The model by *Costa et al.* comes much closer to the measured data. The radiance shows a stronger peak close to the sun and no backward scattering peak, which is expected from the measurements. The chromaticity of the model also comes much closer to the measurements.

The strongest radiance peak close to the sun is produced by the new *Blue Moon's* model, although the *hybrid* model comes really close. Both models show a similar sky color to the measurements, but of all compared models, the *hybrid* model comes closest. The blue glow around the sun is much fainter compared to the model by *Costa et al.* but it is still present, although compared to real images it might be almost too faint. Renderings comparing the look of the different models show, that the *hybrid* model is almost confusingly similar to real images, especially during low sun angles.

Of all the evaluated models, none reached the measured radiance by *Mars Pathfinder* as all models are too dark for all directions, although this might be caused by the altitude of the landing site.

Future Work Amongst many martian dust analogues, the real measured phase function for martian dust for multiple wavelengths has not been defined. The representation of the martian atmosphere would be much more accurate with an accurate phase function. Missions like the *Mars sample return* could enable the analysis of martian dust, just like *Dabrowska et al.* did for the different Mars analogue samples [35]. Functions like the Henyey-Greenstein, Double Henyey-Greenstein or Cornette-Shanks phase function which seem fitting for the Earth's atmosphere could be expanded

by an analytical function which fits the martian atmosphere. Also, Martian weather has a strong influence on the look of the atmosphere. The models which are discussed here are all clear sky models, which means that they can only calculate a uniform atmosphere which has no clouds. Martian atmospheric phenomena like dust storm and dust devils cannot be rendered by these models. Additionally, the density of the atmosphere has been assumed to follow an exponential curve, which might not necessarily be true for the dust distribution.

A Appendix

A.1 Bruneton's Comparison Framework

A.1.1 New Classes

```
1  class CgAtmosphereModel {
2  public:
3          ...
4          void init() = 0;
5
6          virtual int GetOriginalNumberOfWavelengths()
7          virtual IrradianceSpectrum GetSunIrradiance(Length altitude, Angle sun_zenith)
           ↪    const = 0;
8          virtual RadianceSpectrum GetSkyRadiance(Length altitude, Angle sun_zenith, Angle
           ↪    view_zenith, Angle view_sun_azimuth) const = 0;
9
10         virtual RadianceSpectrum GetSkyRadiance(Length altitude, Angle sun_zenith, Angle
           ↪    sun_azimuth, Angle view_zenith, Angle view_azimuth);
11
12         virtual IrradianceSpectrum GetSkyIrradiance(Length altitude, Angle sun_zenith);
13         ...
14 }
```

```
1  class AtmosphericFunctions {
2  public:
3  ...
4      std::function<PhaseFunctionSpectrum(Number scattering_angle_cosine)> MiePhaseFunction;
5      std::function<ScatteringSpectrum()> MieExtinction;
6      std::function<ScatteringSpectrum()> MieScattering;
7
8      std::function<PhaseFunctionSpectrum(Number scattering_angle_cosine)>
       ↪    RayleighPhaseFunction;
9      std::function<ScatteringSpectrum()> RayleighScattering;
10 };
```

A.1.2 Atmospheric Properties Configuration Files

Costa

```
1  name: costa
2  output_directory: output/images
3  image_type: SkyImage #LuminanceAndImage
4  sun_strength: 0.43 # 586.2 (w/m^2) / 1361.0(w/m^2)
5  sun_zenith: 71.0
6  sun_azimuth: 00.0
7  white_balance: false
```

```
8   brightness: 5.0 #auto #auto|[1...inf]
9   show_imprint: false
10  width: 200 #0
11  height: 100 #0
12  #model: Bruneton SINGLE_SCATTERING_ONLY 15 #SINGLE_SCATTERING_ONLY,
    ↪ DOUBLE_SCATTERING_ONLY, ALL_ORDERS
13  model: Bruneton ALL_ORDERS 15 # [Meyran,Bruneton,default: Nishita93]
14
15  MiePhaseFunction: DHG (0.67,0.4,0.03) (0.094,0.094,0.094) (0.743,0.743,0.743)
16
17  MieExtinction: Csv input/MiePythonAtmosphere/mars/MieExtinctionSpectrum.csv cext 4e8
18  MieScattering: Csv input/MiePythonAtmosphere/mars/MieExtinctionSpectrum.csv csca 4e8
19
20  RayleighPhaseFunction: Rayleigh
21  RayleighScattering: Constant 1.2871e-6 3.056e-6 7.6406e-6
22
23  PlanetRadius: 3390.0 #in km
24  AtmosphereRadius: 3510.0 #in km
25  RayleighScaleHeight: 8.0 #in km
26  MieScaleHeight: 10.0 #in km
```

Collienne

```
1   name: Collienne
2   output_directory: output/images
3   image_type: SkyImage #SkyImage #LuminanceAndImage #[SkyImage,LuminanceAndImage]
4   sun_strength: 0.43 # 586.2 (w/m^2) / 1361.0(w/m^2)
5   sun_zenith: 71.0
6   sun_azimuth: 00.0
7   white_balance: false
8   brightness: 5.0 #auto #auto|[1...inf]
9   show_imprint: false
10  width: 200 #0
11  height: 100 #0
12  #model: Bruneton SINGLE_SCATTERING_ONLY 15 #SINGLE_SCATTERING_ONLY,
    ↪ DOUBLE_SCATTERING_ONLY, ALL_ORDERS
13  model: Bruneton ALL_ORDERS 15 # [Meyran,Bruneton,default: Nishita93]
14
15  MiePhaseFunction: CornetteShanks 0.5 #CsvPhaseFunction
    ↪ input/MiePythonAtmosphere/mars/MiePhaseFunctionSpectrum.csv #DHG (0.67,0.4,0.03)
    ↪ (0.099,0.89,0.094) (0.01,0.04,0.743) #
16
17  MieExtinction: Angstrom 0.0 5.328e-3 1.0 # AngstromAlpha AngstromBeta
18  MieScattering: Angstrom 0.0 5.328e-3 1.0 # AngstromAlpha AngstromBeta
19
20  RayleighPhaseFunction: Rayleigh
21  RayleighScattering: Constant 5.75e-6 13.57e-6 19.918e-6 #3.0560e-3 #Penndorf #Constant 0.0
    ↪ #[Penndorf,None,Csv input/MiePythonAtmosphere/mars/MieExtinctionSpectrum.csv csca
    ↪ 2.68731e19]
22
23  PlanetRadius: 3390.0 #in km
24  AtmosphereRadius: 3510.0 #in km
25  RayleighScaleHeight: 8.0 #in km
26  MieScaleHeight: 10.0 #in km
```

Blue Moon's

```
1   name: Blue Moons
2   output_directory: output/images
3   image_type: SkyImage #LuminanceAndImage #SkyImage #LuminanceAndImage #RadianceLuminance
4   sun_strength: 0.43 # 586.2 (w/m^2) / 1361.0(w/m^2)
5   sun_zenith: 88.0
6   sun_azimuth: 00.0
7   white_balance: false
8   brightness: 5 #auto #auto|[1...inf]
9   brightnessFactor: 0.5
10  show_imprint: false
11  width: 100 #0
12  height: 100 #0
13  #model: Bruneton SINGLE_SCATTERING_ONLY 15 #SINGLE_SCATTERING_ONLY,
    ↪   DOUBLE_SCATTERING_ONLY, ALL_ORDERS
14  model: Bruneton ALL_ORDERS 15 # [Meyran,Bruneton,default: Nishita93]
15
16  MiePhaseFunction: CsvPhaseFunction
    ↪   input/MiePythonAtmosphere/mars/MiePhaseFunctionSpectrum.csv
17
18  MieExtinction: Csv input/MiePythonAtmosphere/mars/MieExtinctionSpectrum.csv cext 3e8
19  MieScattering: Csv input/MiePythonAtmosphere/mars/MieExtinctionSpectrum.csv csca 3e8
20
21  RayleighPhaseFunction: Rayleigh
22  RayleighScattering: Csv input/MiePythonAtmosphere/mars/RayleighExtinctionSpectrum.csv csca
    ↪   2.7e22
23
24  PlanetRadius: 3390.0 #in km
25  AtmosphereRadius: 3510.0 #in km
26  RayleighScaleHeight: 8.0 #in km
27  MieScaleHeight: 10.0 #in km
```

Hybrid

```
1   name: hybrid
2   output_directory: output/images
3   image_type: SkyImage #LuminanceAndImage #RadianceLuminance
4   sun_strength: 0.43 # 586.2 (w/m^2) / 1361.0(w/m^2)
5   sun_zenith: 89
6   sun_azimuth: 7.0
7   white_balance: true
8   brightness: auto #auto #auto|[1...inf]
9   brightnessFactor: 10.0
10  show_imprint: false
11  width: 200 #0
12  height: 100 #0
13  #model: Bruneton SINGLE_SCATTERING_ONLY 15 #SINGLE_SCATTERING_ONLY,
    ↪   DOUBLE_SCATTERING_ONLY, ALL_ORDERS
14  model: Bruneton ALL_ORDERS 15 # [Meyran,Bruneton,default: Nishita93]
15
16  MiePhaseFunction: CsvPhaseFunction
    ↪   input/MiePythonAtmosphere/mars/MixedMiePhaseFunctionSpectrum.csv
17
18  MieExtinction: Csv input/MiePythonAtmosphere/mars/MieExtinctionSpectrum.csv cext 4.64e8
```

```
19   MieScattering: Csv input/MiePythonAtmosphere/mars/MieExtinctionSpectrum.csv csca 4.64e8
20
21   RayleighPhaseFunction: Rayleigh
22   RayleighScattering: Csv input/MiePythonAtmosphere/mars/RayleighExtinctionSpectrum.csv csca
     ↪  2.7e23
23
24   PlanetRadius: 3390.0 #in km
25   AtmosphereRadius: 3510.0 #in km
26   RayleighScaleHeight: 8.0 #in km
27   MieScaleHeight: 10.0 #in km
```

A.2 Phase Function Spectrum Calculation

```
1    import pandas as pd
2    import numpy as np
3    import MieHelper as miehelper
4
5    samples = miehelper.createGammaDistribution(1.6e-6, 0.2, steps=5000)
6    wavelengths = np.linspace(360 * nm, 830 * nm, 48)
7    angularResolution = 1800
8    theta = np.linspace(0, 180, angularResolution)
9
10   phaseFunctionDataframe = pd.DataFrame()
11   phaseFunctionDataframe.index.name = 'theta'
12
13   for _wavelength in wavelengths:
14       _m = calculateRefractiveIndex(_wavelength, m_dust=1.5 - 0j, mix=0.03)
15
16       phaseFunctionAccumulator = np.zeros(angularResolution)
17
18       for _radius in samples:
19           _, phaseFunction = miehelper.calculateScatteringPhaseFunctions(theta, _wavelength,
             ↪  _m, _radius)
20           phaseFunctionAccumulator += phaseFunction
21
22       phaseFunctionAccumulator /= len(samples)
23
24       index = int(_wavelength * 1e9)
25       phaseFunctionDataframe = pd.concat([phaseFunctionDataframe, pd.DataFrame({index:
         ↪  phaseFunctionAccumulator}, index=theta)], axis=1)
```

```
1    import miepython
2    def calculateScatteringPhaseFunctions(_theta, _wavelength, m, radius):
3        x = (2 * np.pi * radius) / _wavelength
4        mu = np.cos(np.pi * _theta / 180)
5
6        qext, qsca, qback, g = miepython.mie(m, x)
7        albedo = qsca / qext
8        intensity = miepython.i_unpolarized(m, x, mu)
9        phaseFunction = intensity / albedo  # normalized to 1
10
11       return intensity, phaseFunction
```

```
1  def calculateRefractiveIndex(_wavelength, m_dust=1 + 0j, mix=0):
2      m_hematite = lookupRefractiveIndex(_wavelength / um)  #from the Amsterdam-Granada
   ↪    Light Scattering Database
3      return maxwellGarnettMixingRule(m_hematite, m_dust, mix)
```

[52, 53]

A.2.1 Maxwell Garnett Mixing Rule

```
1  import cmath
2  def maxwellGarnettMixingRule(nA, n0, vA):
3      numerator = (nA * nA) + 2 * (n0 * n0) + 2 * vA * (nA * nA - n0 * n0)
4      denominator = (nA * nA) + 2 * (n0 * n0) - vA * (nA * nA - n0 * n0)
5
6      nsquare = (n0 * n0) * (numerator / denominator)
7
8      res = cmath.sqrt(nsquare)
9      return complex(res.real, -abs(res.imag))  #ensure complex part is negative
```

A.2.2 Gamma Distribution Implementation

```
1  import numpy as np
2  def createGammaDistribution(effectiveRadius, variance, steps=200):
3          # a - effective radius
4          # b - effective variance
5          a = effectiveRadius
6          b = variance
7          k = (1 - 2 * b) / b
8          theta = a * b
9
10         samples = np.random.gamma(k, theta, steps)
11         return samples
```

A.3 Wavelength Dependent Phase Function in the Shader

```
1  //180 degrees with a resolution of 0.25° -> 720 values with each having a phase function
   ↪    value for each of the 3 wavelengths
2  vec3 mie_phase_function_values[mie_phase_function_value_count] =
   ↪    vec3[](vec3(5.213453,8.951169,16.224125), ..., vec3(0.102438,0.085918,0.055660));
```

Blue Moon's Model

```
1  vec3 MiePhaseFunction(float nu /*cosinus of scattering angle*/) {
2          int maxIndex = mie_phase_function_value_count-1;
3          float theta = acos(nu)/pi;
4
5          //linear interpolation between angles
6          float start = float(maxIndex)*theta;
7      int index1 = int(start);
8      int index2 = min(index1+1, maxIndex);
```

```
9
10       float alpha = max(0.0f, min(start-float(index1), 1.0f));
11       return mix(
12              mie_phase_function_values[int(index1)],
13              mie_phase_function_values[int(index2)], alpha);
14   }
```

Costa et al.

```
1  vec3 MiePhaseFunction(float nu) {
2         float r = DoubleHenyeyGreenstein(nu, /*g1*/0.03f, /*g2*/0.094f,
     ↪      /*alpha*/0.743f);//680nm
3
4         float g = DoubleHenyeyGreenstein(nu, /*g1*/0.4f, /*g2*/0.094f,
     ↪      /*alpha*/0.743f);//550nm
5
6         float b = DoubleHenyeyGreenstein(nu, /*g1*/0.67f, /*g2*/0.094f,
     ↪      /*alpha*/0.743f);//440nm
7
8         return vec3(r, g, b);
9  }
```

Collienne

```
1  vec3 MiePhaseFunction(Number g, float nu) {
2      float p = HenyeyGreenstein(nu, g);
3      return vec3(p, p, p);
4  }
```

Ground Texture UV Coordinates

```
1  vec3 posOnPlanet = normalize((camera + view_direction *
     ↪  distance_to_intersection)-earth_center);
2  float lon = atan(posOnPlanet.z, -posOnPlanet.y);
3  float lat = asin(-posOnPlanet.x);
4  float u = clamp((lon / PI + 1.0f)/2.0f, 0.0f, 1.0f);
5  float v = clamp((lat / PI + 0.5f), 0.0f, 1.0f);
6  vec2 uv = vec2(u, v);
```

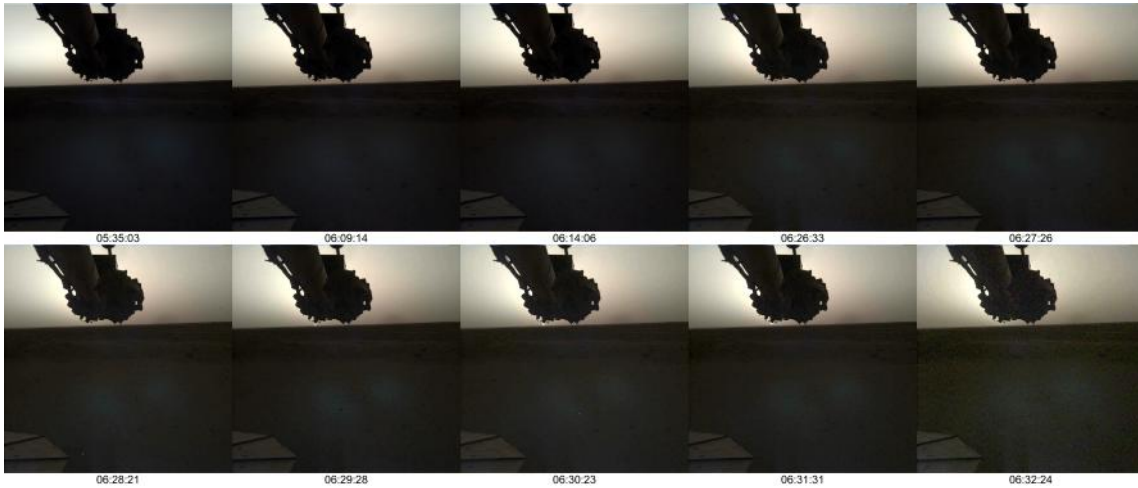## A.4 Additional Images and Renderings

Figure A.1: NASA's InSight Mars lander acquired this image using its robotic arm-mounted, Instrument Deployment Camera (IDC). These images were acquired on April 24, 2019, Sol 145 where the time is the local mean solar time for the image exposures. Each IDC image has a field of view of 45x45 degrees [59].
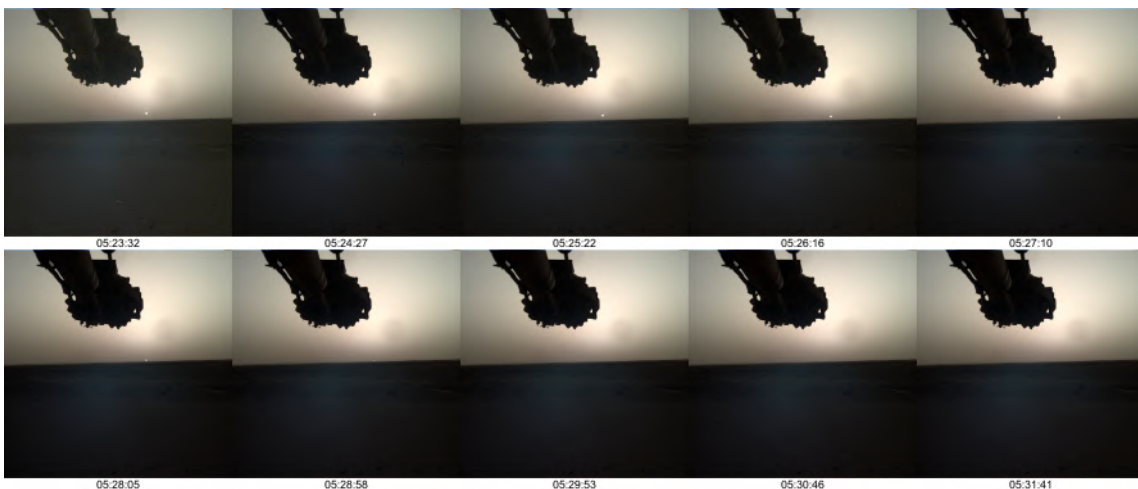

Figure A.2: NASA's InSight Mars lander acquired this image using its robotic arm-mounted, Instrument Deployment Camera (IDC). These images were acquired April 10, 2022, Sol 1198 where the time is the local mean solar time for the image exposures. Each IDC image has a field of view of 45x45 degrees [59].

Figure A.4 shows rendered sky dome views for all four models at sun elevation angles ranging from 5° to 35°.
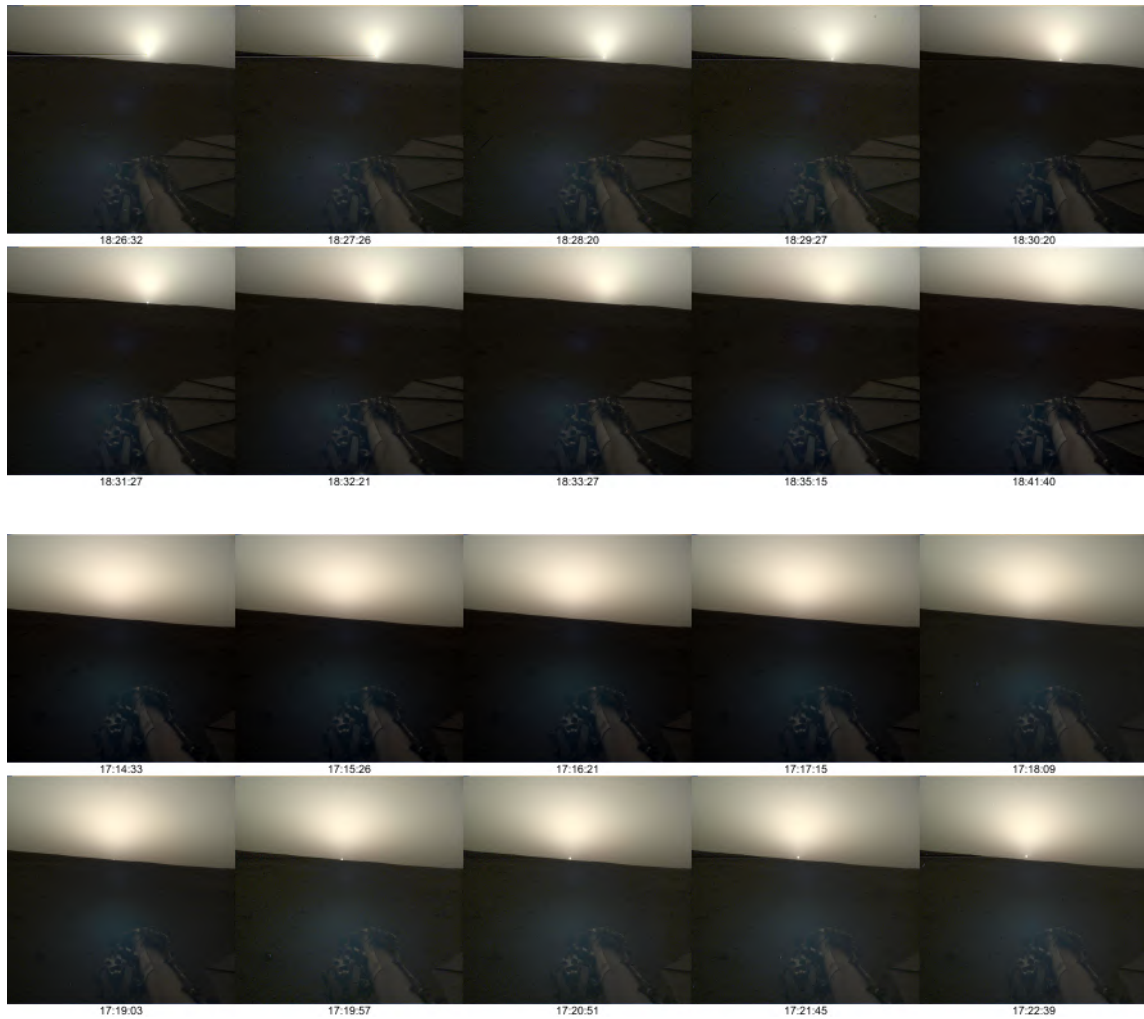
Figure A.3: NASA's InSight Mars lander acquired this image using its robotic arm-mounted, Instrument Deployment Camera (IDC). The images were acquired on April 24, 2019, Sol 145 (top) and April 10, 2022, Sol 1198 (bottom) where the time is the local mean solar time for the image exposures. Each IDC image has a field of view of 45×45 degrees [59].
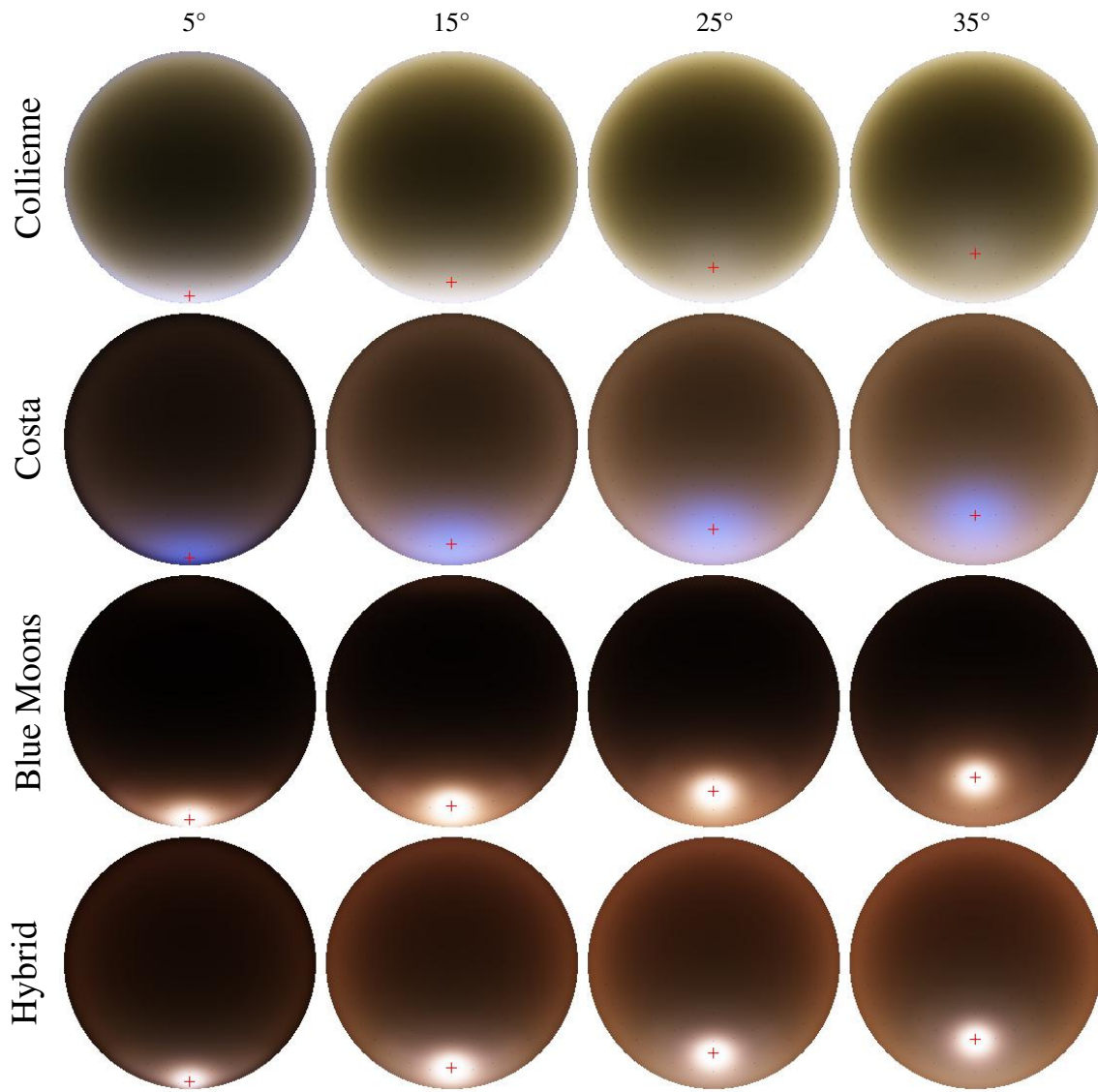
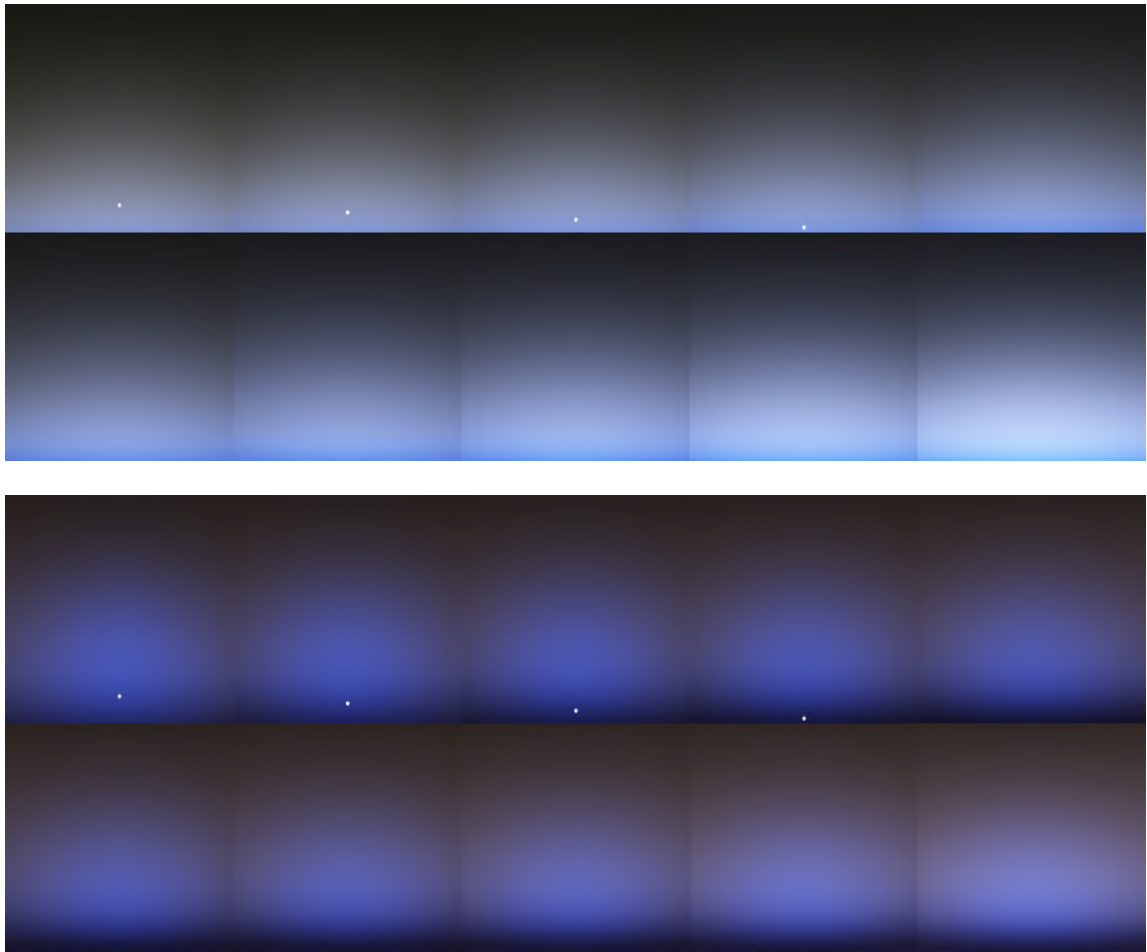Figure A.4: Color sky dome render of all four models.

Figure A.5: Sunset rendered with the model by Collienne (top) and the model by *Costa et al.* (bottom).

Figure A.6: Sunset rendered the Blue Moons's model (top) and the Hybrid model (bottom).

Bibliography

[1] A&M/Cornell, N.: *PIA07997: A Moment Frozen in Time*. `https://photojournal.jpl.nasa.gov/catalog/PIA07997`, visited on 2022-10-14.

[2] Bruneton, E.: *A Qualitative and Quantitative Evaluation of 8 Clear Sky Models*. IEEE Transactions on Visualization and Computer Graphics, 23(12):2641–2655, Dec. 2017, ISSN 1077-2626. `http://ieeexplore.ieee.org/document/7723935/`, visited on 2022-08-17.

[3] Bohren, C. F. and D. R. Huffman: *Absorption and scattering of light by small particles*. Wiley-VCH, Weinheim, 2004, ISBN 978-0-471-29340-8.

[4] Baker, J.: *50 Schlüsselideen Astronomie und Kosmologie*. Springer-Verlag, 2015.

[5] Vollmer, M.: *Atmosphärische optik für einsteiger: Lichtspiele in der luft*. Springer-Verlag, 2019.

[6] Coddington, O., J. L. Lean, P. Pilewskie, M. Snow, C. Lindholm, D. Lindholm, and N. C. Program: *NOAA Climate Data Record (CDR) of Solar Spectral Irradiance (SSI), NRLSSI Version 2.1*, 2017. `https://data.nodc.noaa.gov/cgi-bin/iso?id=gov.noaa.ncdc:C01542`, visited on 2022-09-05, Type: dataset.

[7] *A ray of light being refracted in a plastic block*. `https://en.wikipedia.org/wiki/Refraction#/media/File:Refraction_photo.png`, visited on 2022-09-23.

[8] Hecht, E.: *Optics*. Pearson Education, Inc, Boston, 5 ed ed., 2017, ISBN 978-0-13-397722-6.

[9] Ehlers, K., R. Chakrabarty, and H. Moosmüller: *Blue moons and Martian sunsets*. Applied Optics, 53(9):1808, Mar. 2014, ISSN 1559-128X, 2155-3165.

[10] Hulst, H. C. V. D.: *Light scattering by small particles*.

[11] Elek, O.: *Efficient methods for physically-based rendering of participating media*. 2015.

[12] Stamnes, K., G. E. Thomas, and J. J. Stamnes: *Radiative Transfer in the Atmosphere and Ocean*. Cambridge University Press, 2nd ed., July 2017, ISBN 9781107094734 9781316148549. `https://www.cambridge.org/core/product/identifier/9781316148549/type/book`, visited on 2022-09-13.

[13] Mie, G.: *Beiträge zur Optik trüber Medien, speziell kolloidaler Metallösungen*. Annalen der Physik, 330(3):377–445, 1908, ISSN 00033804, 15213889. `https://onlinelibrary.wiley.com/doi/10.1002/andp.19083300302`, visited on 2022-08-17.

[14] Gnangarra: *Alexander's band*. `https://commons.wikimedia.org/wiki/File:Alexanders_band_gnangarra.jpg`, visited on 2022-10-14.

[15] Bucholtz, A.: *Rayleigh-scattering calculations for the terrestrial atmosphere*. Applied Optics, 34(15):2765, May 1995, ISSN 0003-6935, 1539-4522. `https://opg.optica.org/abstract.cfm?URI=ao-34-15-2765`, visited on 2022-08-17.

[16] Nishita, T., T. Sirai, K. Tadamura, and E. Nakamae: *Display of the earth taking into account atmospheric scattering.* In *Proceedings of the 20th annual conference on Computer graphics and interactive techniques - SIGGRAPH '93*, pp. 175–182, Not Known, 1993. ACM Press, ISBN 978-0-89791-601-1. `http://portal.acm.org/citation.cfm?doid=166117.166140`, visited on 2022-08-17.

[17] Penndorf, R.: *Tables of the Refractive Index for Standard Air and the Rayleigh Scattering Coefficient for the Spectral Region between 02 and 200 micrometer and Their Application to Atmospheric Optics.* Journal of the Optical Society of America, 47(2):176, Feb. 1957, ISSN 0030-3941. `https://opg.optica.org/abstract.cfm?URI=josa-47-2-176`, visited on 2022-08-17.

[18] Barmettler, J.: *Physical sun and sky models in appleseed.* 2020. Publisher: University of Zurich tex.faculty: Faculty of Business, Economics and Informatics.

[19] Elek, O.: *Rendering Parametrizable Planetary Atmospheres with Multiple Scattering in Real-Time.* p. 9.

[20] Cornette, W. M. and J. G. Shanks: *Physically reasonable analytic expression for the single-scattering phase function.* Applied Optics, 31(16):3152, June 1992, ISSN 0003-6935, 1539-4522. `https://opg.optica.org/abstract.cfm?URI=ao-31-16-3152`, visited on 2022-08-17.

[21] Lagarde, S. and C. De Rousiers: *Moving frostbite to physically based rendering.* In *SIGGRAPH 2014 conference, vancouver*, 2014.

[22] Klassen, R. V.: *Modeling the effect of the atmosphere on light.* ACM Transactions on Graphics, 6(3):215–237, July 1987, ISSN 0730-0301, 1557-7368. `https://dl.acm.org/doi/10.1145/35068.35071`, visited on 2022-08-17.

[23] *Barmettler, Joel - 2020 - Physical Sun and Sky Models in appleseed.pdf.*

[24] Haber, J., M. Magnor, and H. P. Seidel: *Physically-based simulation of twilight phenomena.* ACM Transactions on Graphics, 24(4):1353–1373, Oct. 2005, ISSN 0730-0301, 1557-7368. `https://dl.acm.org/doi/10.1145/1095878.1095884`, visited on 2022-08-17.

[25] O'Neil, S.: *Chapter 16. Accurate Atmospheric Scattering.* p. 9.

[26] Bruneton, E. and F. Neyret: *Precomputed Atmospheric Scattering.* Computer Graphics Forum, 27(4):1079–1086, June 2008, ISSN 01677055, 14678659. `https://onlinelibrary.wiley.com/doi/10.1111/j.1467-8659.2008.01245.x`, visited on 2022-08-17.

[27] Preetham, A. J., P. Shirley, and B. Smits: *A practical analytic model for daylight.* In *Proceedings of the 26th annual conference on Computer graphics and interactive techniques - SIGGRAPH '99*, pp. 91–100, Not Known, 1999. ACM Press, ISBN 978-0-201-48560-8. `http://portal.acm.org/citation.cfm?doid=311535.311545`, visited on 2022-08-17.

[28] Hosek, L. and A. Wilkie: *An Analytic Model for Full Spectral Sky-Dome Radiance.* p. 9.

[29] NASA/ESA, Bell, J, and Wolff,M: *Hubble's Closest View of Mars*, Aug. 2003. `https://esahubble.org/images/opo0322a/`, visited on 2022-09-23.

[30] Williams, D. R. and NSSDCA: *Mars Fact Sheet*, Dec. 2021. `https://nssdc.gsfc.nasa.gov/planetary/factsheet/marsfact.html`, visited on 2022-09-23.

[31] Costa, J., A. Bock, C. Emmart, C. Hansen, A. Ynnerman, and C. Silva: *Interactive Visualization of Atmospheric Effects for Celestial Bodies*. IEEE Transactions on Visualization and Computer Graphics, 27(2):785–795, Feb. 2021, ISSN 1077-2626, 1941-0506, 2160-9306. `https://ieeexplore.ieee.org/document/9222377/`, visited on 2022-08-17.

[32] Lemmon, M. T., M. J. Wolff, M. D. Smith, R. T. Clancy, D. Banfield, G. A. Landis, A. Ghosh, P. H. Smith, N. Spanovich, B. Whitney, P. Whelley, R. Greeley, S. Thompson, J. F. Bell, and S. W. Squyres: *Atmospheric Imaging Results from the Mars Exploration Rovers: Spirit and Opportunity*. Science, 306(5702):1753–1756, Dec. 2004, ISSN 0036-8075, 1095-9203. `https://www.science.org/doi/10.1126/science.1104474`, visited on 2022-08-30.

[33] NASA/JPL: *PIA01120: Pathfinder on Mars*. `https://photojournal.jpl.nasa.gov/catalog/PIA01120`, visited on 2022-10-14.

[34] Tomasko, M. G., L. R. Doose, M. Lemmon, P. H. Smith, and E. Wegryn: *Properties of dust in the Martian atmosphere from the Imager on Mars Pathfinder*. Journal of Geophysical Research: Planets, 104(E4):8987–9007, Apr. 1999, ISSN 01480227. `http://doi.wiley.com/10.1029/1998JE900016`, visited on 2022-08-17.

[35] Dabrowska, D. D., O. Muñoz, F. Moreno, J. L. Ramos, J. Martínez-Frías, and G. Wurm: *Scattering matrices of martian dust analogs at 488nm and 647nm*. Icarus, 250:83–94, Apr. 2015, ISSN 00191035. `https://linkinghub.elsevier.com/retrieve/pii/S0019103514006526`, visited on 2022-10-09.

[36] Hille, K.: *The Fact and Fiction of Martian Dust Storms*, Sept. 2015. `http://www.nasa.gov/feature/goddard/the-fact-and-fiction-of-martian-dust-storms`, visited on 2022-10-17.

[37] Ho, C., N. Golshan, and A. Kliore: *Radio Wave Propagation Handbook for Communication on and Around Mars*. p. 116.

[38] Chen-Chen, H., S. Pérez-Hoyos, and A. Sánchez-Lavega: *Characterisation of Martian dust aerosol phase function from sky radiance measurements by MSL engineering cameras*. Icarus, 330:16–29, Sept. 2019, ISSN 00191035. `https://linkinghub.elsevier.com/retrieve/pii/S0019103519300843`, visited on 2022-09-26.

[39] Hansen, J. E. and L. D. Travis: *Light scattering in planetary atmospheres*. Space Science Reviews, 16(4):527–610, Oct. 1974, ISSN 1572-9672. `https://doi.org/10.1007/BF00168069`, visited on 2022-09-26.

[40] Wolff, M. J., M. D. Smith, R. T. Clancy, R. Arvidson, M. Kahre, F. Seelos, S. Murchie, and H. Savijärvi: *Wavelength dependence of dust aerosol single scattering albedo as observed by the Compact Reconnaissance Imaging Spectrometer*. Journal of Geophysical Research, 114:E00D04, June 2009, ISSN 0148-0227. `http://doi.wiley.com/10.1029/2009JE003350`, visited on 2022-08-17.

[41] Tan, C.: *Determination of refractive index of silica glass for infrared wavelengths by IR spectroscopy*. Journal of Non-Crystalline Solids, 223(1-2):158–163, Jan. 1998, ISSN 00223093.

`https://linkinghub.elsevier.com/retrieve/pii/S0022309397004389`, visited on 2022-10-18.

[42] Malitson, I. H.: *Interspecimen Comparison of the Refractive Index of Fused Silica*,†*. Journal of the Optical Society of America, 55(10):1205, Oct. 1965, ISSN 0030-3941. `https://opg.optica.org/abstract.cfm?URI=josa-55-10-1205`, visited on 2022-10-18.

[43] Henning, T., B. Begemann, H. Mutschke, and J. Dorschner: *Optical properties of oxide dust grains.* Astronomy and Astrophysics Supplement Series, 112:143, 1995.

[44] Yen, A., R. Gellert, B. Clark, D. Ming, P. King, M. Schmidt, L. Leshin, R. Morris, S. Squyres, and J. Campbell: *Evidence for a global martian soil composition extends to Gale Crater.* In *Lunar and planetary science conference*, 2013. Number: JSC-CN-27936.

[45] Querry, M.: *Optical Constants of Minerals and Other Materials from the Millimeter to the Ultraviolet*, Nov. 1987. `https://apps.dtic.mil/sti/citations/ADA192210`.

[46] Christensen, P. R., R. V. Morris, M. D. Lane, J. L. Bandfield, and M. C. Malin: *Global mapping of Martian hematite mineral deposits: Remnants of water-driven processes on early Mars.* Journal of Geophysical Research: Planets, 106(E10):23873–23885, Oct. 2001, ISSN 01480227. `http://doi.wiley.com/10.1029/2000JE001415`, visited on 2022-08-17.

[47] Wolff, M. J., R. Todd Clancy, J. D. Goguen, M. C. Malin, and B. A. Cantor: *Ultraviolet dust aerosol properties as observed by MARCI.* Icarus, 208(1):143–155, July 2010, ISSN 00191035. `https://linkinghub.elsevier.com/retrieve/pii/S0019103510000205`, visited on 2022-08-17.

[48] Collienne, P., R. Wolff, A. Gerndt, and T. Kuhlen: *Physically Based Rendering of the Martian Atmosphere*. p. 12.

[49] NASA, JPL-Caltech, MSSS, and Texas A&M Univ.: *Sunset in Mars' Gale Crater*, Apr. 2015. `https://www.jpl.nasa.gov/images/pia19400-sunset-in-mars-gale-crater`, visited on 2022-09-23.

[50] Morales, C., T. Oishi, and K. Ikeuchi: *Real-time rendering of aerial perspective effect based on turbidity estimation.* IPSJ Transactions on Computer Vision and Applications, 9(1):1, Dec. 2017, ISSN 1882-6695. `https://link.springer.com/10.1186/s41074-016-0012-1`, visited on 2022-08-17.

[51] Bock, Alexander: *OpenSpace/OpenSpace · GitHub*, Feb. 2022. `https://github.com/OpenSpace/OpenSpace/compare/master...integration/paper-atmosphere`, visited on 2022-09-27.

[52] Muñoz, O., H. Volten, J. W. Hovenier, M. Min, Y. G. Shkuratov, J. P. Jalava, W. J. van der Zande, and L. B. F. M. Waters: *Experimental and computational study of light scattering by irregular particles with extreme refractive indices: hematite and rutile.* Astronomy & Astrophysics, 446(2):525–535, Feb. 2006, ISSN 0004-6361, 1432-0746. `http://www.aanda.org/10.1051/0004-6361:20053727`, visited on 2022-10-03.

[53] Muñoz, O., F. Moreno, D. Guirado, D. Dabrowska, H. Volten, and J. Hovenier: *The Amsterdam–Granada Light Scattering Database*. Journal of Quantitative Spectroscopy and Radiative

Transfer, 113(7):565–574, May 2012, ISSN 00224073. `https://linkinghub.elsevier.com/retrieve/pii/S0022407312000386`, visited on 2022-10-03.

[54] *miepython — miepython 2.3.0 documentation.* `https://miepython.readthedocs.io/en/latest/`, visited on 2022-10-04.

[55] Ångström, A.: *On the Atmospheric Transmission of Sun Radiation and on Dust in the Air.* Geografiska Annaler, 11(2):156–166, Aug. 1929, ISSN 2001-4422. `https://www.tandfonline.com/doi/full/10.1080/20014422.1929.11880498`, visited on 2022-08-17.

[56] ebruneton: *ebruneton/clear-sky-models*, July 2022. `https://github.com/ebruneton/clear-sky-models`, visited on 2022-10-03, original-date: 2016-01-17T07:39:13Z.

[57] Bell III, J., D. Savransky, and M. J. Wolff: *Chromaticity of the Martian sky as observed by the Mars Exploration Rover Pancam instruments.* Journal of Geophysical Research: Planets, 111(E12), 2006. Publisher: Wiley Online Library.

[58] Lemmon, M. T., M. J. Wolff, J. F. Bell, M. D. Smith, B. A. Cantor, and P. H. Smith: *Dust aerosol, clouds, and the atmospheric optical depth record over 5 Mars years of the Mars Exploration Rover mission.* Icarus, 251:96–111, May 2015, ISSN 00191035. `https://linkinghub.elsevier.com/retrieve/pii/S0019103514001559`, visited on 2022-10-27.

[59] NASA/JPL-Caltech: *Raw Images from Insight.* `https://mars.nasa.gov/insight/multimedia/raw-images/?order=sol+desc%2Cdate_taken+desc&per_page=50&page=0&mission=insight&begin_sol=1198&end_sol=1198&af=idc`, visited on 2022-10-14.